

國立臺灣大學理學院海洋研究所



碩士論文

Graduate Institute of Oceanography

College of Science

National Taiwan University

Master Thesis

台灣西南海域微量金屬沈積歷史

Historical Record of Trace Metals Offshore Southwestern Taiwan

李純瑜

Chun-Yu Lee

指導教授：蘇志杰博士

Advisor: Chih-Chieh Su, Ph.D.

中華民國 107 年 10 月

October, 2018

國立臺灣大學碩士學位論文
口試委員會審定書

台灣西南海域微量金屬沈積歷史
Historical Record of Trace Metals Offshore
Southwestern Taiwan

本論文係李純瑜君 (R05241310) 在國立臺灣大學理學院海洋研究所完成之碩士學位論文，於民國 107 年 9 月 28 日承下列考試委員審查通過及口試及格，特此證明。

口試委員：

鄭志杰

(簽名)

(指導教授)

溫良政

林毅田

系主任、所長

詹森

(簽名)

誌謝



在讀研究所的路上，真的很幸運能遇到蘇老師，老師在研究上總是給予我們非常彈性的空間和最大的資源，雖然我總是被死線追著跑，但老師總是盡心盡力提供他最大的協助，真的非常非常感謝老大。另外還要特別感謝溫老師和小田學長，沒有你們，我研究所可能要讀 6 年（太衰 XD），所以每次負能爆棚的時候都會想：大家都盡全力幫妳了，妳還有什麼資格不努力？你們的幫助和支持都是我前進的動力，真的非常謝謝你們不論是在實驗上或論文寫作上給我的幫助，使我得以順利完成我的碩士學業。

另外，也非常幸運遇到實驗室的大家，謝謝帶我入門分析化學的 Lulu，從小豆學長的計畫到自己的實驗，總是耐心幽默的教會我好多事，從完美的滴定到發現我們都有強迫症（擊掌），讓我跟無塵室變好朋友；305 小家長聖婷和堯禮，總是在我不知道該怎麼辦時提供貼心意見，並準備食物餵食療癒我們這群孩子（絕對是畢業後會最想念的溫馨下午茶時光），還有那一同分樣的美好；心思細膩的怡雯姊，總是貼心的關心提醒，還有超積極的辦事效率，覺得有妳的照顧真好；鳳心不時暖心的問候和貼心的糖果補給，真的是疲累時的充電能量；半夜研究室大師兄宇璜的卡農放送（行健說要關燈配合想像自己是居里夫人 XD），著實是首提高效率的經典神曲；還有同學家騏、喆元一起的學習討論還有幫忙；AA 上機治平的八卦不無聊時光，睿晟的酸，佩俞的手沖咖啡；鶴漢和乒乓在 EGU 幫我拿到的暖心啤酒；深受學弟愛戴的巴馬策勵我要運動……，還有感謝太多太多的人，沒有你們，我的研究生生活不會如此充實而美滿。

也感謝那些實驗上遇到的不順，讓我學會嘗試自己解決問題、尋求答案，而且還多學會做不同的儀器，果然多看多學即使失敗卻都還是收穫滿滿。

最後，還是最感謝爸媽的愛與支持，讓我回家可以無憂耍廢盡情享受當爸寶媽寶的幸福時光，還有那個像是從來沒離開過的你，相信我一路上的幸運，都有你的 blessing。

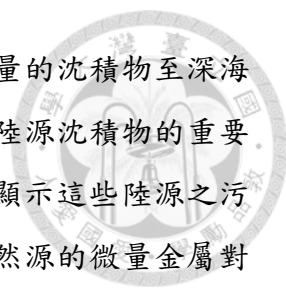
中文摘要



台灣位於活動型大陸邊緣，板塊擠壓造山使其發展出眾多高山型小河，這些河流快速侵蝕地表挾帶大量陸源沈積物傳輸至海洋。自 1970 年代起，台灣工業迅速發展，1980 年代開始，台灣重金屬汙染問題不斷浮現，甚至擴及沿岸地區，顯示人為活動已經對臺灣周遭環境造成一定程度的影響。在此地質環境和人為活動的交互作用下，這些流經高度工業發展和人口居住密集區域的河川，勢必會將這些經濟發展下對於環境造成負面影響的產物帶進海洋環境當中，此研究目的於探討這些人為汙染物於海洋沈積物中的堆積歷史紀錄，以了解其傳輸之控制機制、來源及其擴散影響的範圍。

高屏溪為台灣流域面積最大的一條河流，因流經人口居住密集及工業高度發展之地區，與其他世界大河相比，擁有顯著高濃度的顆粒態和溶解態金屬。高屏海底峽谷位於台灣西南海域，其峽谷頭部幾乎與高屏溪連接，為高屏溪帶來大量陸源物質往深海傳輸的主要通道。本研究主要利用鉛-210 定年、粒徑分析、地化分析（分析元素包括 Zn, Cr, Pb, Co, Ni, Cu, Cd, Fe, Mn, Al, Ti, Mg, K）等方法，分析在西南海域周邊採集之岩芯，並以其金屬對 Al 之比值與自然環境（平均上部地殼、平均臺灣沈積岩、揚子陸塊及平均頁岩）背景值相比，以分辨沈積物中微量金屬之來源。根據岩心採樣位置，可劃分為三大類：(I) 高屏峽谷上段兩側陸坡站位；(II) 高屏峽谷下段深海站位；(III) 澎湖峽谷頭部異源站位。

本研究之結果發現在陸棚外之區域找不到顯著的人為汙染訊號，陸棚外大部分重金屬呈現出相對穩定的時間分佈，其和 Al 的比值皆接近或低於自然背景。然而，於峽谷上段陸坡站位的表層沈積物中記錄到輕微的 Pb 富集及其隨時間顯著增加的趨勢，但於深海站並未紀錄到此趨勢，顯示陸源的汙染訊號主要可以到達高屏陸坡。此外，雖與自然背景並無明顯差異，但在高屏陸坡上這些記錄到 Pb 隨某段時間劇烈增加的站位中，皆可清楚描繪出台灣工業發展開始的時期(1970 年代)。除了微量金屬的人為輸入之外，也發現自然災害（地震，颱風等）亦會加速海洋環境中微量金屬的累積。在高屏陸坡和深海這兩個沈積環境中，兩者擁有相當的微量金屬累積質量和相對一致的 Ti / Al 莫耳比，顯示這些由高屏峽谷傳輸之沈積



物可以越過陸棚，除了一部分堆積至陸坡，另外也運送相當大量的沈積物至深海中沈積。雖然沈積物於此研究區跨棚傳輸之特性，使深海成為陸源沈積物的重要匯區，但在本研究的深海站位並未發現微量金屬的污染記錄，顯示這些陸源之污染信號可以在進一步向遠洋傳輸的過程中被稀釋，揭示這些汙然源的微量金屬對於深海的影響是微不足道的。

關鍵字：臺灣西南海域、高屏海底峽谷、汙染歷史、自然災害、傳輸、深海

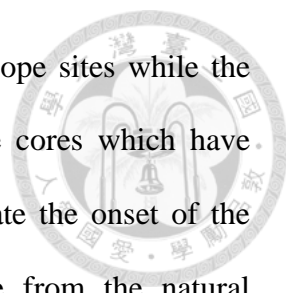
ABSTRACT



Rapid economic and industrial development over the past five decades in Taiwan has caused the expense of environment. Heavy metals pollution issue has gradually emerged after the 1980s and the contaminated area has extended to the coastal environment. With the tectonic setting and climatic condition in Taiwan, a considerable amount of pollutants could be carried into the marine environment. The aim of this study is to investigate the distribution and transportation of heavy metals through sedimentary records offshore southwestern Taiwan.

Gaoping River (GPR) is the largest river in southern Taiwan and stands out of other major world rivers for its high concentrations of dissolved and particulate metals. Gaoping Submarine Canyon (GPSC) has been proven to be the major pathway for the transportation of terrestrial materials discharged from GPR into the deep sea. In this study, ^{210}Pb dating, grain size and geochemical analyses (Zn, Cr, Pb, Co, Ni, Cu, Cd, Fe, Mn, Al, Ti, Mg, K) were applied to the sediment cores sampled in three different sedimentary environments around the GPSC: (I) Gaoping Slope sites, (II) Deep sea sites at lower reach of GPSC, and (III) Penghu Submarine Canyon site. Since trace metals could be derived from natural or anthropogenic sources, reference background materials (UCC, ACST, UC-YC and Average Shale) are compared to distinguish the source of the trace metals.

Compared to previous studies conducted in the nearshore regions, pollution signals are hardly to be found in our further seaward sites (Gaoping Slope & deep sea), most of the measured trace metals display a stable temporal distribution with a level near or under the natural background. However, slight enrichment of Pb and its sharp increase



were still recorded within the surface sediments at the Gaoping Slope sites while the records are absent in the deep sea. Moreover, the Gaoping Slope cores which have conformably recorded the pollution of Pb can even clearly illustrate the onset of the industrial development in Taiwan despite their subtle difference from the natural background. Other than the anthropogenic input of the trace metals, natural hazards (earthquakes, typhoons, etc.) are also found to accelerate the accumulation of trace metals in the marine environment. The comparable amount of cumulative mass of the trace metals between Gaoping slope and the deep sea sites and the relatively consistent Ti/Al molar ratio between these two sedimentological regimes, all suggesting that the sediments discharged from GPR could cross the narrow shelf and made a considerable amount to transport and accumulate in the deep sea. Though deep sea can act as an important sink for the terrestrial materials due to the cross-shelf transport, pollution record was not found in the deep sea sites as the pollution signals can be largely diluted during the further seaward transport, implying the pollution in the deep sea is insignificant in the study area.

Keywords: Gaoping Submarine Canyon, Southwestern Taiwan, Trace Metals, Pollution Record, Natural Hazards, Transport, Deep Ocean

CONTENTS

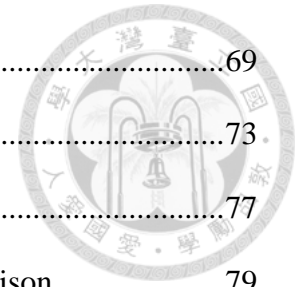


口試委員會審定書	#
誌謝	i
中文摘要	ii
ABSTRACT	iv
CONTENTS	vi
LIST OF FIGURES	ix
LIST OF TABLES	xii
Chapter 1 Introduction.....	1
1.1 Introduction.....	1
1.2 Background.....	2
1.3 Study Area	3
1.3.1 Gaoping River (GPR).....	3
1.3.2 Gaoping Shelf.....	4
1.3.3 Gaoping slope.....	5
1.3.4 Gaoping Submarine Canyon (GPSC).....	5
1.3.5 Penghu Submarine Canyon	6
1.4 Study Aims	7
Chapter 2 Sampling & Methods	12
2.1 Sampling	12
2.1.1 Sampling Sites.....	12
2.1.2 Sampling Method	12
2.2 Sample Treatment	15

2.3	Analytical Method	16
2.3.1	Water Content.....	16
2.3.2	X-Radiography	17
2.3.3	²¹⁰ Pb Geochronology.....	18
2.3.4	Grain Size Analysis	24
2.3.5	Geochemical Analysis	27
Chapter 3	Results and Discussions	34
3.1	Sedimentary Properties	34
3.1.1	Gaoping Continental Slope Site: S2, S6, S1 and B4G.....	34
3.1.2	Deep Sea Site: MT6 and MT7	36
3.1.3	Penghu Submarine Canyon Site: PL02	39
3.2	Major Element Ratios	39
3.2.1	Reference Element (Al).....	39
3.2.2	Reference Backgrounds	42
3.2.3	Ti/Al Molar Ratio	50
3.3	Vertical Distribution of the Metals	55
3.3.1	S2 (Gaoping Slope Site).....	55
3.3.2	S6 (Gaoping Slope Site).....	56
3.3.3	S1 (Gaoping Slope Site).....	57
3.3.4	B4G (Gaoping Slope Site)	59
3.3.5	PL02 (Penghu Submarine Canyon Site)	60
3.3.6	MT6 (Deep Sea Site).....	61
3.3.7	MT7 (Deep Sea Site).....	63
3.4	Source of the Elements	64
3.5	Enrichment of the Trace Metals.....	69



3.5.1	Mn	69
3.5.2	Pb.....	73
3.6	Cumulative Mass of the Trace Metals	77
3.7	Lead Pollution in Aquatic Sediments in a global Comparison	79
Chapter 4	Conclusion	83
	REFERENCE	85
	APPENDIX	90



LIST OF FIGURES

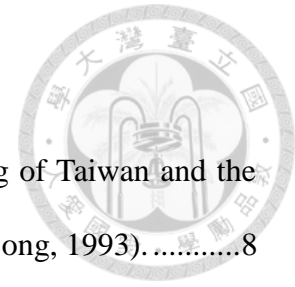


Figure 1-1 Schematic block diagram illustrating the tectonic setting of Taiwan and the associated major submarine physiographic units (Yu & Song, 1993).8

Figure 1-2 The sediment dispersal system off southwestern Taiwan (Yu et al., 2009). ...9

Figure 1-3 The intraslope basins distributed on the Gaoping Slope which are separated by the mud diapiric ridges (Yu & Huang , 2006).10

Figure 1-4 The Gaoping (formerly spelled “Kaoping”) Submarine Canyon has two morphologic breaks that separate it into three distinct segments, including upper reach, a middle reach and lower reach (Chiang & Yu, 2006). 11

Figure 2-1 Study area and sampling sites.13

Figure 2-2 Flowchart of the sample treatment.16

Figure 2-3 The ^{226}Ra , ^{222}Rn , ^{210}Pb , and ^{210}Po in ^{238}U decay series (Swarzenski, 2014). 19

Figure 2-4 Conceptual illustration of the dominant sources and transport pathways for ^{210}Pb (Swarzenski, 2014).20

Figure 3-1 The X-Radiography, core surface image, and profiles of ^{210}Pb , water content and grain size in core S2.35

Figure 3-2 The X-Radiography, core surface image, and profiles of ^{210}Pb , water content and grain size in core S6.35

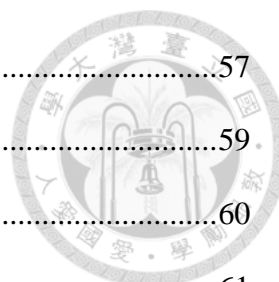
Figure 3-3 The X-Radiography, core surface image, and profiles of ^{210}Pb , water content and grain size in core S1.36

Figure 3-4 The X-Radiography, core surface image, and profiles of ^{210}Pb , water content and grain size in core B4G.36

Figure 3-5 The X-Radiography, core surface image, and profiles of ^{210}Pb , water content and grain size in core MT6.37

Figure 3-6 The X-Radiography, core surface image, and profiles of ^{210}Pb , water content and grain size in core MT7.	38
Figure 3-7 The topographic map showing the location of core MT6 and MT7 (modified from 蔡, 2014).	38
Figure 3-8 The X-Radiography, core surface image, and profiles of ^{210}Pb , water content and grain size in core PL02.	39
Figure 3-9 Vertical distributions of Al with comparison to the clay fraction in each sediment core analyzed in this study.	41
Figure 3-10 Down core Ti/Al ratio with comparison to the reference background materials (ACST, UCC, UC-YC, Average Shale) in each sediment core analyzed in this study.	46
Figure 3-11 Down core Fe/Al ratio with comparison to the reference background materials (ACST, UCC, UC-YC, Average Shale) in each sediment core analyzed in this study.	47
Figure 3-12 Down core Mg/Al ratio with comparison to the reference background materials (ACST, UCC, UC-YC, Average Shale) in each sediment core analyzed in this study.	48
Figure 3-13 Down core K/Al ratio with comparison to the reference background materials (ACST, UCC, UC-YC, Average Shale) in each sediment core analyzed in this study.	49
Figure 3-14 The Ti/Al molar ratios from the fluvial sediments (temporary sinks) and the surface soils (source materials) along the Gaoping (Kaoping) River drainage (Chen et al., 2013).	52
Figure 3-15 The spatial distribution of Ti/Al molar ratio compared to previous studies.	54
Figure 3-16 Vertical distribution of the metals in core S2.	56

Figure 3-17	Vertical distribution of the metals in core S6.....	57
Figure 3-18	Vertical distribution of the metals in core S1.....	59
Figure 3-19	Vertical distribution of the metals in core B4G.	60
Figure 3-20	Vertical distribution of the metals in core PL02.	61
Figure 3-21	Vertical distribution of the metals in core MT6.....	62
Figure 3-22	Vertical distribution of the metals in core MT7.....	64
Figure 3-23	Scatter plot between concentrations of metals (Mg, Ti, Fe, K, Mn, Zn) and Al for each sample in different sediment cores analyzed in this study.....	67
Figure 3-24	Scatter plot between concentrations of metals (Cr, Pb, Co, Ni, Cu, Cd) and Al for each sample in different sediment cores analyzed in this study.....	68
Figure 3-25	Vertical distributions of Mn and Mn/Al ratio with comparison to the natural backgrounds in each sediment core analyzed in this study.....	71
Figure 3-26	Vertical distributions of Mn and Fe in each sediment core analyzed in this study.....	72
Figure 3-27	Vertical distributions of Pb and Pb/Al ratio with comparison to the natural backgrounds in each sediment core analyzed in this study.....	75
Figure 3-28	Temporal variations of Pb in (b) Gaoping Slope compared to that in the (a) Gaoping coastal area (head of GPSC) from previous study (Hung & Hsu, 2004).....	76
Figure 3-29	Cumulative mass of the metals in the last 150 years in core PL02, S2, S6, MT6, B4G and S1.....	78



LIST OF TABLES



Table 2-1	The detailed information of the collected cores.....	14
Table 2-2	The detailed FAAS (iCE 3000 SERIES, Thermo) analytical protocols for the analyzed element of Zn and Pb.....	31
Table 2-3	The detailed ICP-MS (iCapQs, Thermo) analytical protocols for the analyzed element of Mg, Al, K, Ti, Fe, Mn, Cr, Co, Ni, Cu, Cd.....	31
Table 2-4	The concentrations of the standard used to build the calibration line for each element in FAAS (iCE 3000 SERIES Thermo) and ICP-MS (iCapQs, Thermo).....	32
Table 2-5	The results of the Certified Reference Material PACS-3 analyzed in the study.....	33
Table 3-1	The mean major element/Al mass ratios compared to previous study by Chen & Selvaraj (2008) and the reference materials (UCC, ACST, UC-YC, and Average Shale).....	44
Table 3-2	The background ratios of M/Al in different reference materials used in this study.....	45
Table 3-3	The mean 100Ti/Al molar ratios in surface sediments along the Gaoping dispersal system.....	53
Table 3-4	Comparison in cumulative mass of the trace metals contributed from non-event and event period in core MT6 and B4G.....	79
Table 3-5	Estimated increasing rate of anthropogenic Pb flux in different aquatic sediments around the world.....	82

Chapter 1 Introduction

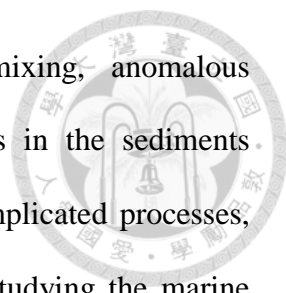


1.1 Introduction

Trace metals present a trace concentration in the environment matrices. Some of them are vital elements for living organisms, though when they exceed certain threshold concentrations in the environment they can be toxic/noxious and play a threat on lives of either plants or animals (Järup, 2003; Nagajyoti et al., 2010). It has been acknowledged that some of these metals have many adverse health effects and can exist in the environment for a long period of time that can affect the biosphere and hydrosphere. With the global development of industrialization and urbanization, the anthropogenic input of heavy metals has sharply increased in the last century, which makes metal contamination become an important issue worldwide. These metals will not be removed by natural degradation processes, and they can be accumulated in the environment over time, which makes them become a special group of pollutants and deserve a great concern.

Either natural processes or anthropogenic activities could bring metals into the marine environment. The metal elements can be easily adsorbed onto the surface of particles associated with the organic material and can be transported and deposited to the underlying sediments. They are introduced to the marine sediment system through several pathways, including direct terrestrial input from rivers, air deposition, and scavenging from the water column, among which, the riverine input is generally the major source, and can bring a tremendous amount of these metals into the marine environment.

After deposition, distributions of the metals can be modified again by the



post-depositional processes, such as bioturbation, sediment mixing, anomalous sedimentation events (slumps and gravity flows), and diagenesis in the sediments (Finney & Huh, 1989; Zwolsman et al., 1993). Through these complicated processes, the ocean can serve as a final sink for these trace metals. With studying the marine sediments, we could extract the information from sediment records for knowing the influence of surface runoff, the interaction between terrestrial and marine materials and the anthropogenic impacts on the environment.

1.2 Background

Taiwan is located on a collision boundary of the Eurasian Plate and Philippine Sea plate, which formed the fold-and-thrust mountain belt and developed many small mountainous rivers on the island (Figure 1-1). Compared to other river basins with different elevations of headwaters in the world, Milliman and Syvitski (1992) suggest these tectonic-generated small mountainous rivers can deliver a much tremendous amount of sediments to the sea and the sediments were more liable to escape from narrow continental shelves to deep waters. Ranged in the latitude of subtropical/ tropical and western edge of Pacific Ocean, Taiwan is deeply influenced by the East Asia monsoon and tropical cyclone system. Kao and Milliman (2008) also point out the importance of earthquakes and typhoons induced episodic events under the tectonic setting and climatic condition of Taiwan and reveal the potential impacts on the river discharge and yield from human activities.

Since the 1970s, Taiwan has experienced a rapid economic and industrial development which subsequently brought a negative impact on the environment. After the 1980s, the problems of heavy metal pollution gradually emerged, and many coastal

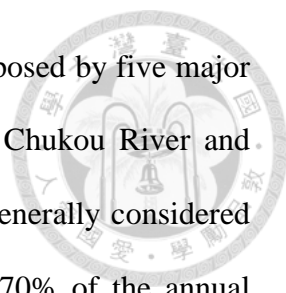
areas in western Taiwan have been found contaminated with different heavy metals to some extent. It indicates the contaminated area has expanded to the coastal environment and a considerable amount of trace metals might further be brought to the offshore environment. Thus we would like to know whether these man-made pollutants would be continued transport into the deep sea and be recorded (accumulated) in the marine sediments, or they will be buffered by the great natural pool, ocean, through some geochemical processes.

1.3 Study Area

The seafloor morphology off southwestern Taiwan comprises the Gaoping Shelf and Gaoping Slope and finally descends to a water depth of more than 3000 m in the northern end of the abyssal basin of South China Sea. The study area is mainly along the path of Gaoping Submarine Canyon (GPSC) offshore southern Taiwan. The GPSC, which developed on the active continental margin, is the largest submarine canyon system in this geographic area and serves as an active conduit for transporting the terrestrial sediments from Gaoping River to the abyssal plain (Liu et al., 2002; Huh et al., 2009; Yu et al., 2009; Su et al., 2018). Together with the source from the Gaoping River, and pathway cutting through the Gaoping Shelf and Gaoping Slope, they constitute the sediment dispersal system off southwestern Taiwan (Figure 1-2).

1.3.1 Gaoping River (GPR)

The Gaoping River (GPR) is the largest river in southern Taiwan with a drainage area of 3257 km². Originated from the southern part of the Jade Mountain, it has a mainstream of 171 km and a relatively high average slope gradient of 1/150

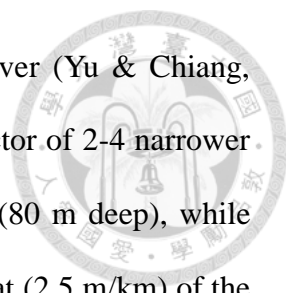


(Hydrological Yearbook of Taiwan, 2017). The GPR system is composed by five major tributaries, including Cishan River, Laonong River, Baolai River, Chukou River and Ailiao River. Among them, Cishan River and Laonong River are generally considered as the primary stream of the river system which contribute over 70% of the annual discharge. Two hydrological seasons can be derived from the monthly runoff distribution of GPR. The dry season is from November to April, and due to southwest monsoon and typhoon activities, the wet season is mainly from May to October. Consequently, the wet season accounts for over 90% of the annual rainfall (~3000 mm/year) in the river basin. The relatively high slope gradient and high precipitation rate of the GPR system also make it as one of the highest physical denudation rates (10934 ton/km² year) area in the world (Li, 1976; Chung et al., 2009).

Gaoping River flows through densely populated areas and industrial districts in the lower watershed, and the lower part of GPR is heavily polluted due to the discharge from metal scrap factories and livestock farms. As a result, the GPR is not only one of the most contaminated rivers in Taiwan, if compared to other major world rivers, GPR can also present as a prominent role for its high concentrations of either dissolved or particulate metals (Hung & Hsu, 2004). According to Doong et al. (2008), very high concentrations of Cr, Cu, Ni, Zn were detected in the sediments from GPR due to the discharge from swinery and industrial wastewaters.

1.3.2 Gaoping Shelf

The Gaoping Shelf is an offshore extension (progradation) from the sediments progressively deposited seaward from the Pingtung Plain (Yu & Chiang, 1997). It has a length of 100 km that extends northward from the southern tip of the Hengchun Peninsula, turning its direction to northwestward at Fangliao beside the Chaochou Fault



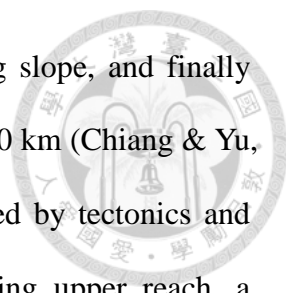
and finally reaches its northern end at the mouth of Tsengwen River (Yu & Chiang, 1997). It is characterized with a narrow platform (20 km wide, a factor of 2-4 narrower than the average width of shelves worldwide) and shallow waters (80 m deep), while having an average slope gradient of 5 m/km which is greater than that (2.5 m/km) of the shelves around the world (Yu & Chiang, 1997). The morphological properties of this shelf are dictated by the tectonic setting of the uplifting Taiwan orogen and the associated sedimentation process.

1.3.3 Gaoping slope

Stretching from the Gaoping Shelf, the Gaoping Slope extends southwestward for a long distance over a broad and deeply sloping region of more than 16000 km², and finally reaches a water depth of 3500 m (Yu & Song, 1993). An escarpment on the slope ranging at the water depth of 1200 to 2000 m has separated the slope into two parts with an immediate relief over 800 m, producing a steep upper slope and a gentle lower slope (Yu & Song, 1993; Chiang & Yu, 2006). The irregular topography on the slope is the interplay results of deformations of folding, faulting and mass wasting, and silts and clays are the main constitutes in this physiographic region (Yu & Song, 1993; Chiang & Yu, 2006). Mud diapirs were discovered widely distributed on this slope region, forming intraslope basins between these structural highs, and a distinct upward series of seismic facies can be found over the sedimentary processes in these basins (Figure 1-3, Yu & Huang, 2006).

1.3.4 Gaoping Submarine Canyon (GPSC)

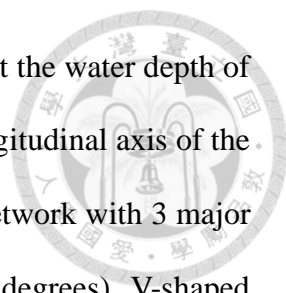
Gaoping Submarine Canyon begins immediately with the river mouth of GPR,



crossing through the narrow Gaoping shelf and the broad Gaoping slope, and finally emerging into the northern end of Manila Trench with a length of 260 km (Chiang & Yu, 2006). According to the morphological features of GPSC controlled by tectonics and structures, it can be divided into three distinct segments, including upper reach, a middle reach and lower reach (Figure 1-4). The upper reach cutting through the shelf and the upper slope meanders towards southwest with a distance of 88 km to a water depth of 1600 m (Chiang & Yu, 2006). With a sharp bend from the upper reach, the middle reach presents a nearly linear southeast orientation along the foot of the escarpment with V-shaped valley and extends for a distance of 65 km to a water depth of 2600 m (Chiang & Yu, 2006), and be consider as either a temporary sediment sink or conduit (Yu et al., 2009). The lower reach finally turns back toward the southwest direction on the lower slope and elongates with a distance of 100 km where it emerges into the northern end of Manila Trench at the water depth of 3500 m (Chiang & Yu, 2006). Previous geophysical study along this canyon suggests that the recurrent hyperpycnal flows in the GPSC can be an important force to erode Gaoping Shelf and Gaoping Slope and brought the eroded sediments continually transported to the deep sea (Yu et al., 2009).

1.3.5 Penghu Submarine Canyon

Eastern to the GPSC, there lies another submarine canyon, Penghu Submarine Canyon, which separates the Gaoping slope and the South China Sea slope. It has a length of 180 km from its head started from the shelf break of the Taiwan Strait Shelf to its mouth emerging into the Manila Trench. Unlike most of the submarine canyons developed on submarine slopes with heads normal to the shoreline, Penghu Submarine Canyon has extended in a nearly north-south direction. The canyon consists of an upper



reach and a lower reach demarcated by a clear knickpoint occurred at the water depth of 2500 m and about 100 km away from the canyon head along the longitudinal axis of the canyon. Above the knickpoint, the upper reach displays a fan-like network with 3 major tributary canyons, which is characterized with a steep slope (1.42 degrees), V-shaped valleys, and high relief from the edge to the bottom of the canyon, showing a greater intensity of erosion and represents a typical canyon morphology. The lower reach shows to have only one single course without any tributary canyons and occurred on a gentle slope angle of 0.5 degrees, having broad U-shaped troughs and relatively small relief between the edges and bottoms of the canyon. These morphological properties of the lower reach canyon imply a low-intensity downward erosion and mild structural uplift by thrust faults (Yu & Chang, 2002). Penghu Submarine Canyon is also an important conduit for bringing the orogenic sediments from Taiwan and sediments from passive Chinese margin together to sink into the Manila Trench (Yu & Chang, 2002).

1.4 Study Aims

According to Hung & Hsu (2004), the surface sediments at Gaoping coastal area (near the mouth of GPR) have been largely contaminated with trace metals (Pb, Zn, Cr, Ni, Cd), and GPSC appears to be the major sink for river borne trace metals. By comparing to several published reference materials in major element ratios and applying the factor analysis, Chen & Selvaraj (2008) assess the contamination at the (iron and steel) slag-dumping area offshore southwestern Taiwan and reveal the sources and dominated geochemical associations of the elements. Previous studies about the metal distributions and contaminations in sediments off southwestern Taiwan only concentrated on the nearshore regions, while seldom has focused on the influence of

heavy metals in further seaward areas (e.g. lower slope, deep sea basin). Therefore, the study will focus on the areas on the Gaoping Slope and the deep sea basin along the Gaoping Submarine Canyon. The objective of this study is to determine the concentrations and the fate of the metals and the transport mechanisms through the sedimentary records off southwestern Taiwan.

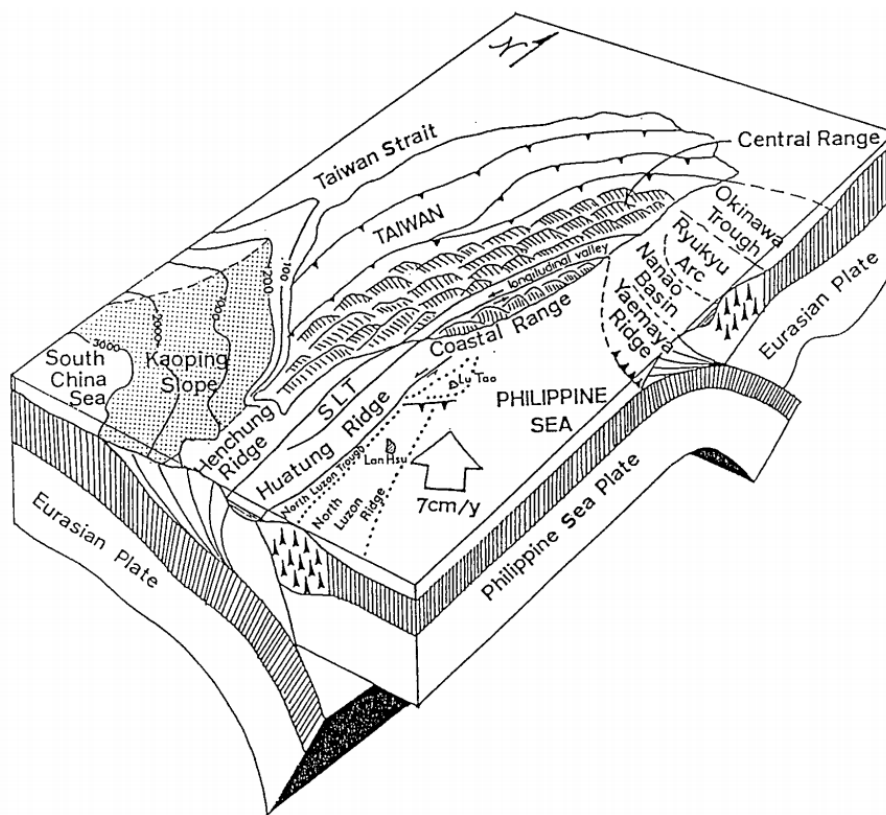


Figure 1-1 Schematic block diagram illustrating the tectonic setting of Taiwan and the associated major submarine physiographic units (Yu & Song, 1993).

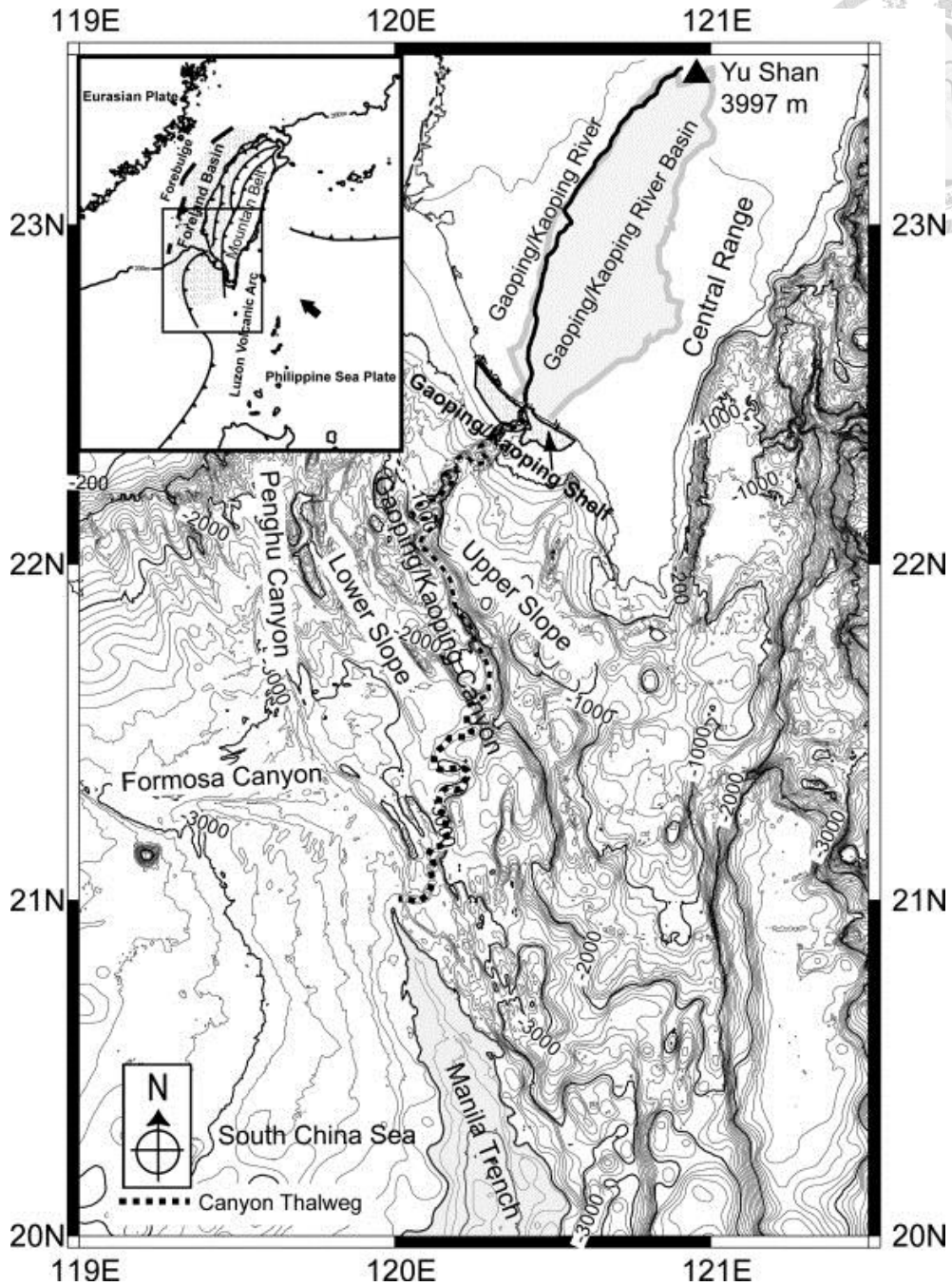


Figure 1-2 The sediment dispersal system off southwestern Taiwan, consisting of the Gaoping River (GPR), the Gaoping Shelf, the Gaoping Slope, and the Gaoping Submarine Canyon (GPSC) (Yu et al., 2009).

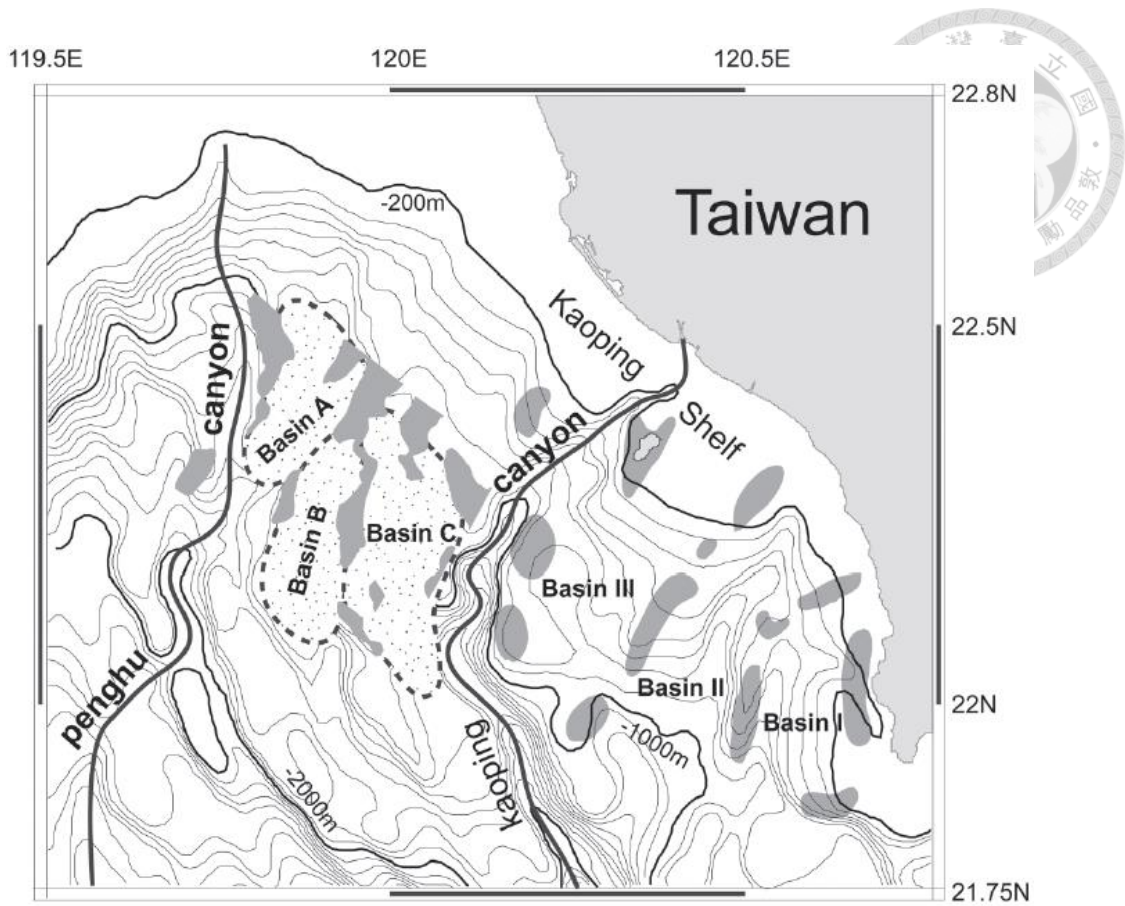


Figure 1-3 The intraslope basins distributed (determined by seismic profiles) on the Gaoping Slope which are separated by the mud diapiric ridges (Yu & Huang , 2006).

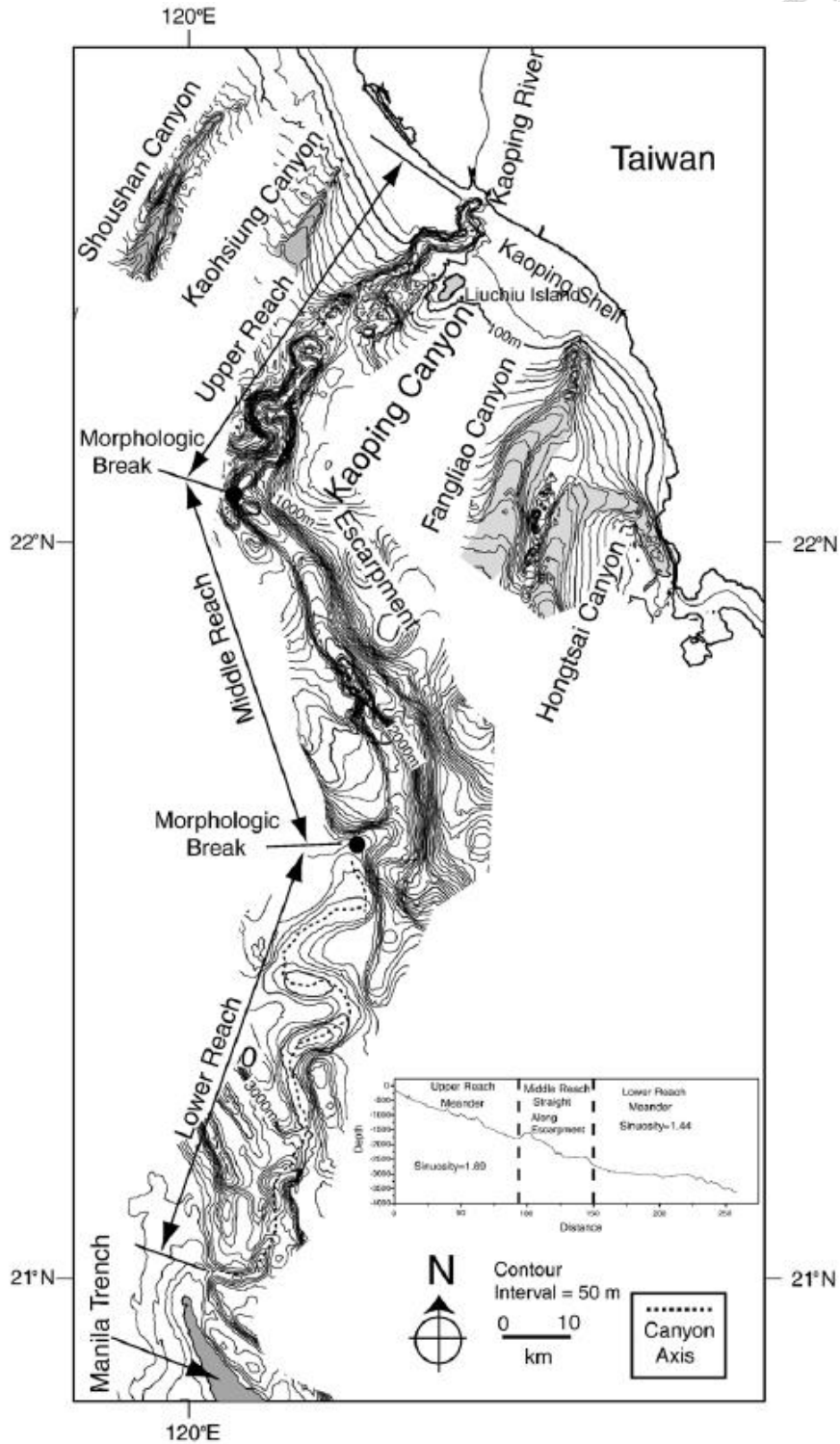


Figure 1-4 The Gaoping (formerly spelled “Kaoping”) Submarine Canyon has two morphologic breaks that separate it into three distinct segments, including upper reach, a middle reach and lower reach (Chiang & Yu, 2006).

Chapter 2 Sampling & Methods



2.1 Sampling

2.1.1 Sampling Sites

The sampling sites are mainly along the Gaoping Submarine Canyon which has been proven to be the major pathway for the transportation of terrestrial materials brought by Gaoping River into the deep sea (Liu et al. 2002; Huh et al. 2009; Su et al. 2018). Since the purpose of this study is to establish the historical record of trace metals, the sampling sites were chosen at flank of GPSC where is relatively stable and can provide a better age model for sedimentary history reconstruction. The sampling sites (Figure 2-1) represent 3 major geographic zones, including the Gaoping Slope (sites on the Gaoping Slope at lateral sides of the upper reach of GPSC, yellow squares in Figure 2-1, including S6, S2, S1 and B4G), the Penghu Submarine Canyon (a site located on the Palm Ridge at the head of Penghu Submarine Canyon, green square in Figure 2-1, PL02) and deep ocean (sites at lower reach of the GPSC with water depth over 2600m, red squares in Figure 2-1, including MT6 and MT7). The details of the sampling sites are shown in Table 2-1.

2.1.2 Sampling Method

7 sediment cores were collected by using gravity corer and piston corer on R/V Ocean Researcher 1 and R/V Ocean Researcher 5 from 2010 to 2016. Core information (core top, core length, cruise number, and station name) were marked on the core tube upon collection, and the sediment cores were immediately stood upright until the suspended particles within the core-tope water were settled down. The further processes

were removing the sea water on the core tope, cutting the tube into a proper length (<150 cm), and filling the hollow space with plastic wrap covered styrofoam to prevent the disturbance of the sediments. Both ends of the sediment cores were capped by a lid with tape sealed to prevent the loss of water contained in the sediments.

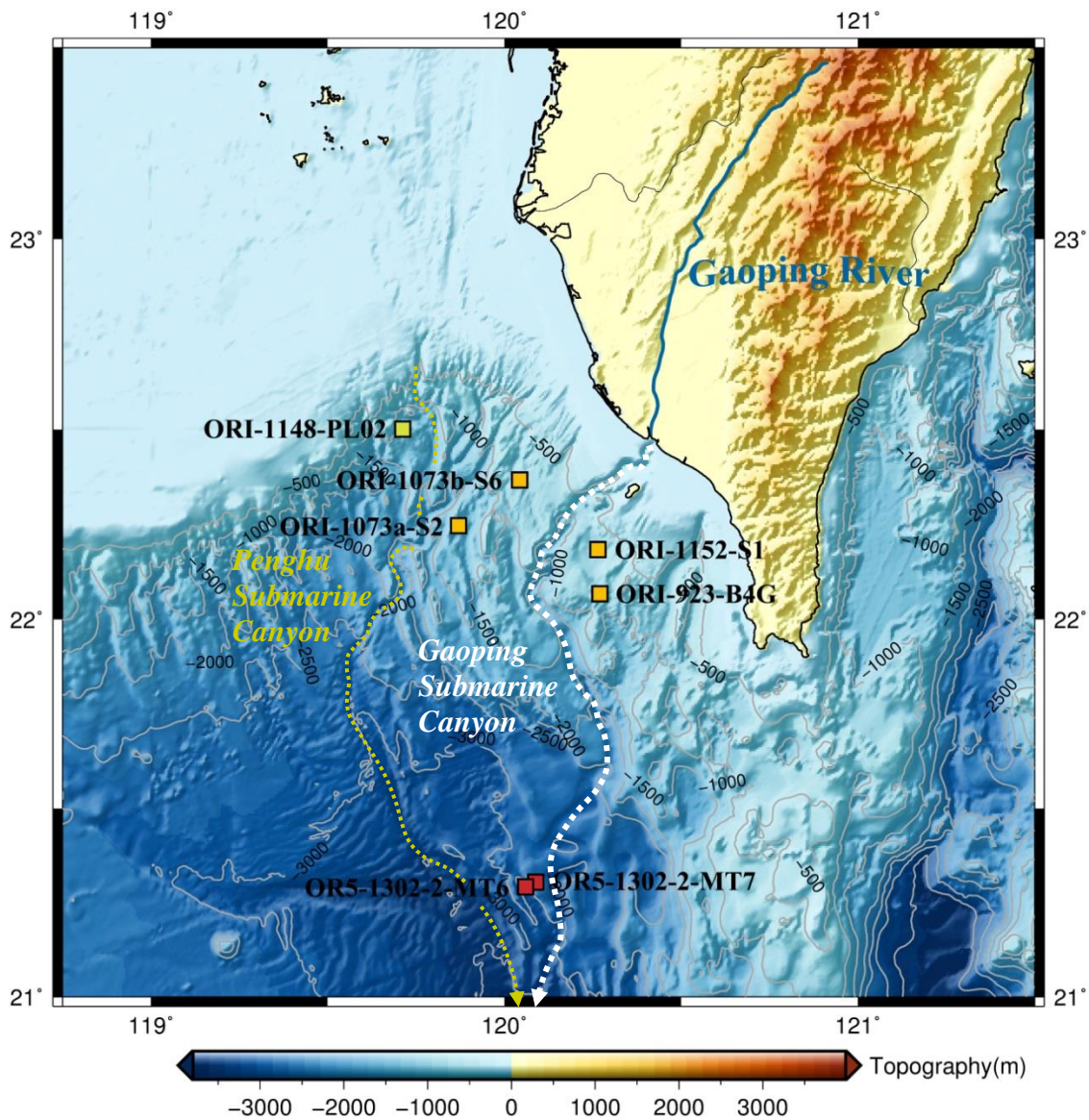
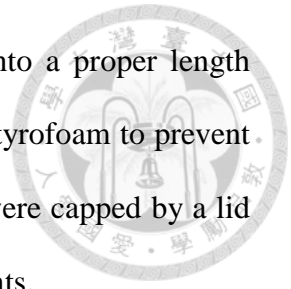


Figure 2-1 Study area and sampling sites. The collected sediment cores are from three different geographic locations: (I) Gaoping Slope (S2, S6, S1 and B4G, yellow square in the map), (II) Deep Sea (MT6 and MT7, red squares in the map), and (III) Penghu Submarine Canyon (PL02, green square in the map).



Table 2-1

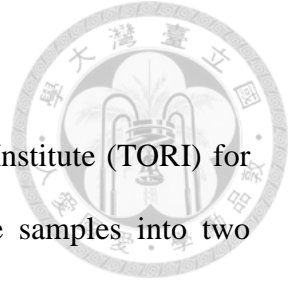
The detailed information of the collected cores.

Cruise	Station	Water Depth (m)	Sampling Time (GMT+8)	Longitude	Latitude	Core Length (cm)	Core Type	²¹⁰ Pb & Grain Size Data Source
ORI-1148	PL02	931	2016/10/04 12:30	119°42.74'	22°30.05'	114	GC	(林等人, 2016)
ORI-1073a	S2	1205	2014/05/09 06:15	119°52.218'	22°14.815'	123	GC	(徐, 2015)
ORI-1073b	S6	618	2014/05/14 22:36	120°02.58'	22°22.02'	112	GC	(徐, 2015)
ORI-1152	S1	822	2016/11/02 03:38	120°15.87'	22°11.03'	93	GC	-
ORI-923	B4G	863	2010/04/06 07:28	120°16.20'	22°04.04'	67	GC	(鄭, 2012)
OR5-1302-2	MT6	3078	2013/03/06 20:00	120°03.61'	21°17.52'	91	PC	(蔡, 2014)
OR5-1302-2	MT7	2654	2013/03/07 02:48	120°05.32'	21°18.27'	498	PC	(蔡, 2014)

GC: Gravity Core ; PC: Piston Core.

2.2 Sample Treatment

The sediment cores were sent to the Taiwan Ocean Research Institute (TORI) for preliminary treatments, including core splitting (splitting the core samples into two halves, as working and archive halves, respectively), core surface photography, core description, and Multi-Sensor Core Logger (MSCL) scan. The working halves were taken back to Marine Sedimentology and Environmental Radioactivity Lab (MSERL) at IONTU for subsequent core analysis processing, including sliced working half cores into 1 cm thickness by using a transparent acrylic slab (25 × 10 × 1 cm) for X-ray photography while the rest core sample was sliced into 1 cm interval and stored in 50 mL centrifuge tube. The samples were freeze-dried for 3-5 days prior to the following analyses. The analytical process is shown as Figure 2-2.



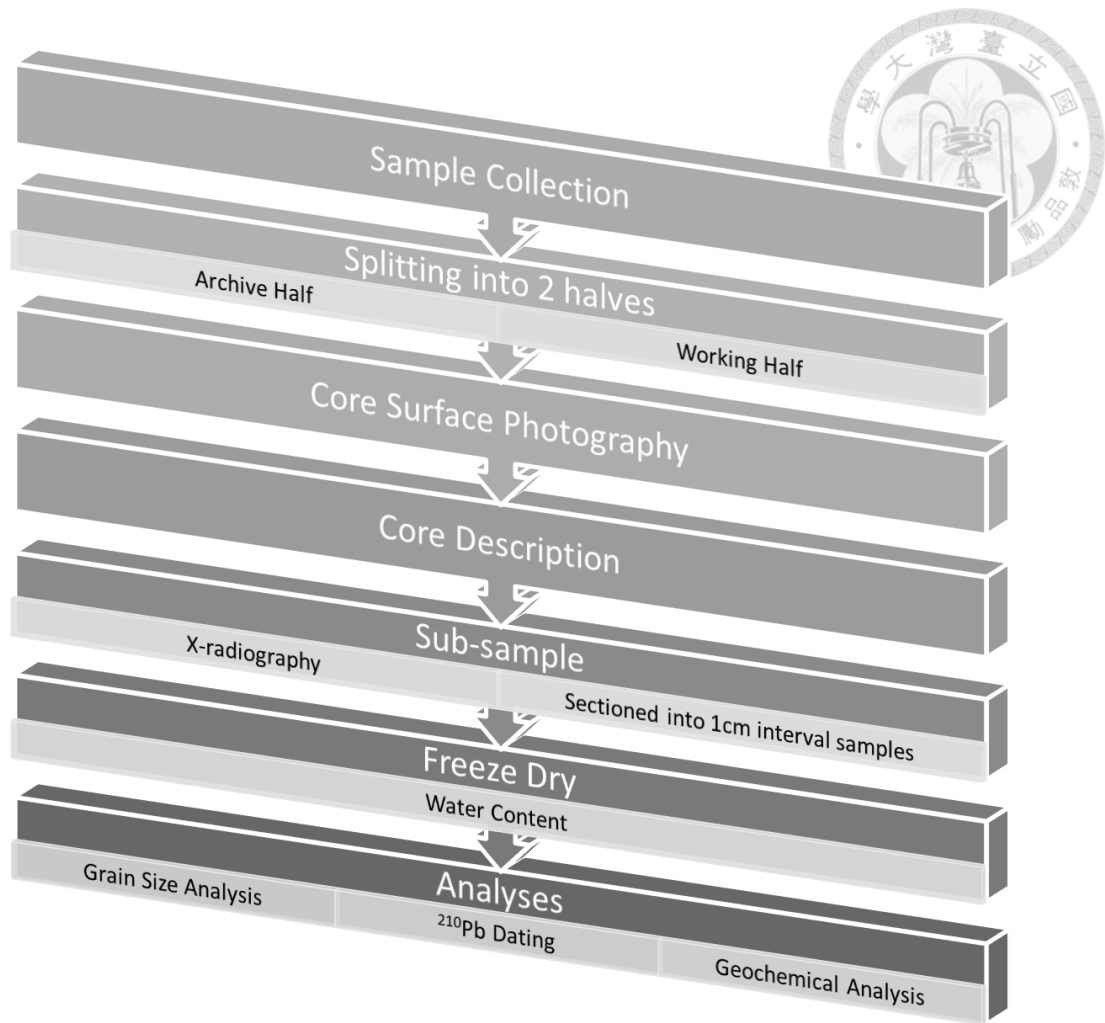


Figure 2-2 Flowchart of the sample treatment.

2.3 Analytical Method

Analytical methods of sediment samples using in this study include X-radiography, ^{210}Pb geochronology, laser grain size analysis and geochemical analysis (determine the concentrations of Zn, Cr, Pb, Co, Ni, Cu, Cd, Fe, Mn, Al, Mg, K, Ti).

2.3.1 Water Content

The water content in the sediments is the proportion of pore water in the sediments. The pore water was removed from the sediments by freeze-dryer, which applies the

condensation and vacuum state to make the water sublimate into gas and flee away from the sediments. After the wet weights of sediment samples were recorded, 1cm-interval sectioned sediments were fully frozen.

A freeze-dryer produced by Kingmech company is used to remove the pore water within the sediments, at the setting of -55°C, vacuum 30-50 millitorr (1 atm = 760000 millitorr) for 3-4 days. The water content is calculated as below:

$$\text{water}\% = \frac{W_{wet} - W_{dry}}{W_{wet} - W_{tube}} \times 100\%$$

where W_{wet} is the weight of wet sediment in the centrifuge tube, W_{dry} is the weight after being freeze-dried, and W_{tube} is the weight of the centrifuge tube without sediment sample.

2.3.2 X-Radiography

Hamblin (1962) first used the technique of X-ray photography for studying micro structures of sandstone and siltstone, followed by Calvert and Veevers (1962) to apply this method to unconsolidated marine sediments. Bouma (1964) later facilitated this method and discuss the sedimentary features obtained from this technique in different sedimentation environments. This technique allows us to build up an integrated structural picture of sediment core and provide us information for examining the homogeneity of the sample, and even reveals some latent structures lied within the sample, through, a non-destructive way.

In this study, AXR Model M160NH Cabinet X-ray System was employed to obtain the sedimentary structural pictures of the sediment samples. The 1 cm thick sediment slab (surface polished) was placed in the scan room for the X-ray exposure with the X-ray operating settings of 60-70 keV and 2-3 mA, and integration (exposure) time of

100-140 ms, all of which were adjusted in regard to the properties of the sample.

The X-radiograph image presents the sedimentary features which we can not see through our bare eyes and the primitive information about the cores through the lux of the image which is influenced by physical properties of sediments, such as density and grain size. Bioturbation or some subtle structures (mottles, streaks, etc) hidden in the sediment then can be revealed.

2.3.3 ^{210}Pb Geochronology

^{210}Pb is a naturally occurring nuclide from the ^{238}U decay series and has a half-life of 22.23 years (Figure 2-3). Derived from ^{226}Ra ($t_{1/2} = 1600$ year), ^{210}Pb has a relatively short half-life that makes them reach a radioactive secular equilibrium if the environmental system remained “closed” for a sufficient long time. However, in more recent deposited sediment, there will exist a disequilibrium due to the natural processes, like weathering, transportation and deposition. Since the disequilibrium once formed, they would tend to restore a new radioactive equilibrium which is controlled by their respective decay rate. Such radioactive properties render these nuclides as a useful time-measuring tool (Ku, 1976; Swarzenski, 2014).

The disequilibrium state of ^{210}Pb in a sedimentation system was caused from the additional source of ^{210}Pb . In general, the observed ^{210}Pb in the sediments can be divided into two parts. One part is produced from the intrinsic decay of ^{226}Ra in sediments, representing the time-independent “supported” ^{210}Pb ($^{210}\text{Pb}_{\text{supported}}$). The other is considered as the “excess” ^{210}Pb ($^{210}\text{Pb}_{\text{excess}}$) sourced from: (1) the decay of atmospheric ^{222}Rn which gets into the sedimentation system through a wet/dry deposition, (2) the riverine input, and (3) the decay of the ^{226}Ra in the water column

which enters the sedimentation system through rapid scavenging processes (^{210}Pb is a particle-reactive radionuclide which can be easily adsorbed onto suspended particles). (Figure 2-4). The excess ^{210}Pb therefore provides as a chronometer of the sediments deposited in recent 150 years under ideal depositional conditions. With the excess ^{210}Pb , we can use the time-dependent relationship to calculate the sedimentation rate.

The isotope dilution method, adding ^{209}Po as tracer into each sample, was employed to measure the activity of ^{210}Pb in sediment. Based on the principle that ^{210}Po ($t_{1/2} = 138.4$ day) and ^{210}Pb can reach secular equilibrium in 2 years, with the α count ratio of ^{210}Po and ^{209}Po and the known activity of the internal yield tracer ^{209}Po , we can obtain the activity of ^{210}Po in the samples and then calculate the activity of ^{210}Pb .

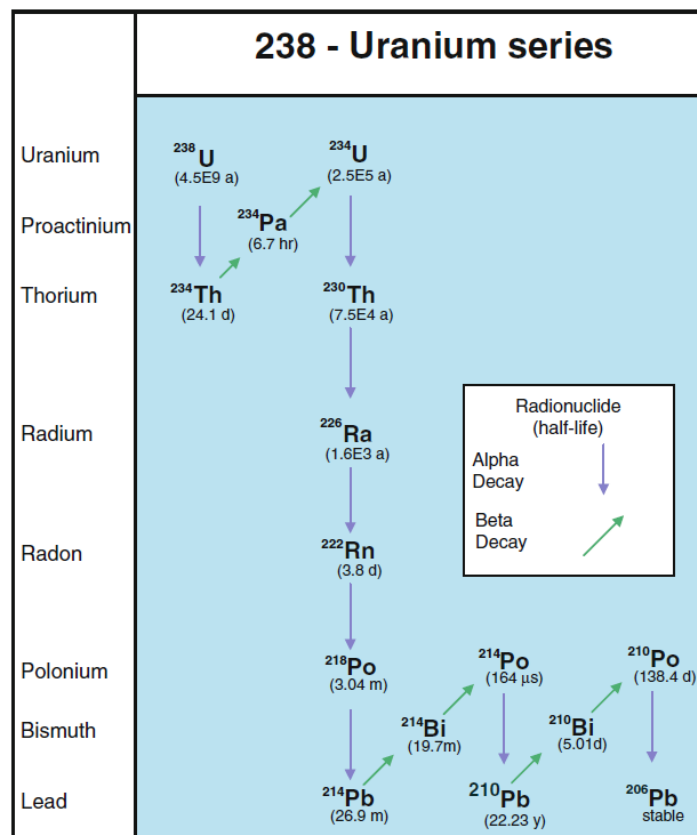


Figure 2-3 The ^{226}Ra , ^{222}Rn , ^{210}Pb , and ^{210}Po in ^{238}U decay series (Swarzenski, 2014).

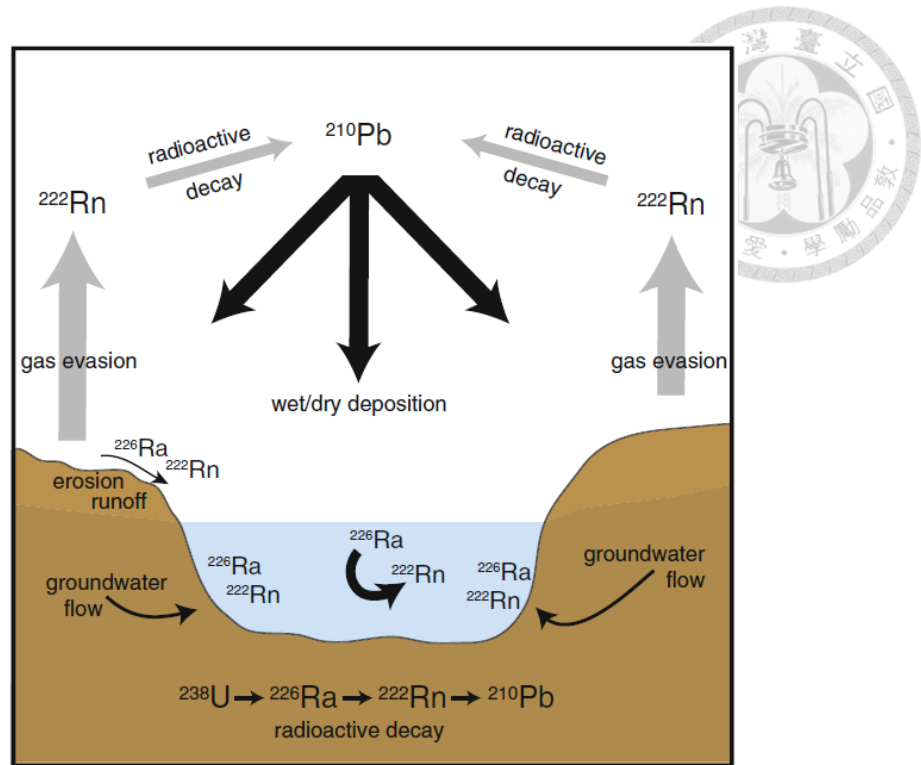
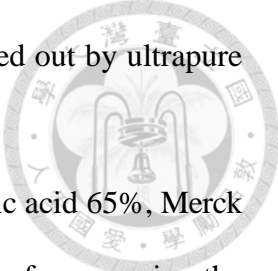


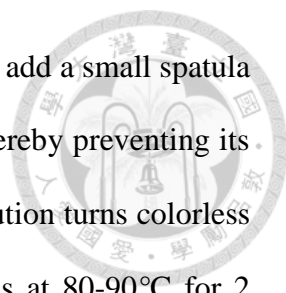
Figure 2-4 Conceptual illustration of the dominant sources and transport pathways for ^{210}Pb (Swarzenski, 2014).

The analytical procedures of ^{210}Pb in sediments are listed as follow:

- i. 0.5 g of sediment sample is placed into a cleaned crucible and record sample weight.
- ii. Crucible with the sediment sample is transferred into the drying oven and heated at 105°C for over 6 hours to remove water and the weight of water-free sample is recorded.
- iii. The water-free sample in the crucible is placed into the muffle furnace and heated at 550°C for 6 hours to ash the organic materials in sediments. The remaining sample weight is recorded after this process.
- iv. Prepare clean Teflon beakers and mark them with sample numbers. Add $100\ \mu\text{L}$ of ^{209}Po tracer into the beaker (record the “exact” weight of ^{209}Po) and transfer the

- 
- sample into the beaker (residual sediment in the crucible is rinsed out by ultrapure water).
- v. Place the Teflon beakers on the hot plate. Add 5 mL HNO₃ (Nitric acid 65%, Merck EMSURE[®]), covered the beaker and heat at 150°C for 1-2 hours for removing the carbonates in sediments. Then add 5 mL HF (Hydrofluoric acid 40%, Merck EMSURE[®]) and heat overnight at 150°C to destroy the silicates.
 - vi. Add 2 mL HClO₄ (Perchloric acid 70-72%, Merck EMSURE[®]) and continually heat at 200°C to digest the organic matter.

*Continually heat for at least 12 hours until a clear solution is obtained. Add sufficient HClO₄ to accomplish this step until the black solution turned clear.
 - vii. Remove the lid and evaporate the solution to an incipient dryness (until a yellow jelly-shaped sample appears) and then add little volume of ultrapure water (18.2 MΩ.cm) to swirl it until a clear solution appears again. A few drops of concentrated NH₄OH are added to neutralize the solution (testing the pH value with pH-indicator paper) and forming the orange ferrous iron precipitates. Transfer the orange precipitates into a cleaned centrifuge tube (rinse the Teflon beaker for several times to prevent the loss of the sample).
 - viii. Wash the orange precipitates with ultrapure water (18.2 MΩ.cm) for at least 3 times (each time centrifuged at 4500 rpm for 3 minutes and pour out the clear supernatant) until there's no smell of the ammonia.
 - ix. Add 2 mL 9N HCl to dissolve the precipitates and bring the volume to 20 mL with ultrapure water (18.2 MΩ.cm). After shaking the solution, let it sit overnight.
 - x. Add 1 mL 9N HCl into the solution and shake it till the precipitates totally dissolved. Centrifuge the solution and transfer the clear and yellow solution into a cleaned glass beaker.

- 
- xi. Put the glass beaker with sample solution onto the hot plate and add a small spatula of ascorbic acid to form a complex with ferrous iron (Fe^{2+}), thereby preventing its possible interference with the Po plating. After the color of solution turns colorless from the yellow, drop in silver disk to run the plating process at 80-90°C for 2 hours. The time when the Po plating process starts is recorded.
- xii. Pick up the silver disk from the solution and rinse it with ultrapure water (18.2 MΩ.cm) and acetone. Store them in a sealed plastic bag before the Alpha measurement.

The measurement was carried out by α spectrometer (OCTETE PC™ ALPHA SPECTROMETER) and the total activity of ^{210}Pb is corrected for the decay of ^{210}Po (from Po plating time to counting time) and ^{210}Pb (from sample collection time to Po plating time), which was calculated as below:

$$^{210}\text{Pb}_{\text{total}} = \frac{C_{210}}{C_{209}} \times \frac{A_{209}}{W} \times e^{-\lambda_{Po-210}(t_{\text{counting}}-t_{\text{plating}})} \times e^{-\lambda_{Pb-210}(t_{\text{plating}}-t_{\text{sampling}})}$$

C_{210} is the α decay counts of ^{210}Po

C_{209} is the α decay counts of ^{209}Po

A_{209} is the activity of the spiked ^{209}Po

W is the weight of salt-free and water-free sediment sample

(the weight was corrected for the salt contents based on the sea water stoichiometry, an average salinity of 35‰ was postulated)

λ_{Po-210} is the decay constant of ^{210}Po (1.829 yr^{-1})

λ_{Pb-210} is the decay constant of ^{210}Pb (0.0311 yr^{-1})

t_{sampling} is the time of sample collection

t_{plating} is the time when the Po plating process starts

$t_{counting}$ is the time when the Alpha counting starts



The down core activity of ^{210}Pb (>150 year) could be seen as the supported ^{210}Pb for the excess ^{210}Pb will not be present that it would have decayed out in the deeper sections. In this study, supported ^{210}Pb was calculated as the mean in the core bottom where there are at least 3 sections showing an approximately constant activity. Therefore, the activity of excess ^{210}Pb can be obtained by subtracting the down core activity of supported ^{210}Pb as:

$$^{210}\text{Pb}_{excess} = ^{210}\text{Pb}_{total} - ^{210}\text{Pb}_{supported}$$

For sedimentation rate calculation, we use the advection-diffusion model with the assumption of both the flux of $^{210}\text{Pb}_{excess}$ to the sediment and sedimentation rate are constant over time, once the sediments deposited (in a closed system) the relationship between $^{210}\text{Pb}_{excess}$, sedimentation rate and mixing rate can be denoted as:

$$D \frac{\partial^2 C}{\partial Z^2} - S \frac{\partial C}{\partial Z} - \lambda C = 0 \quad (2-1)$$

where Z is the depth of sample (cm or g/cm²), C is the activity of $^{210}\text{Pb}_{excess}$ at certain depth Z (dpm/g), D is the diffusion coefficient (cm²/yr), S is the sedimentation rate (cm/yr or g/cm²/yr), and λ is the decay constant of ^{210}Pb (0.0311 yr⁻¹). Under the boundary conditions of, (1) the activity of $^{210}\text{Pb}_{excess}$ at core top ($Z = 0$) is the initial activity of $^{210}\text{Pb}_{excess}$ ($C = C_0$), and (2) the activity of $^{210}\text{Pb}_{excess}$ will be 0 when the depth reach infinitely large ($Z \rightarrow \infty$), if not regarding to the mixing process, the equation (2-1) can be written as:

$$-S \frac{\partial C}{\partial Z} - \lambda C = 0 \quad (2-2)$$

the solution of the equation (2-2) is:

$$\ln C = \ln C_0 - \frac{Z}{\lambda} S$$

with the slope of the $\ln {}^{210}\text{Pb}_{\text{excess}}$ profile, we can have:

$$S = -\lambda \text{ slope}$$

where we get the apparent sedimentation rate S . In this study, the slope was obtained from the points in the upper layer based on linear least square fit where the mixing or turbidite layers were excluded.

2.3.4 Grain Size Analysis

Particle size of sediment is an important indicator of hydrodynamic conditions, transport distances, and deposition environments. Early methods for measuring particle size include sieving, settling tubes, and microscope observations. Now, a laser granulometer has been well-developed and widely-used. This laser diffraction technique is based on the principle that particles passing through a laser beam will scatter light at an angle and diminish the light intensity, both of which are related to the particle size. In this study, the grain size analysis was carried out using Laser Diffraction Particle Analyzer (Beckman Coulter LS13 320) equipped with auto-sampler with a detection range of 0.375-2000 μm (11.38 ϕ —-1 ϕ). To plot the graph of grain size distribution, a grade scale mostly used in sedimentological studies is to normalize the grain size to a logarithmic scale, for which the well sorted single-population sediments will present as nearly symmetrical Gaussian probability curve. Therefore, the particle size is generally represented in unit of ϕ , with numerical conversion to international length unit as: $\phi = -\log_2 D$ (D is the diameter of the particle in mm).

The measured sediment samples will be pre-treated to remove sea salt, organic

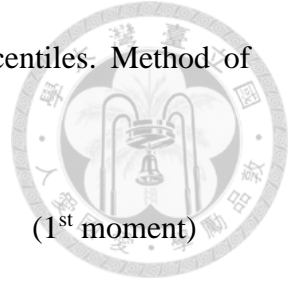


matter and carbonates, and finally followed an addition of 1% sodium hexametaphosphate as a dispersant. These pretreatment steps are to ensure that organic matter and carbonate bodies (for example, foraminifera) do not affect the silicate particle size determination. The pre-treatment procedures are listed as follow:

- i. Put about 0.5 g (depending on estimated sand content) sediment sample into a 50 mL centrifuge tube.
- ii. 30 mL of RO water is added into the tube and fully mixed with sediments through shaking. Subsequently, this sample is centrifuged for 5 minutes at 4500 rpm and then removing the supernatant. Repeat the process for 3 times to wash out the sea salt.
- iii. Add 10 mL 15% H₂O₂ and shake (loose the cap after shaking) to be well mixed. Then put the tubes into the ultrasonic bath to let it react for 1-2 days for removing the organic matter. If the reaction is not completed, repeat this step. After the process is completed, wash the sample with RO water for 2 times.
- iv. Add 7.5 mL 15% HCl and shake (loose the cap after shaking). Then put the tubes into the ultrasonic bath for 4 hours to remove the carbonates. If the reaction is not completed, repeat this step. After the effervescence is completed, wash the sample with RO water for at least 3 times (testing the pH value with pH-indicator paper).
- v. Add 10 mL dispersant (1% sodium hexametaphosphate) into the sample and shake before measurement.

Calculation of particle size statistical parameters (mean, sorting, skewness, kurtosis) can be divided into graphical method and moment method. In this study, the statistical parameters are performed by using moment method which brings the entire frequency

distribution into the determination rather than a few selected percentiles. Method of moments is calculated as below:



$$\text{Mean} = x = \frac{\sum f m_{\varphi}}{\sum f} \quad (1^{\text{st}} \text{ moment})$$

$$\text{Sorting} = \sigma = \sqrt{\frac{\sum f (m_{\varphi} - x)^2}{100}} \quad (2^{\text{nd}} \text{ moment})$$

$$\text{Skewness} = \frac{\sum f (m_{\varphi} - x)^3}{100 * \sigma^3} \quad (3^{\text{rd}} \text{ moment})$$

$$\text{Kurtosis} = \frac{\sum f (m_{\varphi} - x)^4}{100 * \sigma^4} \quad (4^{\text{th}} \text{ moment})$$

where f is the frequency (%) for each size class, and m_{φ} is the midpoint of each φ class.

According to Folk (1966), the geological meanings of the parameters are as follow:

Median (D₅₀): Median value of cumulative particle size distribution which is less susceptible to maximum or minimum values than the average (mean) particle size.

Sorting: The standard deviation (σ) of the particle size distribution, which also represents the degree of dispersion of the particle size in the sediments. The higher value reveals a worse sorting.

Skewness: The measure of asymmetry of the particle size distribution. A dominant population of coarse or fine grains will deviate the distribution curve away from a normal distribution (growing “tail” at one end of the distribution curve).

Kurtosis: The measure of peakedness of the particle size distribution. The size difference between two populations in a mixture will determine the distribution that goes to platykurtic (two equivalent population size) or leptokurtic (two very different population size).



2.3.5 Geochemical Analysis

The elements measured in this study include Mg, Al, K, Ti, Fe, Mn, Zn, Cr, Pb, Co, Ni, Cu, Cd. The total concentration of the above metals were determined after digestion of the sediment samples. Measurement was performed on the acid-digested sediment solutions. Flame Atomic Absorption Spectrometer (FAAS) and Inductively Coupled Plasma Mass Spectrometer (ICP-MS) were employed to determine the total content of the elements in the sediments and ensure the accuracy of the data set in this study.

(1) Sample Pre-treatment (Removal of Sea Salt)

The sediments were washed by ultrapure water (18.2 M Ω .cm) to remove any remaining sea salt and then freeze-dried before digestion. About 0.5 g of the sediment sample was transferred into a 50 mL polypropylene centrifuge tube (BD Falcon™) by a plastic spatula. 40 mL of ultrapure water (18.2 M Ω .cm) was also added to the tube and fully mixed with sediment through shaking. The sample was centrifuged for 5 minutes at 4500 rpm and the supernatant was removed. Repeat the process for 3 times and then this washed sediment sample was brought to freeze-dry for 3 days.

(2) Total Digestion

The pre-treated sediments were placed in drying oven overnight to remove water content prior to total digestion. The sediments were digested with multiple acids (HNO₃, HF and HClO₄), and the procedure is shown as below:

- i. Put 0.5 g of the pre-treated (salt-free and water-free) sediment into a cleaned Teflon beaker.



- ii. 5 mL of HNO₃ (Nitric acid 65%, Merck EMSURE[®]) is added to the sample and heated on the hot plate at 150°C for 2-3 hours with lid.
- iii. Add 5 mL of HF (Hydrofluoric acid 40%, Merck EMSURE[®]) to the sample with continually heating overnight with lid.
- iv. Add 0.5 mL of HClO₄ (Perchloric acid 70-72%, Merck EMSURE[®]) to the sample and heated at 200°C overnight with lid.

*add sufficient HClO₄ and heated for a sufficient reaction time until a clear solution was obtained.
- v. Remove the lid to evaporate the solution to dryness (until it turns into a white biscuit).

*knock the beakers throughout the process to make the droplets on the beaker wall fall onto the beaker bottom, ensuring the whole sediment solution is all dried and condensed onto the white biscuit.
- vi. Add little volume of ultrapure water (18.2 MΩ.cm) onto the white biscuit and add 5 mL of HNO₃ (Nitric acid 65%, Merck EMSURE[®]) to re-dissolve it. This solution was then boiled at 150°C for 1 hour with lid.
- vii. Take the solution sample off the hot plate and let it cool for 1 hour.
- viii. Put the solution into a 30 mL PP vial and bring the weight to about 25 g by adding ultrapure water (18.2 MΩ.cm).

*the lid and the interior wall of the beaker are washed by ultrapure water (18.2 MΩ.cm) and the beaker is swirled throughout the process to make the wall of the beaker clean and to prevent the loss of the sample.

**all the Teflon beakers should be cleaned by adding 5 mL of HNO₃ (Nitric acid 65%, Merck EMSURE[®]) through boiling with lid at 200°C for 2 hours. And the acid-washed

beakers are then rinsed by ultrapure water (18.2 MΩ.cm) and get fully dried before usage.

**all the PP vials for storing the digested samples should be soaked in 10% (v/v) HNO₃ for 3 days, triple-rinsed by ultrapure water (by Merck Millipore Milli-Q-Pod®) and dried in the hood in the clean room before usage.

**Each acid-digested sample was measured in weight unit (wt%), which was then converted into volumetric concentration (g/mL) by its density (obtained from the weight measured during the dilution step).

(3) Measurement

The concentrations of the elements were determined by external standard method using the ICP element standard solutions (Merck). Digested sample solutions were diluted (with 2% HNO₃ solution) to ensure that the measured results fall in the linear dynamic range of calibration curve. The linear dynamic range of the calibration curve for each element is shown in Table 2-4. The diluted sample solutions were analyzed using FAAS (iCE 3000 SERIES, Thermo) from Professor Liang-Saw Wen's Lab in IONTU and ICP-MS (iCapQs, Thermo) from the Exploration & Development Research Institute, CPC, analyzed by In-Tian Lin, see the analytical settings in Table 2-2 and Table 2-3.

**All the dilution procedure was conducted in the clean room.

**All the PE vials for storing the diluted samples should be soaked in 10% (v/v) HNO₃ for over 3 days and then triple-rinsed with ultrapure water (by Merck Millipore Milli-Q-Pod®) and dried in the hood of clean room prior to use.

**The diluent 2% HNO₃ solution is diluted from the ultrapure nitric acid (Nitric Acid

ULTREX[®] II Ultrapure Reagent, J.T.Baker)

**Multi-element mixed external standard solutions were prepared from 1000 mg/L of the following ICP element standard solutions from Merck company:



a. Certipur[®] ICP multi-element standard solution IV, MERCK

1000 mg/L: Ag, Al, B, Ba, Bi, Ca, Cd, Co, Cr, Cu, Fe, Ga, In, K, Li, Mg, Mn, Na, Ni, Pb, Sr, Tl, Zn (23 elements in diluted nitric acid) (contains nitric acid, nickel(II) nitrate)

b. Certipur[®] Titanium ICP standard solution, MERCK

1000 mg/L: Ti (traceable to SRM from NIST (NH₄)₂TiF₆ in H₂O)

(4) Quality Assurance and Quality Control

Quantification of all elements measured in this study was based on calibration lines established by the ICP multi-element standard solutions from Merck. Precision and accuracy of the data were assured through repeated analysis (n =4) of certified reference material PACS-3 (Marine Sediment Reference Material for Trace Metals and other Constituents) from National Research Council Canada (NRC). With the exception of Zn (98%) and Cu (82%), the results for most of the elements are shown within 90 ± 5% of the certified values, see Table 2-5. The precision for the analysis of certified reference material for all elements is better than 5% (all RSD<5%). All samples were measured with 3 replicates and average values are reported. Most (97%) of the reported data lies within 2 standard deviations of the mean, which can empirically account for 95% of probability close to certainty. Repeated analysis of the calibration solution (0.2 ppm) were arranged between every 10-15 samples to monitor the instrumental shift over the duration of measurements and the shift has been corrected.

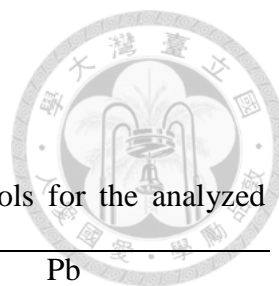


Table 2-2

The detailed FAAS (iCE 3000 SERIES, Thermo) analytical protocols for the analyzed element of Zn and Pb.

Element	Zn	Pb
Lamp Current (mA)	75	75
Wavelength (nm)	213.9	217.0
Bandpass (nm)	0.2	0.5
Fuel Flow (L/min, C ₂ H ₂)	0.9	1.1
D ₂ Lamp Correction	✓	✓

Table 2-3

The detailed ICP-MS (iCapQs, Thermo) analytical protocols for the analyzed element of Mg, Al, K, Ti, Fe, Mn, Cr, Co, Ni, Cu, Cd.

Parameter	Value
Nebulizer	PFA
Injector	Quartz 2.5 mm ID
Spray Chamber	Quartz, cyclonic
interface	Pt cone
Plasma mode	KEDs
RF forward power (W)	1550
Sampling depth (mm)	4.7
Nebulizer gas Flow (L/min)	1.02
Spray Chamber Temperature (°C)	2.7
He cell gas flow (mL/min)	4.2



Table 2-4

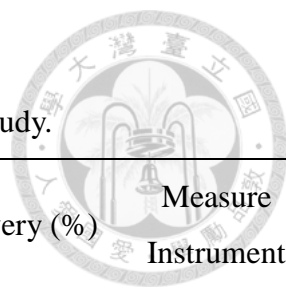
The concentrations of the standard used to build the calibration line for each element in FAAS (iCE 3000 SERIES Thermo) and ICP-MS (iCapQs, Thermo).

Element	Std 1	Std2	Std3	Std4	Std5	Std6	Instrument
Mg	0.1	0.2	0.5	1.0	-	-	ICP-MS
Al	0.1	0.2	0.5	1.0	-	-	ICP-MS
K	0.1	0.2	0.5	1.0	-	-	ICP-MS
Ti	0.1	0.2	0.5	-	-	-	ICP-MS
Fe	0.1	0.2	0.5	1.0	-	-	ICP-MS
Mn	0.1	0.2	0.5	1.0	-	-	ICP-MS
Sr	0.1	0.2	0.5	1.0	-	-	ICP-MS
Zn	0.1	0.2	0.5	1.0	-	-	FAAS
Cr	0.1	0.2	0.5	1.0	-	-	ICP-MS
Pb	0.1	0.2	0.5	1.0	2.0	5.0	FAAS
Co	0.1	0.2	0.5	1.0	-	-	ICP-MS
Ni	0.1	0.2	0.5	1.0	-	-	ICP-MS
Cu	0.1	0.2	0.5	1.0	-	-	ICP-MS
Cd	0.1	0.2	0.5	1.0	-	-	ICP-MS

All linear least square fits to the calibration line are better than 0.999 ($R^2 > 0.999$).

Table 2-5

The results of the Certified Reference Material PACS-3 analyzed in the study.



Element	Certified Value (mean±2sd)	This Study *(mean±2sd)	RSD (%)	Recovery (%)	Measure Instrument
Mg (%)	1.402 ± 0.058	1.259 ± 0.055	1.5	90	ICP-MS
Al (%)	6.58 ± 0.12	6.15 ± 0.23	4.0	93	ICP-MS
K (%)	1.253 ± 0.040	1.162 ± 0.044	2.1	93	ICP-MS
Ti (%)	0.442 ± 0.018	0.384 ± 0.021	2.5	87	ICP-MS
Fe (%)	4.106 ± 0.064	3.897 ± 0.190	2.0	95	ICP-MS
Mn (µg g ⁻¹)	432 ± 16	386 ± 11	3.4	89	ICP-MS
Sr (µg g ⁻¹)	267 ± 10	239 ± 7	4.6	89	ICP-MS
Zn (µg g ⁻¹)	376 ± 12	370 ± 8	3.1	98	FAAS
Cr (µg g ⁻¹)	90.6 ± 4.0	82.7 ± 2.4	4.1	91	ICP-MS
Pb (µg g ⁻¹)	188 ± 7.4	178 ± 5.3	1.9	94	FAAS
Co (µg g ⁻¹)	12.1	10.7 ± 0.3	3.0	88	ICP-MS
Ni (µg g ⁻¹)	39.5 ± 2.2	35.2 ± 0.9	1.8	89	ICP-MS
Cu (µg g ⁻¹)	326 ± 10	268 ± 6	4.3	82	ICP-MS
Cd (µg g ⁻¹)	2.23 ± 0.16	1.97 ± 0.04	3.8	88	ICP-MS

*n=4

Chapter 3 Results and Discussions



The sediment cores analyzed in this study are from three different sedimentological regimes, including (I) sites at lateral sides of GPSC on the Gaoping Slope which are proximal to the point source of GPR, (II) one site on the Palm Ridge at the head of Penghu Submarine Canyon which receives sediments from other sources than GPR, and (III) two deep sea sites next to the lower reach of GPSC which are along the major pathway for the terrestrial materials discharged from GPR but distal to the major source. The following results will be compared between these regions.

3.1 Sedimentary Properties

Before presenting the results of this study, the sedimentary features of each cores will be introduced based on the ^{210}Pb dating and grain size data obtained from previous studies (鄭, 2012; 蔡, 2014; 林等人, 2016).

3.1.1 Gaoping Continental Slope Site: S2, S6, S1 and B4G

S2, S6, S1 and B4G are located in the intraslope basins on the Gaoping Slope, the GPSC divides them into two symmetric parts, where S2 and S6 are located at west side of the GPSC, while S1 and B4G are situated at the east side of the GPSC. In S2, S6 and B4G cores, the ^{210}Pb activity decreased exponentially with increasing depth, indicating a constant sediment accumulation rate with no significant particle mixing process (Figure 3-1; Figure 3-2; Figure 3-4). In core S1, a small decline in ^{210}Pb activity within the subsurface layer, but for most of the profile it still follows an exponential decay pattern (Figure 3-3). For the grain size data, the median grain size in most cores fall

between fine and very fine silt (most of them falls around 7ϕ). However, B4G has more variations in the grain size profiles and it can be noted that there's a decline in the median grain size profile, high sorting value, and an increase in the coarser grain fraction at the depth of 5.5 cm which can indicate an event layer. The sedimentation rates derived from the excess ^{210}Pb in these cores are as follow: **S2**: 0.06 cm/yr; **S6**: 0.04 cm/yr; **S1**: 0.13 cm/yr; **B4G**: 0.02 cm/yr.

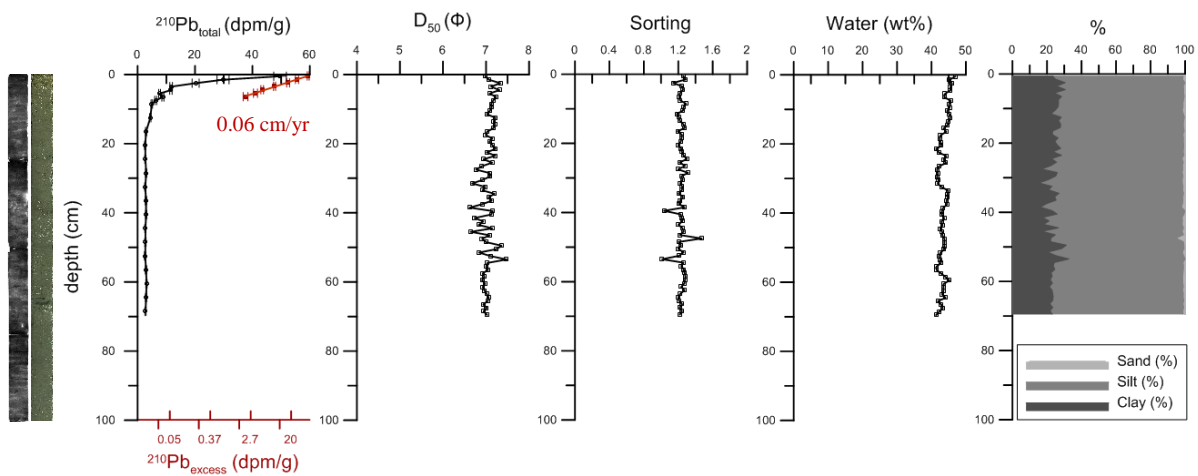


Figure 3-1 The X-Radiography, core surface image, and profiles of ^{210}Pb , water content and grain size in core S2.

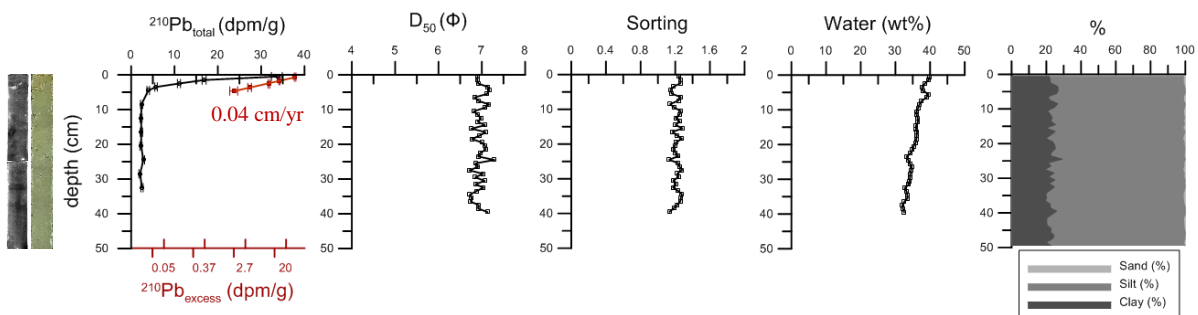


Figure 3-2 The X-Radiography, core surface image, and profiles of ^{210}Pb , water content and grain size in core S6.

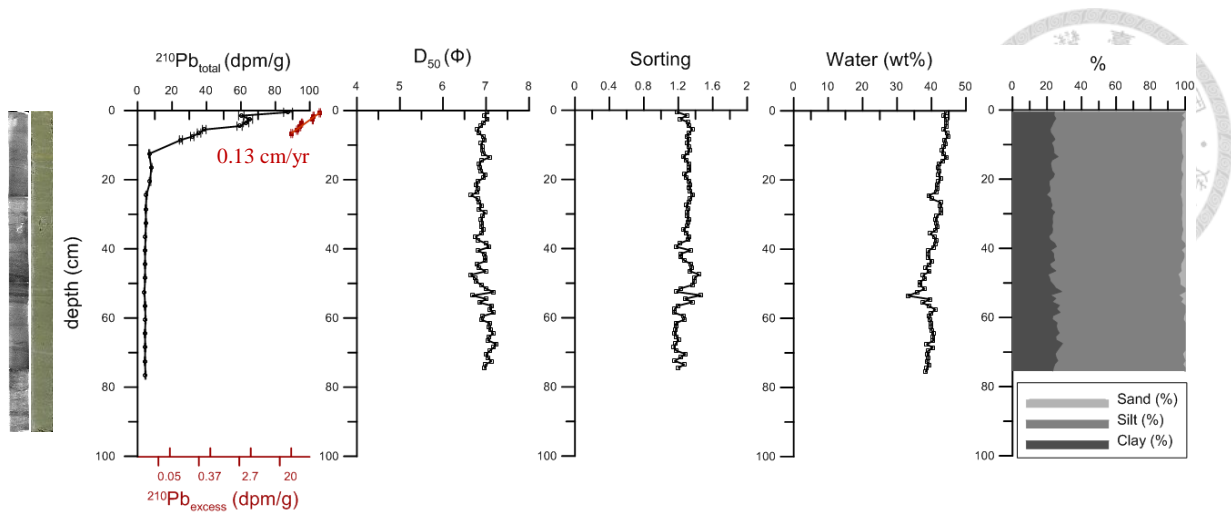


Figure 3-3 The X-Radiography, core surface image, and profiles of ^{210}Pb , water content and grain size in core S1.

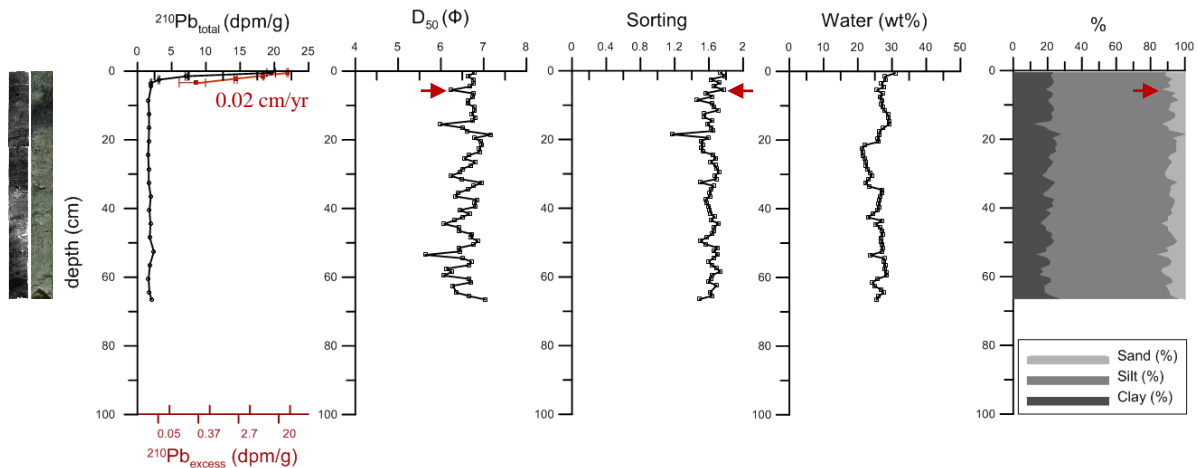


Figure 3-4 The X-Radiography, core surface image, and profiles of ^{210}Pb , water content and grain size in core B4G. The red arrow indicates the layer (5.5 cm) with coarser median grain size (D_{50}), bad sorting, and increasing coarser fraction that can suggest an event layer, which will be discussed in the later section.

3.1.2 Deep Sea Site: MT6 and MT7

MT6 and MT7 are located on the west side of the lower reach of GPSC, close to the intersection of GPSC and Penghu Submarine Canyon, MT7 is located on the Tsan-Yao Ridge and MT6 is located in the basin on the west side of the ridge with a

water depth of 2654 and 3078 m, respectively (Figure 3-7). The sedimentary records between these two nearby sites are very different. A thick turbidite layer in the upper 25 cm revealed two natural geohazards, including 2006 Pingtung Earthquake and 2009 Morakot Typhoon, were recorded in MT7 (Figure 3-6). In contrast, the ^{210}Pb profile of MT6 shows a relatively steady sedimentation environment (Figure 3-5). It's suggested that the discrepancy existing between these two sites can be controlled by terrain, the relief between these two sites is more than 500 meters. When natural geohazards delivered tremendous sediment masses down to the sea, these sediments would be transported as sediment flows through the GPSC and suspended particles can be deposited on the ridge top without direct deposition in the basin area (MT6) right next to the ridge. However, in the deeper part of MT6, the grain size profile shows paleo-event layers at depth of 35-48 cm (Figure 3-5). The sedimentation rates derived from the excess ^{210}Pb for MT6 and MT7 are 0.04 and 0.06 cm/yr, respectively. In MT7, the sedimentation rate is derived by taking no regard to the upper 25 cm event layer.

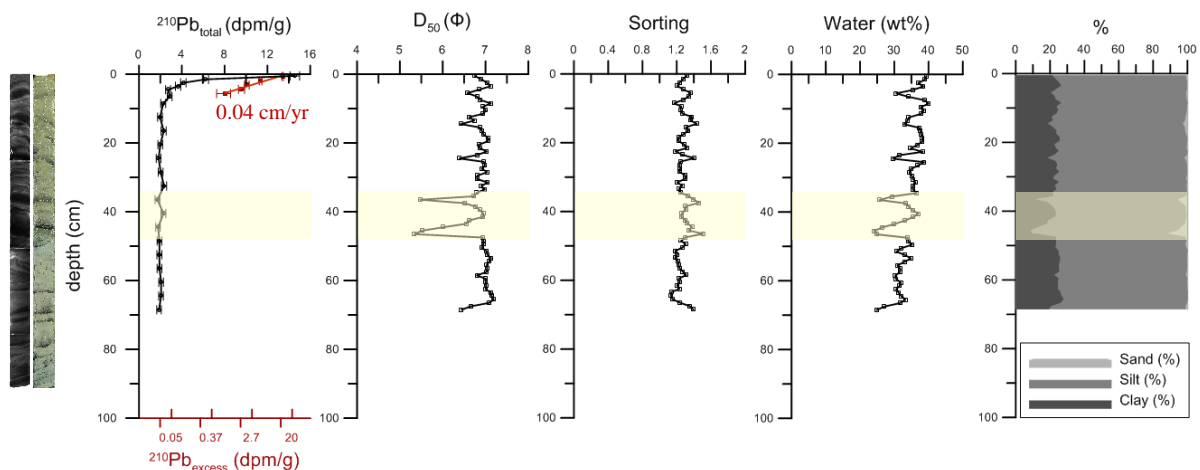


Figure 3-5 The X-Radiography, core surface image, and profiles of ^{210}Pb , water content and grain size in core MT6. Two major paleo-event layers are identified by the coarser median grain size (D_{50}) and the increase of sorting values at the depth of 36.5 and 46.5 cm (yellow shaded area).

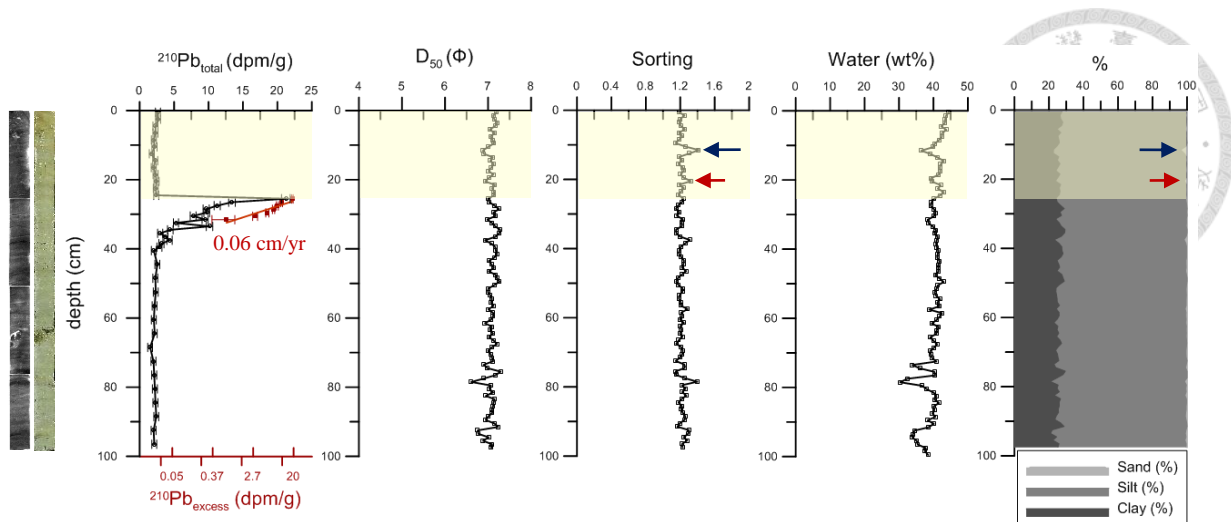


Figure 3-6 The X-Radiography, core surface image, and profiles of ^{210}Pb , water content and grain size in core MT7. Two event layers which produced by 2006 Pingtung Earthquake (red arrow) and 2009 Morakot Typhoon (blue arrow) were identified in the upper 25 cm through two distinct peaks in sorting and increasing amount of coarser grain fraction.

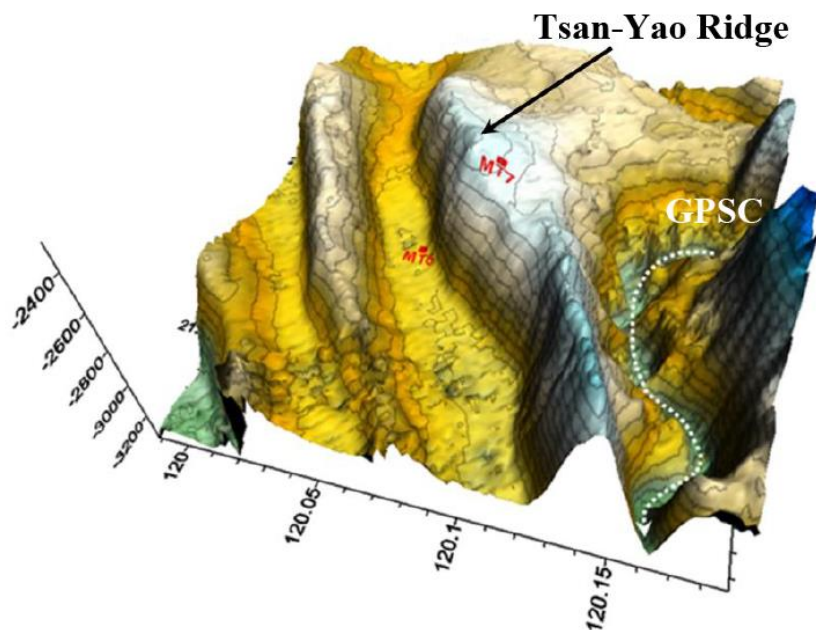
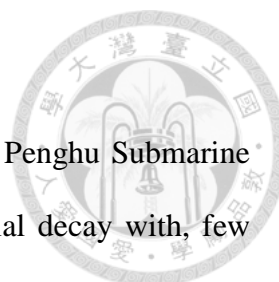


Figure 3-7 The topographic map showing the location of core MT6 and MT7. MT7 is on the ridge top of Tsan-Yao Ridge and MT6 is in the basin next to the ridge. The white dot line is the Gaoping Submarine Canyon (GPSC) with the arrow indicating the direction of lower reach of GPSC (modified from 蔡, 2014).



3.1.3 Penghu Submarine Canyon Site: PL02

PL02 is a site located on the Palm Ridge close to the head of Penghu Submarine Canyon. The profile of ^{210}Pb at this site shows a steady exponential decay with, few variations in the grain size profiles (Figure 3-8). The median grain size at this site falls in the range of fine silt. The sedimentation rate derived from the excess ^{210}Pb at this site is 0.06 cm/yr.

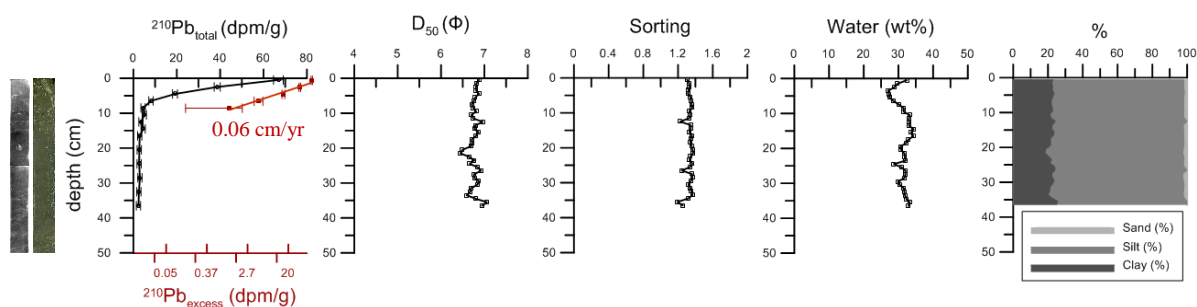


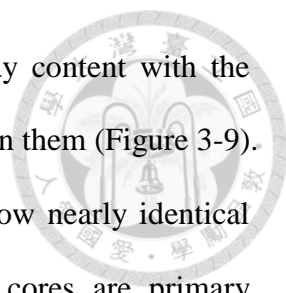
Figure 3-8 The X-Radiography, core surface image, and profiles of ^{210}Pb , water content and grain size in core PL02.

3.2 Major Element Ratios

3.2.1 Reference Element (Al)

The concentrations of Al in each sediment core are in the ranges as follow: **PL02**: 4.7-7.37%, with a mean of 6.2%; **S2**: 7.7-8.7%, with a mean of 8.2%; **S6**: 8.1-9.33%, with a mean of 8.5%; **S1**: 7.7-10.2%, with a mean of 8.7%; **B4G**: 6.8-7.4%, with a mean of 7.1%; **MT6**: 7.16-9.6%, with a mean of 8.6%; **MT7**: 7.5-9.5%, with a mean of 8% (see Appendix).

Figure 3-9 shows the vertical distribution of Al in each sediment core. In most of the sediment cores, the temporal fluctuation of Al is small. Since aluminosilicate is the major component in clay minerals, Al tends to be enriched in such fine-grained clay



during weathering and transport processes. If we compare the clay content with the distribution of Al, we do find a highly correlated relationship between them (Figure 3-9). In core S2, S6, B4G, MT6 and MT7, the clay and Al contents show nearly identical patterns in the profiles, indicating the variation of Al in these cores are primary controlled by the grain size and composition of the sediments. However, in S1 and PL02, the clay fractions show little variations with depth while the Al concentrations present more fluctuations over time, showing S1 and PL02 sites may represent a less stable sedimentary environment.

Moreover, Al is a very immobile element in natural environment which can scarcely affect by the changes in environmental conditions and has no significant anthropogenic input, so this element is often regarded as a proxy to crustal or terrestrial materials and has been widely used as the reference element to eliminate the effect caused by grain size and to determine the source of other elements.

In this study, we also use Al as the reference element to eliminate the effects caused by grain size and calculate the elements to Al ratios to be compared with the ratio in natural background (will introduce in the following section) to discuss the enrichment of each element and the possible source for the elements.

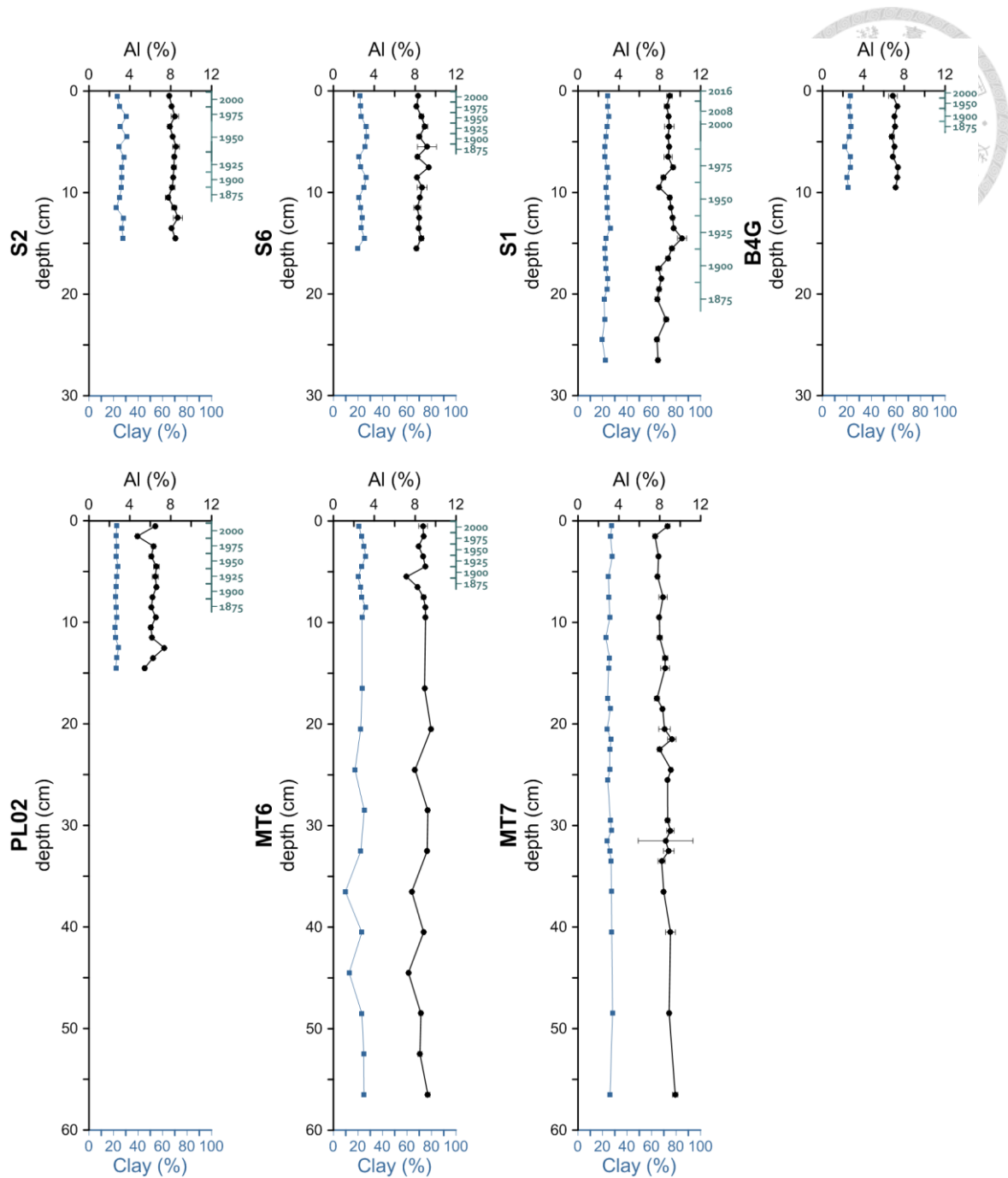
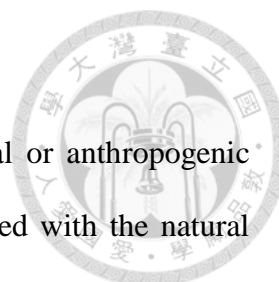


Figure 3-9 Vertical distributions of Al with comparison to the clay fraction (blue line) in each sediment core analyzed in this study. All the cores show little variations in the Al concentrations over time and the variations can usually correlate to the clay fractions in the sediments.



3.2.2 Reference Backgrounds

Since metal content in sediments can be derived from natural or anthropogenic sources, the observed elemental concentrations are usually compared with the natural abundances of the elements in the Earth's crust for accessing the level of excess elements in sediments. In this study, Al is used as the reference element for it is the dominant element in crust and not susceptible to the variations of environmental condition. Elements to Al ratios are then compared to the natural backgrounds, when “ $(M/Al)_{\text{sample}} \leq (M/Al)_{\text{background}}$ ”, it represents the element of interest is entirely from the crustal contribution (natural weathering); while the “ $(M/Al)_{\text{sample}} > (M/Al)_{\text{background}}$ ” can indicate that there can be an important proportion of elements delivered from non-crustal materials, which might be sourced from a biogenic or anthropogenic source.

However, the abundance of elements in different areas may indicate regional differences in composition of the source rock. Therefore, in this study, we not only measured the total concentration of trace elements, but also determined the concentration of major elements in the sediments, trying to get a more reliable background value in the study area.

The major elements measured in this study include Mg, Al, K, Ti and Fe, all of which are the dominated elements in the natural matrix and are resistant to weathering and can reflect a regional composition of the source rock. Compared to previous study conducted in the shallow water (Chen & Selvaraj, 2008), all major elements normalized by Al (Ti/Al, Fe/Al, Mg/Al, K/Al) in sediments off southwestern Taiwan show a relatively consistent value in different geographic zones (Table 3-1). Based on the major elements/Al ratio and considering the possible provenance of the study area, several reference materials are used in this study for the trace metals source identification. These reference materials include Upper Continental Crust (UCC) by Hu & Gao (2008),

Average Composition of Sedimentary rocks of Taiwan (ACST) by Lan et al. (2002), Upper Crust of Yangtze Craton (UC-YC) by Gao et al. (1998), and Average Shale by Turekian & Wedepohl (1961), the background ratios of M/Al in these materials are shown in Table 3-2. The comparison of major element/Al ratios between samples and these reference materials are shown in Figure 3-10-Figure 3-13. Similar to the distribution of Al, all the other measured major elements (Ti, Fe, Mg, K) present a relatively consistent level in all analyzed sediment cores, indicating there is a steady natural input source for all these major elements.

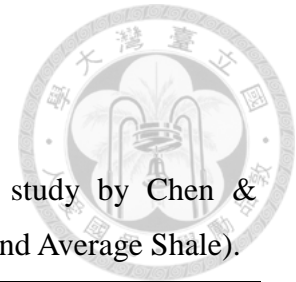


Table 3-1

The mean major element/Al mass ratios compared to previous study by Chen & Selvaraj (2008) and the reference materials (UCC, ACST, UC-YC, and Average Shale).

	Ti/Al	Fe/Al	Mg/Al	K/Al
Bed sediment, Gaoping River ^a	0.049	0.51	0.12	0.26
Coastal sediments ^a (n=8) (water depths: <100 m)	0.049	0.47	0.16	0.30
Offshore sediments ^a (n=12) (water depths: 105–537 m)	0.054	0.49	0.15	0.28
Gaoping Slope (water depth: 618-1205 m)	0.050	0.50	0.15	0.29
Deep Sea (water depth: 2654-3078 m)	0.050	0.50	0.15	0.29
Penghu Submarine Canyon (water depth: 931m)	0.060	0.52	0.16	0.34
Mean of this study	0.051	0.50	0.15	0.30
UCC ^b	0.049	0.45	0.15	0.34
ACST ^c	0.049	0.44	0.14	0.33
UC-YC ^d	0.052	0.50	0.19	0.29
Average Shale ^e	0.058	0.59	0.19	0.33

The values for **Gaoping Slope** is the mean values of all analyzed depths in S2, S6, S1 and B4G (at lateral sides of the upper reach of GPSC). The values for **deep sea** is the mean values of all analyzed depths in MT6 and MT7. The values for **Penghu Submarine Canyon** is the mean values of all analyzed depths in PL02. The values for **mean of this study** are the mean values of all analyzed depths in all cores (S2, S6, S1, B4G, PL02, MT6, MT7).

^a Chen & Selvaraj (2008): The coastal sediments were collected adjoining Kaohsiung Harbor and the offshore sediments were collected in or around the old and new slag dumping sites of China Steel Corporation off southwestern Taiwan (red square and star in Figure 3-15). Surface sediments (0-2.5 cm) are used for their study.

^b Upper Continental Crust, Hu & Gao (2008)

^c Average Composition of Sedimentary rocks of Taiwan, Lan et al. (2002)

^d Upper Crust of Yangtze Craton, Gao et al. (1998)

^e Turekian & Wedepohl (1961)

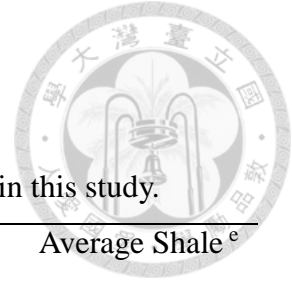


Table 3-2

The background ratios of M/Al in different reference materials used in this study.

M/Al	UCC ^b	ACST ^c	UC-YC ^d	Average Shale ^e
Mg/Al	0.15	0.14	0.19	0.19
K/Al	0.34	0.33	0.29	0.33
Ti/Al	0.049	0.049	0.052	0.058
Fe/Al	0.45	0.44	0.50	0.59
Mn/Al*1000	9.46	9.26	10.41	10.63
Zn/Al*1000	0.92	1.13	0.96	1.19
Cr/Al*1000	0.90	1.33	0.91	1.13
Pb/Al*1000	0.31	0.29	0.23	0.25
Co/Al*1000	0.18	0.13	0.22	0.24
Ni/Al*1000	0.42	0.31	0.51	0.85
Cu/Al*1000	0.33	0.33	0.48	0.56
Cd/Al*1000	0.0007	ND	0.0011	0.0038

ND=No Data.

^b Upper Continental Crust, Hu & Gao (2008)

^c Average Composition of Sedimentary rocks of Taiwan, Lan et al. (2002)

^d Upper Crust of Yangtze Craton, Gao et al. (1998)

^e Turekian & Wedepohl (1961)

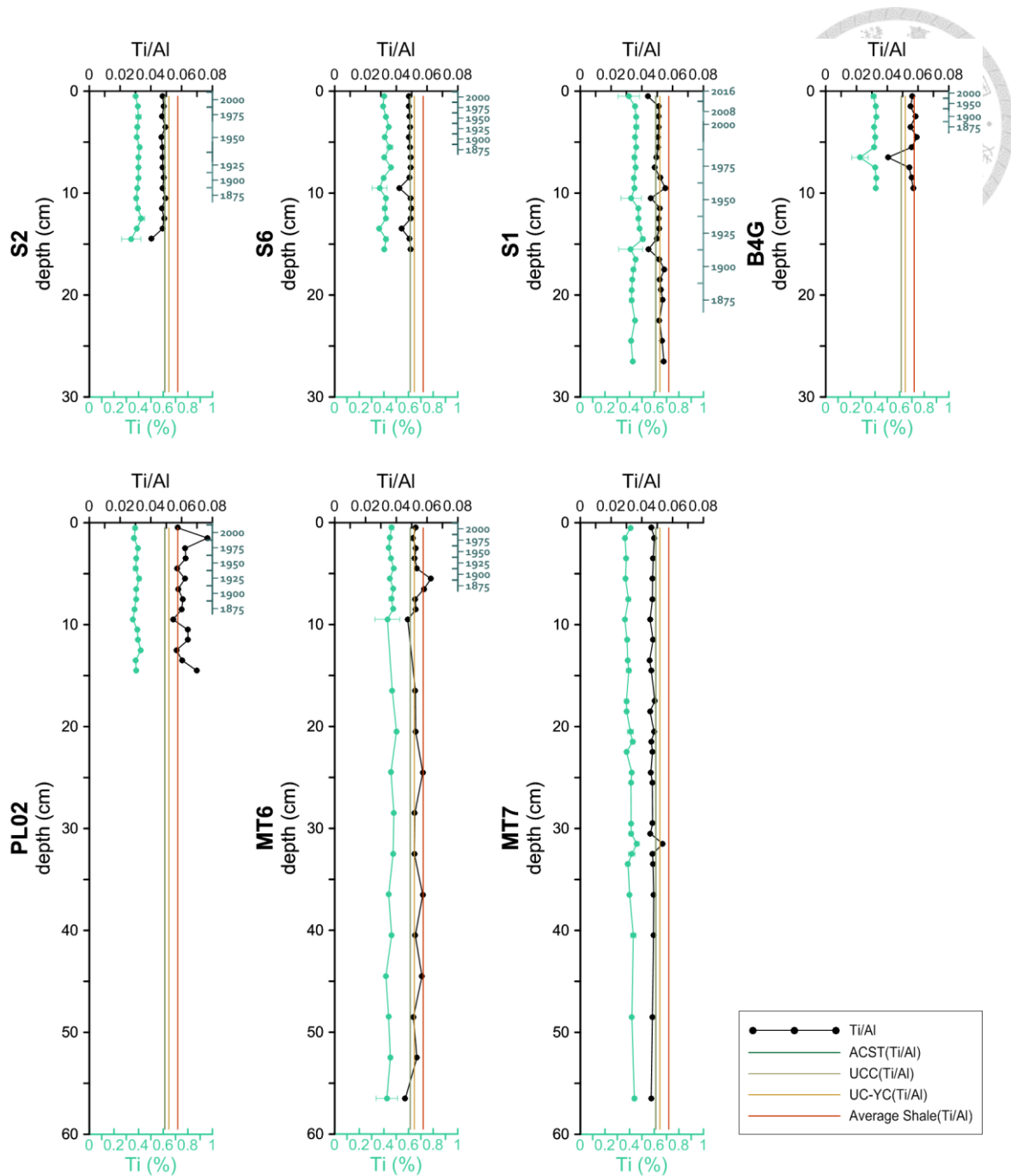


Figure 3-10 Down core Ti/Al ratio with comparison to the reference background materials (ACST, UCC, UC-YC, Average Shale) in each sediment core analyzed in this study. Most cores have a stable Ti/Al ratio over time and their values are closer to the reference material of ACST and UCC.

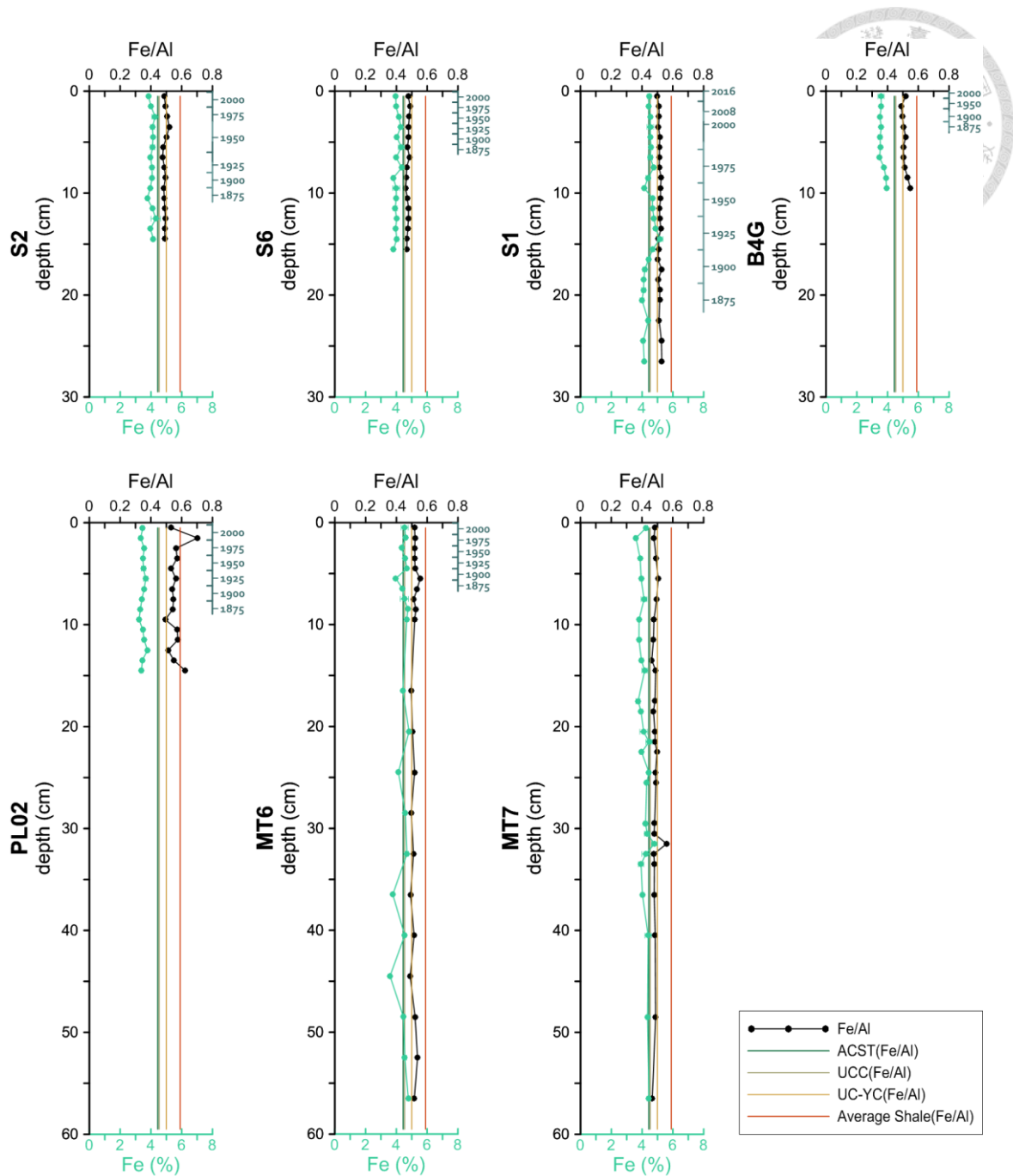


Figure 3-11 Down core Fe/Al ratio with comparison to the reference background materials (ACST, UCC, UC-YC, Average Shale) in each sediment core analyzed in this study. Most cores have a stable Fe/Al ratio over time and their values are closer to the reference material of UC-YC.

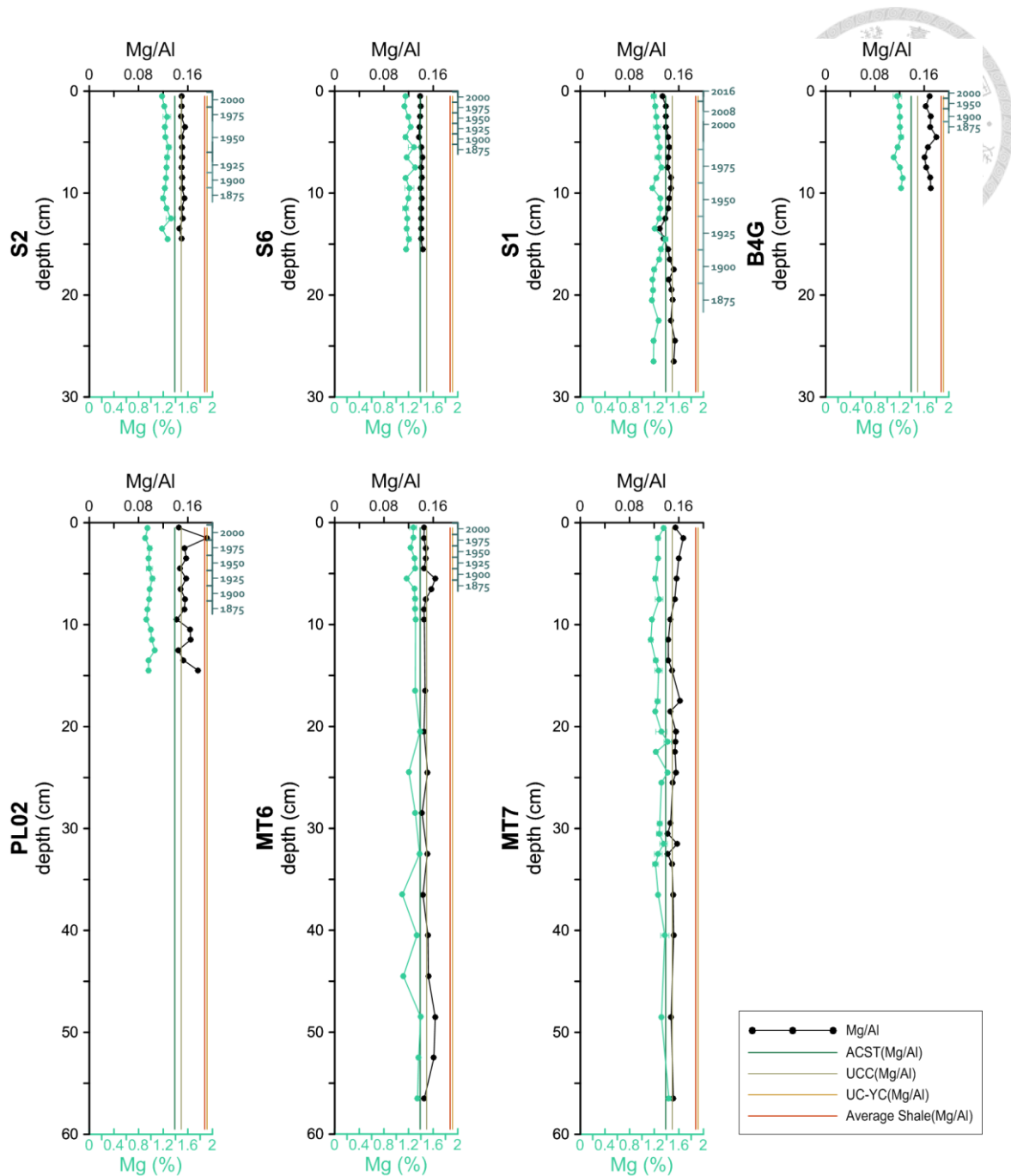


Figure 3-12 Down core Mg/Al ratio with comparison to the reference background materials (ACST, UCC, UC-YC, Average Shale) in each sediment core analyzed in this study. Most cores have a stable Mg/Al ratio over time and their values are closer to the reference material of ACST and UCC.

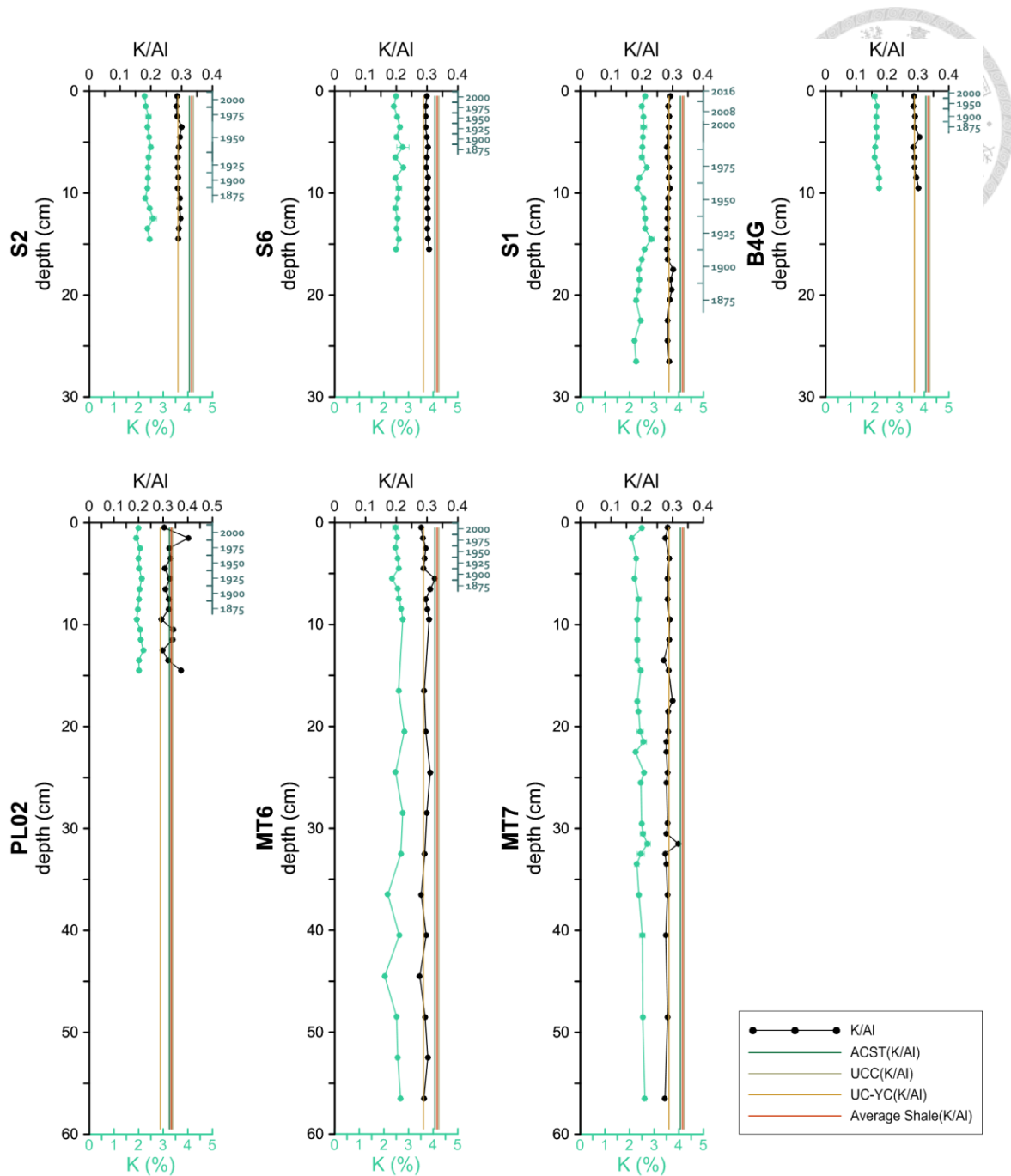
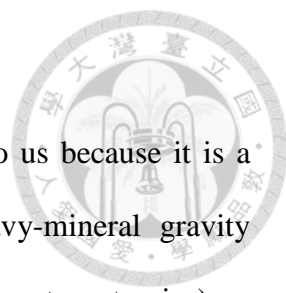


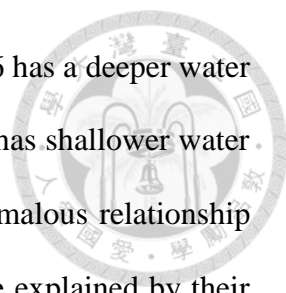
Figure 3-13 Down core K/Al ratio with comparison to the reference background materials (ACST, UCC, UC-YC, Average Shale) in each sediment core analyzed in this study. Most cores have a stable K/Al ratio over time and their values are closer to the reference material of UC-YC.

3.2.3 Ti/Al Molar Ratio



Among these major element ratios, Ti/Al ratio is of interest to us because it is a good proxy for the sediment transportation process due to heavy-mineral gravity fractionation (Chen et al., 2013). Either river systems (downstream to estuaries) or marine environment (shallow to deep water), sink areas are typically found to have lowered Ti/Al molar ratio as heavy minerals, which usually rich in Ti, will deposit former during the transport process (Chen et al., 2013). The initial Ti/Al molar ratio is determined by the source rock, once the particles separated from the parent material, the ratio can reflect the transportation process. This has also been examined in Gaoping River system by Chen et al. (2013), the Ti/Al molar ratio (expressed as 100Ti/Al molar ratio) in fluvial sediments (temporary sinks, Figure 3-14a) are slightly lowered than the adjacent surface soils (source materials, Figure 3-14b), and it also showed the downstream decreasing trend and mixing values at the junction of the river. All evidence suggests the Ti/Al molar ratio can be used as a reliable proxy to reflect the transportation process. Their results revealed that the Ti/Al molar ratio in fluvial sediments of the Gaoping River system is 2.50 to 3.89 (Figure 3-14a), and 2.73 to 3.94 in surface soils (Figure 3-14b).

Compared to previous studies conducted in GPR and shallow water (Chen et al., 2013; Chen & Selvaraj, 2008), if we don't regard the relatively high Ti/Al value observed in the offshore sediments (slag dumping site, Ti is also an additive to steel) and B4G (Table 3-3), a decreasing trend in Ti/Al molar ratio can be observed from the upstream of GPR (source) to Gaoping slope (temporary sink) (Figure 3-15). However, for the sediment transport path from the Gaoping Slope to the deep sea sites, there is no obvious decreasing trend between these two geographic zones, where MT6 (2.92) and MT7 (2.66) have almost the same or even higher values than those in Gaoping slope (S1:



2.67; S2: 2.71; S6: 2.72). Moreover, in these two deep sea sites, MT6 has a deeper water depth (3078m) but with higher Ti/Al molar ratio (2.92), while MT7 has shallower water depth (2654m) but with a lower Ti/Al molar ratio (2.66). This anomalous relationship between water depth and Ti/Al molar ratio in these two sites can be explained by their topographic characteristic, since MT7 is on the ridge top while MT6 is in the deep basin where can be more likely to be a sink for those heavy minerals, revealing that topography can also be an important control on the Ti/Al molar ratio during the sediment transport. Though the Ti/Al molar ratio in Gaoping River System display a clear and high resolution information on the sediment transportation process, the Ti/Al molar ratio along the further seaward transport path (coastal to deep sea sediments) doesn't reflect the same trend. The spatial distribution of Ti/Al ratio between the Gaoping Slope and deep sea sites might reveal an abrupt sediment transport process that the sediments discharged from GPR will bypass the narrow Gaoping Shelf, and together with the eroded materials from the Gaoping Slope, being fast transported and deposited a considerable amount of sediments into the deep sea basin.

At the Penghu Submarine Canyon site (PL02), it has higher major element/Al ratios than all other sites in this study, and their ratios can be compared to the ratios in the reference material UC-YC which also has higher ratios than that in UCC and ACST (Table 3-1), indicating this site can receive sediments from different sources.

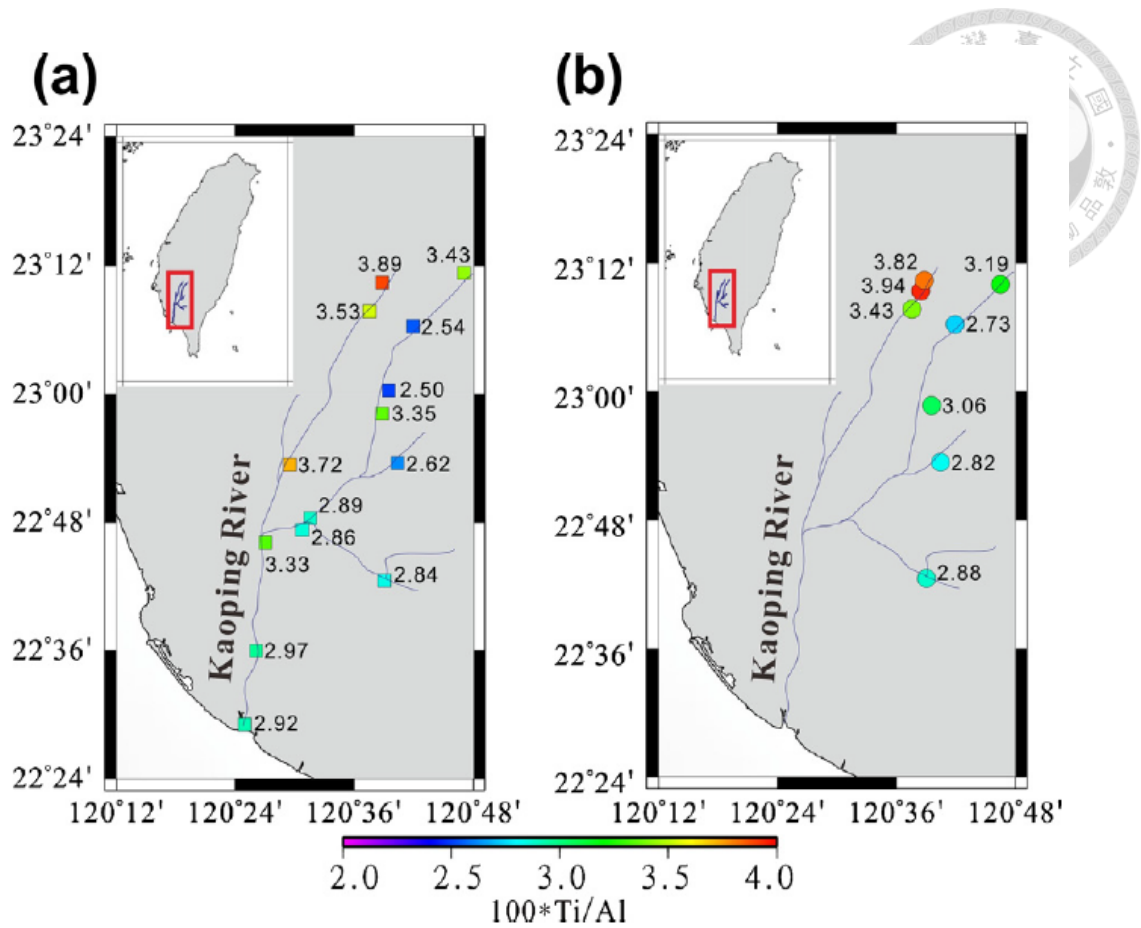


Figure 3-14 The Ti/Al molar ratios from (a) the fluvial sediments (temporary sinks) and (b) the surface soils (source materials) along the Gaoping (Kaoping) River drainage (Chen et al., 2013).



Table 3-3

The mean 100Ti/Al molar ratios in surface sediments along the Gaoping dispersal system.

Location	100Ti/Al molar ratio	
Gaoping River mouth ^f	2.92	
Coastal sediments ^a (water depths: <100 m)	2.76	
Offshore sediments ^a (water depths: 105–537 m)	3.04	
	S6 (water depth: 618m)	2.72
Gaoping Slope ^g	S2 (water depth: 1205m)	2.71
(water depth: 618-1205 m)	S1 (water depth: 822m)	2.67
	B4G (water depth: 863m)	3.15
Deep Sea ^g	MT7 (water depth: 2654m)	2.66
(water depth: 2654-3078 m)	MT6 (water depth: 3078m)	2.92
Penghu Submarine Canyon (water depth: 931m)	PL02 (water depth: 931m)	3.48

All the Ti/Al mass ratio data was recalculated as 100Ti/Al molar ratio by the function as follow: $100 Ti/Al \text{ molar ratio} = 100[Ti(\%)/47.867] \div [Al(\%)/26.982]$. (The molar mass of Ti is 47.867 g/mol; the molar mass of Al is 26.982 g/mol)

*all the values showed here was the mean 100Ti/Al molar ratios in the surface sediments.

^a Chen & Selvaraj (2008): uppermost 2.5 cm of core top (0-2.5 cm).

^f Chen et al. (2013): surface fluvial sediments.

^g This study: uppermost 2 cm of core top (0-2 cm).

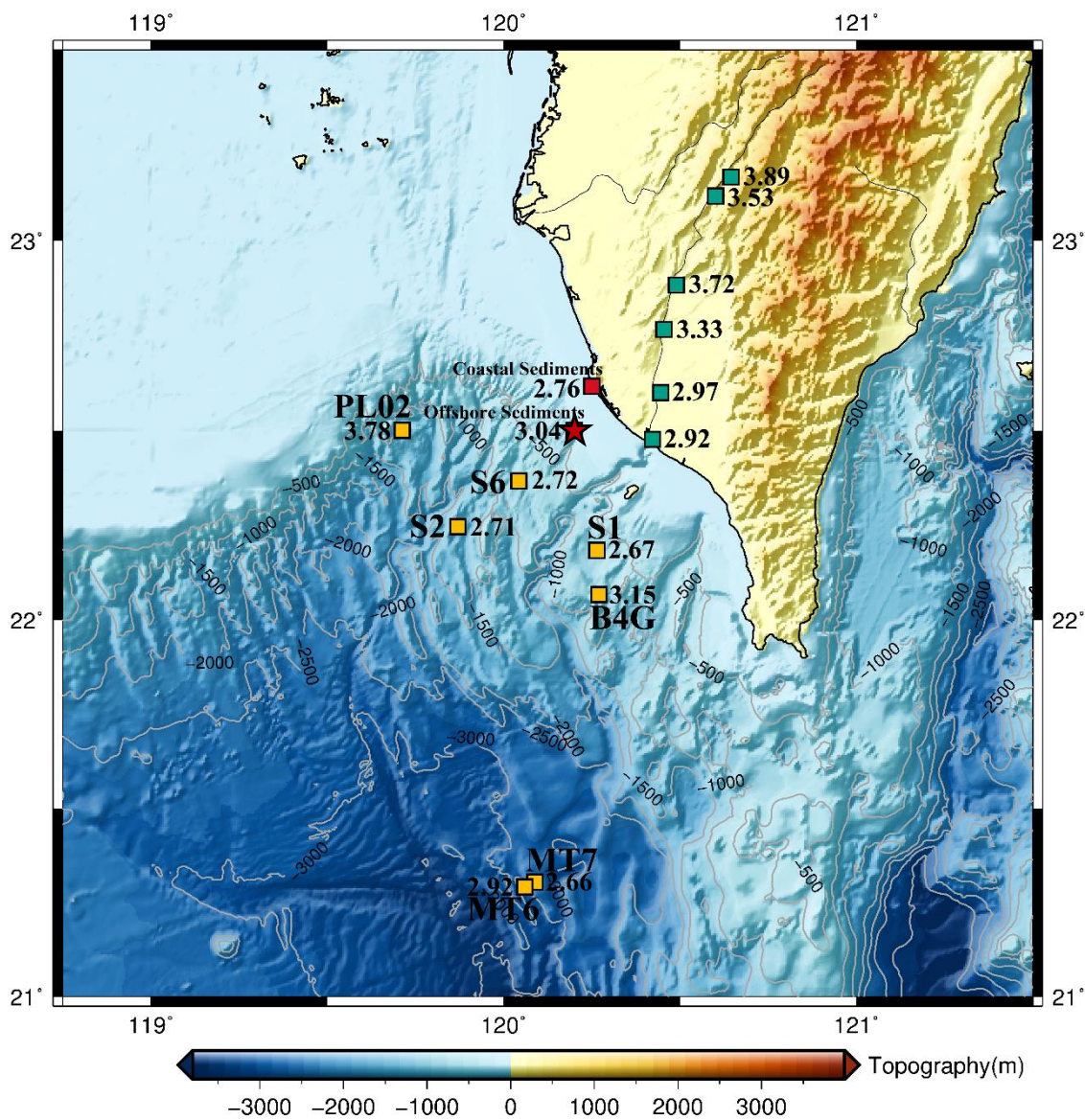


Figure 3-15 The spatial distribution of Ti/Al molar ratio compared to previous studies (green squares: Chen et al., 2013; red square: Chen & Selvaraj, 2008; yellow squares: this study). The number beside the square is expressed as “100Ti/Al molar ratio”. The offshore sediments from Chen & Selvaraj (2008) is collected in and around the old and new slag dumping sites (red star).

3.3 Vertical Distribution of the Metals



3.3.1 S2 (Gaoping Slope Site)

S2 is located on the west side of GPSC with a deeper water depth of 1205 m, and the concentration of each element at this site are as follow, **Al**: 7.7-8.7%, with a mean of 8.2%; **Fe**: 3.8-4.3%, with a mean of 4.1%; **Mn**: 335-2022 $\mu\text{g/g}$, with a mean of 513 $\mu\text{g/g}$; **Zn**: 95-103 $\mu\text{g/g}$, with a mean of 99 $\mu\text{g/g}$; **Cr**: 51-77 $\mu\text{g/g}$, with a mean of 68 $\mu\text{g/g}$; **Pb**: 16-27 $\mu\text{g/g}$, with a mean of 19 $\mu\text{g/g}$; **Co**: 11.7-13.9 $\mu\text{g/g}$, with a mean of 12.5 $\mu\text{g/g}$; **Ni**: 30.0-34.2 $\mu\text{g/g}$, with a mean of 31.4 $\mu\text{g/g}$; **Cu**: 17-20 $\mu\text{g/g}$, with a mean of 18 $\mu\text{g/g}$; **Cd**: 0.12-0.20 $\mu\text{g/g}$, with a mean of 0.15 $\mu\text{g/g}$ (see Appendix).

Except for Cr and Cd, most of the trace metals at this site shows little variations over time, and their ratio to Al all appears around or under the ratio of natural backgrounds (Figure 3-16), implying most of them are from natural sources. However, Mn and Pb show a sharp increase in the uppermost layer of this sediment core, and their ratios to Al indicate a slight (Pb) and significant (Mn) enrichment with respect to the natural backgrounds (Figure 3-16).

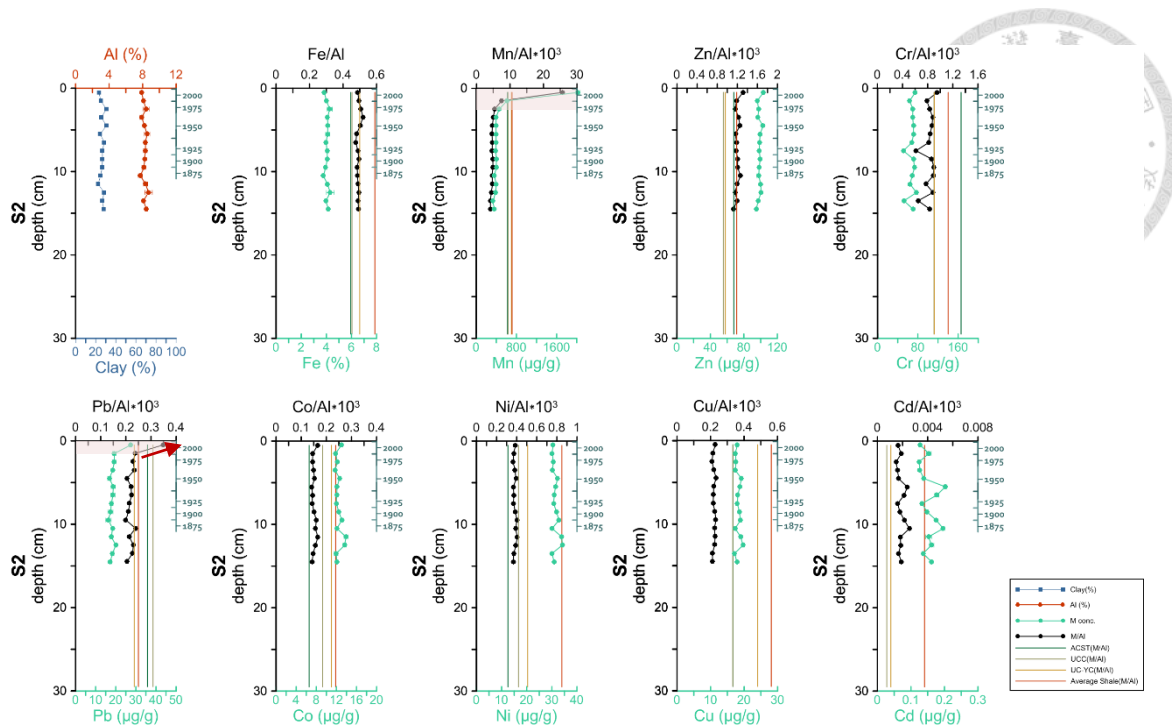


Figure 3-16 Vertical distribution of the metals in core S2. The concentration of Mn and Pb have a sharp increase in the surface layer (red shaded area) and their ratio to Al shows different extent of enrichment with respect to the natural backgrounds (straight lines).

3.3.2 S6 (Gaoping Slope Site)

S6 is also located on the west side of GPSC with a shallower water depth of 618 m, and the concentration of each element at this site are as follow, **Al**: 8.1-9.3%, with a mean of 8.5%; **Fe**: 3.8-4.3%, with a mean of 4.0%; **Mn**: 264-775 µg/g, with a mean of 346 µg/g; **Zn**: 91-103 µg/g, with a mean of 98 µg/g; **Cr**: 66-73 µg/g, with a mean of 69 µg/g; **Pb**: 18-24 µg/g, with a mean of 21 µg/g; **Co**: 11.0-13.6 µg/g, with a mean of 12.1 µg/g; **Ni**: 28.3-31.6 µg/g, with a mean of 29.8 µg/g; **Cu**: 15-18 µg/g, with a mean of 16 µg/g; **Cd**: 0.07-0.14 µg/g, with a mean of 0.11 µg/g (see Appendix).

Most of the trace metals at this site also shows less variations over time, and their ratio to Al all appears around or below the natural backgrounds (Figure 3-17), showing

the natural variability of these elements. The concentration of Zn and Pb have a slight increase over time, and the trend disappeared after normalizing to Al for Zn yet there is still a slight increase in the surface layer for Pb. However, both of their ratio to Al still fall within the range of natural backgrounds (Figure 3-17). Like in core S2, there is also a sharp increase of Mn concentration observed in the surface layer in S6, but their ratio to Al is all below the natural backgrounds (Figure 3-17).

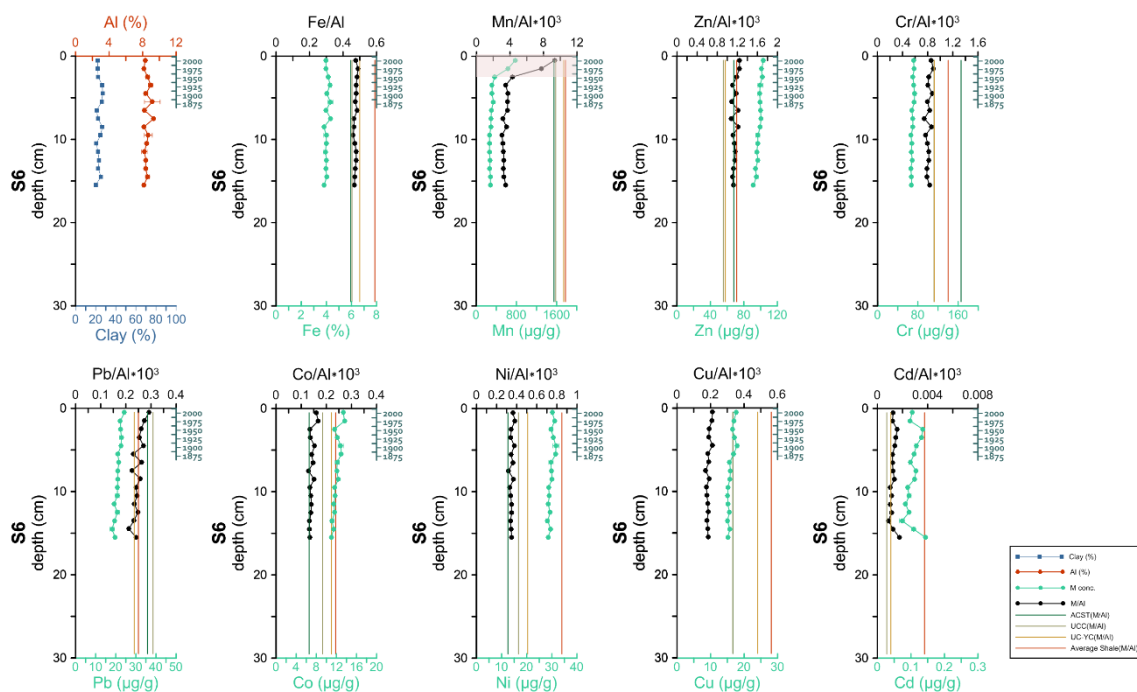
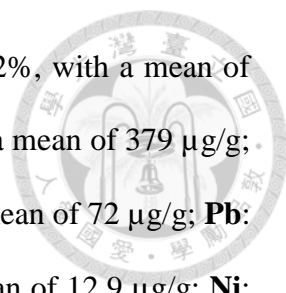


Figure 3-17 Vertical distribution of the metals in core S6. Mn has a sharp increase (red shaded area) at top of this sediment column while its ratio to Al is all below the natural backgrounds.

3.3.3 S1 (Gaoping Slope Site)

S1 is located on the east side of GPSC with a water depth of 822 m, and the



concentration of each element at this site are as follow, **Al**: 7.7-10.2%, with a mean of 8.7%; **Fe**: 4.0-5.2%, with a mean of 4.5%; **Mn**: 311-527 $\mu\text{g/g}$, with a mean of 379 $\mu\text{g/g}$; **Zn**: 95-111 $\mu\text{g/g}$, with a mean of 103 $\mu\text{g/g}$; **Cr**: 59-85 $\mu\text{g/g}$, with a mean of 72 $\mu\text{g/g}$; **Pb**: 18-30 $\mu\text{g/g}$, with a mean of 23 $\mu\text{g/g}$; **Co**: 11.9-15.1 $\mu\text{g/g}$, with a mean of 12.9 $\mu\text{g/g}$; **Ni**: 30.3-36.9 $\mu\text{g/g}$, with a mean of 31.9 $\mu\text{g/g}$; **Cu**: 17-24 $\mu\text{g/g}$, with a mean of 19 $\mu\text{g/g}$; **Cd**: 0.11-0.18 $\mu\text{g/g}$, with a mean of 0.14 $\mu\text{g/g}$ (see Appendix).

Most of the trace metals at this site also oscillates around a constant level (Zn and Pb have a slight increase) over time, and their ratio to Al all appears around or below the natural backgrounds, suggesting a natural variability of these elements (Figure 3-18). In this core, Mn has a small peak in the subsurface layer while the ratio to Al all appears below the natural backgrounds (Figure 3-18). The most obvious feature of this core is Pb has a sharp increase in the surface layer, below which the Pb content seems to fall back to a relatively constant level, and its ratio to Al indicates a slight enrichment in the surface layer (Figure 3-18).

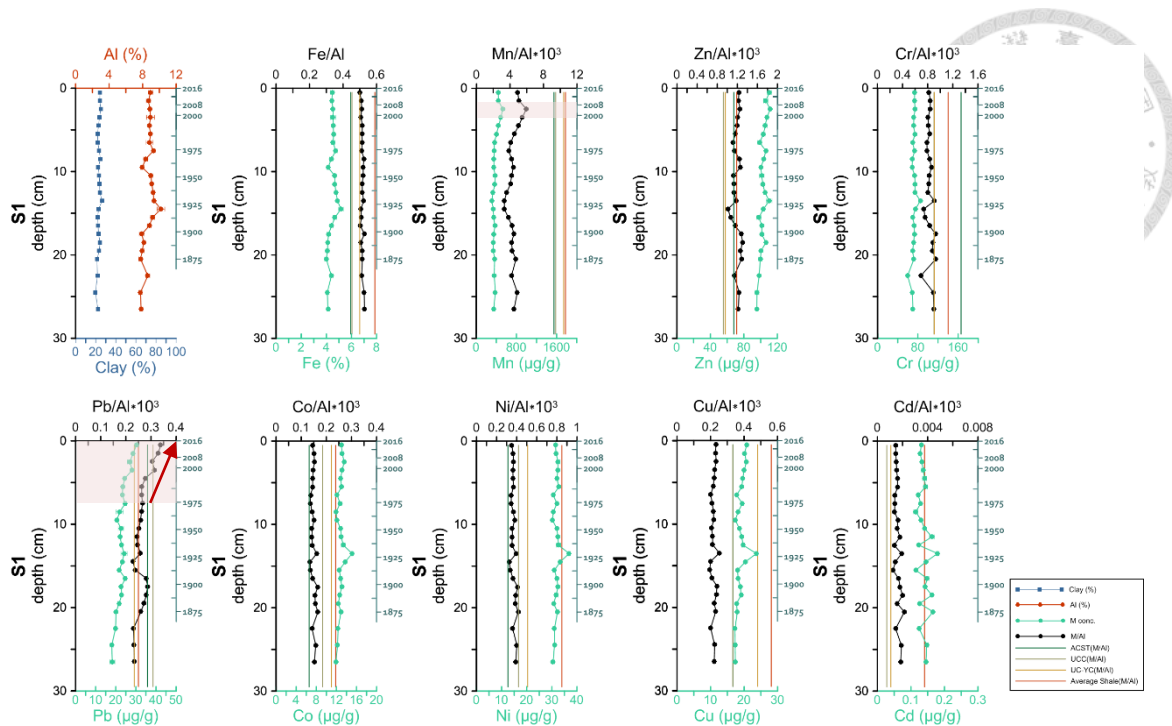
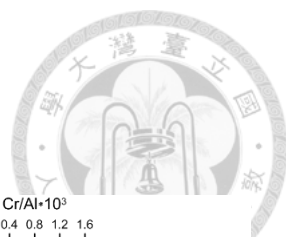


Figure 3-18 Vertical distribution of the metals in core S1. Pb has a sharp increase in the surface layer (red shaded area) and its ratio to Al shows a slight enrichment with respect to the natural backgrounds.

3.3.4 B4G (Gaoping Slope Site)

B4G is also located on the east side of GPSC with a deeper water depth of 863 m, and the concentration of each element at this site are as follow, **Al**: 6.8-7.4%, with a mean of 7.1%; **Fe**: 3.5-3.93%, with a mean of 3.6%; **Mn**: 248-308 µg/g, with a mean of 282 µg/g; **Zn**: 77-87 µg/g, with a mean of 81 µg/g; **Cr**: 62-70 µg/g, with a mean of 65 µg/g; **Pb**: 14-20 µg/g, with a mean of 16 µg/g; **Co**: 9.0-9.9 µg/g, with a mean of 9.5 µg/g; **Ni**: 26.1-29.1 µg/g, with a mean of 27.1 µg/g; **Cu**: 11-14 µg/g, with a mean of 12 µg/g; **Cd**: 0.13-0.26 µg/g, with a mean of 0.20 µg/g (see Appendix).

Most of the trace metals have little variations over time, and their ratio to Al is all around or below the natural backgrounds, showing a dominated natural source at this site (Figure 3-19). Pb and Cd seem to have a slight increase over time, but their ratios



to Al are all around or below the natural backgrounds (Figure 3-19).

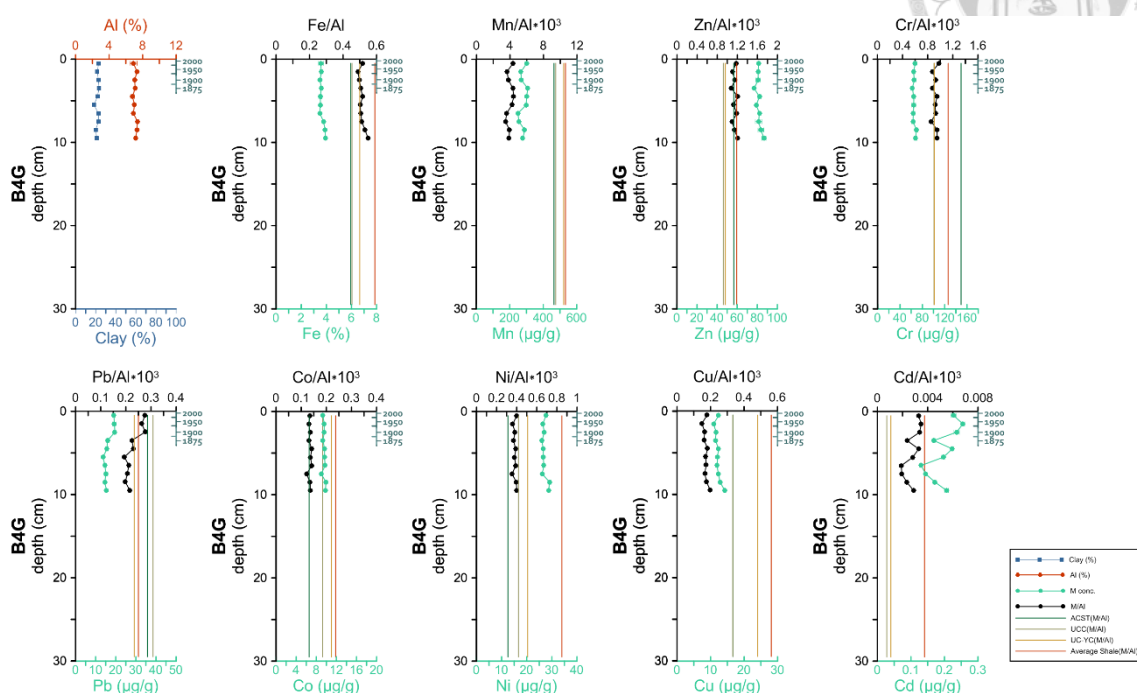


Figure 3-19 Vertical distribution of the metals in core B4G.

3.3.5 PL02 (Penghu Submarine Canyon Site)

PL02 is sampled on the Palm Ridge at head of the Penghu Submarine Canyon with a water depth of 931 m, and the concentration of each element at this site are as follow, **Al**: 4.7-7.4%, with a mean of 6.2%; **Fe**: 3.2-3.8%, with a mean of 3.5%; **Mn**: 250-595 $\mu\text{g/g}$, with a mean of 310 $\mu\text{g/g}$; **Zn**: 77-85 $\mu\text{g/g}$, with a mean of 81 $\mu\text{g/g}$; **Cr**: 57-66 $\mu\text{g/g}$, with a mean of 63 $\mu\text{g/g}$; **Pb**: 12-17 $\mu\text{g/g}$, with a mean of 14 $\mu\text{g/g}$; **Co**: 9.8-11.7 $\mu\text{g/g}$, with a mean of 11.0 $\mu\text{g/g}$; **Ni**: 25.0-29.2 $\mu\text{g/g}$, with a mean of 27.4 $\mu\text{g/g}$; **Cu**: 11-14 $\mu\text{g/g}$, with a mean of 13 $\mu\text{g/g}$; **Cd**: 0.10-0.15 $\mu\text{g/g}$, with a mean of 0.13 $\mu\text{g/g}$ (see Appendix).

At the Penghu Submarine Canyon site, except that Mn has a sharp increase in the surface layer, other metals show a nearly constant concentration over time (Figure 3-20). After normalizing to Al, most of the metal/Al ratios show a small peak in the subsurface

and bottom layer. However, since their concentrations stay nearly constant over time, these peaks are resulted from the variation of Al concentration along the depth (can also see these small peak layers is characterized with a relatively low concentration of Al, Figure 3-20), and most of the metals to Al ratio still appear around the natural backgrounds, showing their primary sources from crustal materials. Zn/Al ratio is slightly higher than the natural backgrounds in this core.

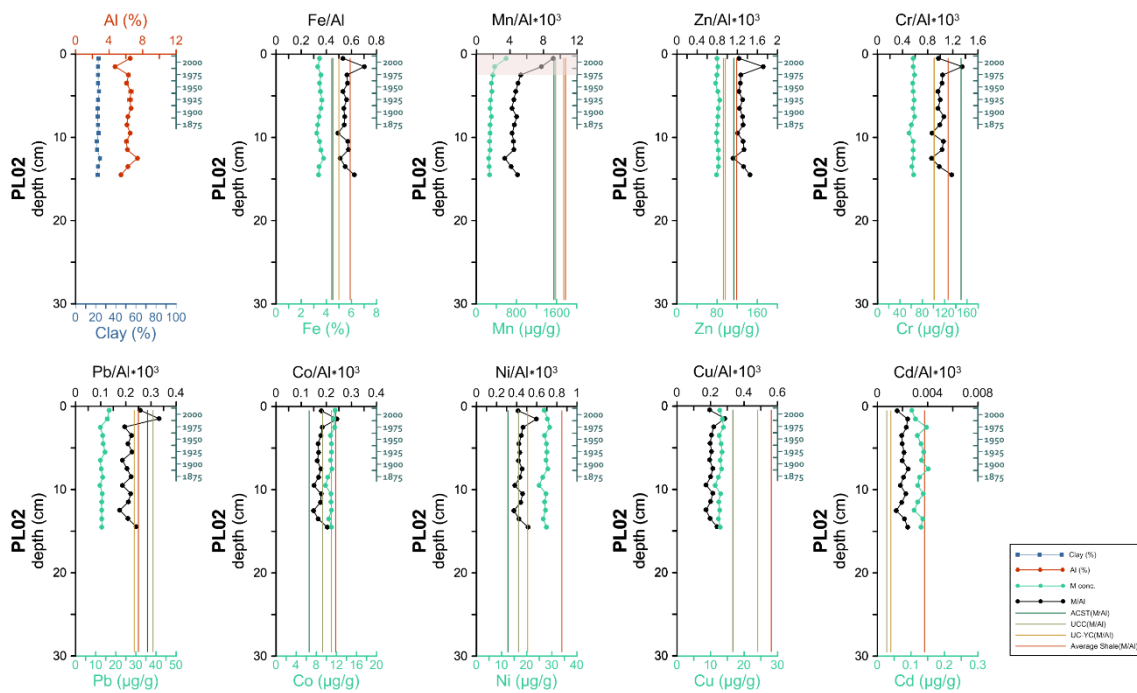
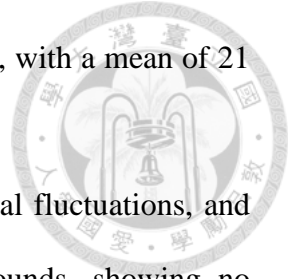


Figure 3-20 Vertical distribution of the metals in core PL02.

3.3.6 MT6 (Deep Sea Site)

MT6 is a deep sea site at lower reach of GPSC with a water depth of 3078 m, and the concentration of each element at this site are as follow, **Al**: 7.2-9.6%, with a mean of 8.6%; **Fe**: 3.6-4.8%, with a mean of 4.4%; **Mn**: 393-1160 µg/g, with a mean of 516 µg/g; **Zn**: 86-113 µg/g, with a mean of 100 µg/g; **Cr**: 62-76 µg/g, with a mean of 70 µg/g; **Pb**: 9-23 µg/g, with a mean of 18 µg/g; **Co**: 11.0-13.1 µg/g, with a mean of 12.2

$\mu\text{g/g}$; **Ni**: 28.2-33.9 $\mu\text{g/g}$, with a mean of 31.2 $\mu\text{g/g}$; **Cu**: 16-24 $\mu\text{g/g}$, with a mean of 21 $\mu\text{g/g}$; **Cd**: 0.13-0.25 $\mu\text{g/g}$, with a mean of 0.19 $\mu\text{g/g}$ (see Appendix).



Most of the trace metals at this site also possess small temporal fluctuations, and their ratio to Al all drops around or below the natural backgrounds, showing no interference from anthropogenic sources (Figure 3-21). At top of this sediment column, it is also found a sharp increase of Mn, and its ratio to Al shows its enrichment with respect to the natural backgrounds (Figure 3-21). Due to the dilution of coarser detrital materials, lowered concentration of most trace metals are found in the event layers (yellow shaded area).

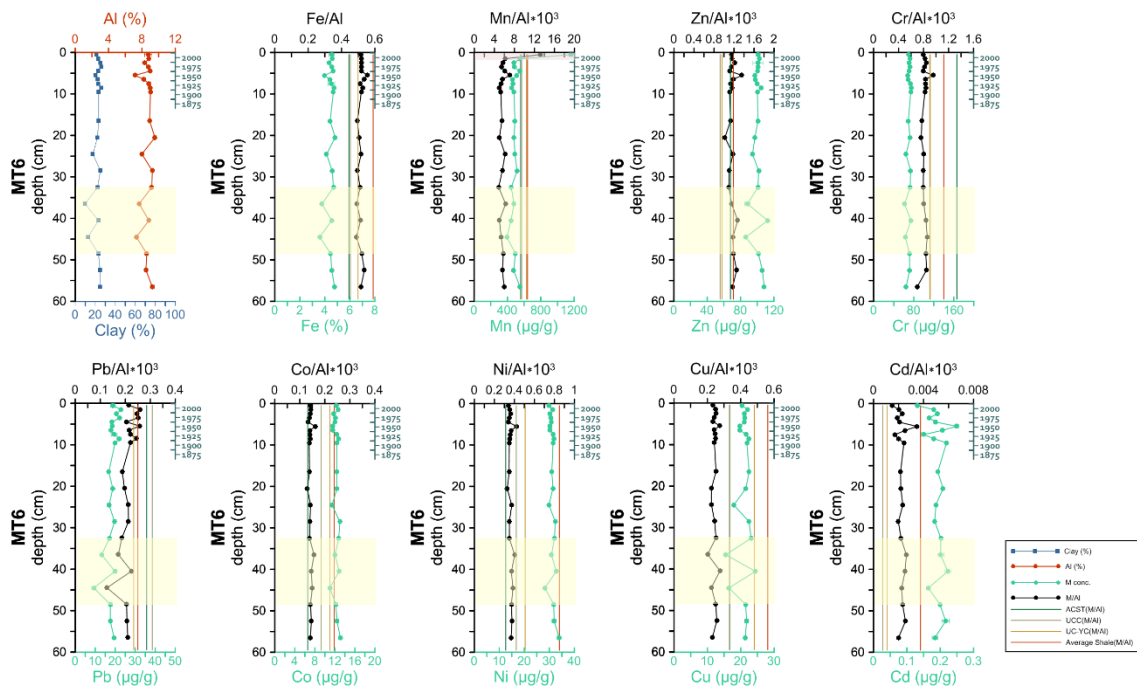
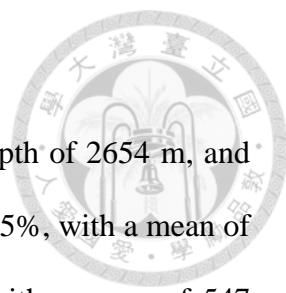


Figure 3-21 Vertical distribution of the metals in core MT6. Mn has a sharp increase at top of this sediment column and its ratio to Al shows its enrichment with respect to the natural backgrounds. Lowered concentration of most trace metals is found in the event layer (yellow shaded area).

3.3.7 MT7 (Deep Sea Site)



MT7 is a deep sea site on the Tsan-Yao Ridge with a water depth of 2654 m, and the concentration of each element at this site are as follow, **Al**: 7.5-9.5%, with a mean of 8.5%; **Fe**: 3.6-4.8%, with a mean of 4.1%; **Mn**: 355-1663 $\mu\text{g/g}$, with a mean of 547 $\mu\text{g/g}$; **Zn**: 93-106 $\mu\text{g/g}$, with a mean of 100 $\mu\text{g/g}$; **Cr**: 59-77 $\mu\text{g/g}$, with a mean of 70 $\mu\text{g/g}$; **Pb**: 16-23 $\mu\text{g/g}$, with a mean of 19 $\mu\text{g/g}$; **Co**: 11.5-14.7 $\mu\text{g/g}$, with a mean of 12.7 $\mu\text{g/g}$; **Ni**: 29.3-33.8 $\mu\text{g/g}$, with a mean of 31.6 $\mu\text{g/g}$; **Cu**: 18-28 $\mu\text{g/g}$, with a mean of 23 $\mu\text{g/g}$; **Cd**: 0.09-0.32 $\mu\text{g/g}$, with a mean of 0.15 $\mu\text{g/g}$ (see Appendix).

Most of the trace metals at this site also presents little variations over time, and their ratio to Al also falls within or below the natural backgrounds (Figure 3-22). At this site, it can be noticed that the high content of Mn, unlike other cores, all appearing in the surface layer, it appears right below the event layer, and their ratio to Al also indicates their enrichments with respect to the natural backgrounds (Figure 3-22). In contrast, Cd shows increased and frequent changes within the event layer.

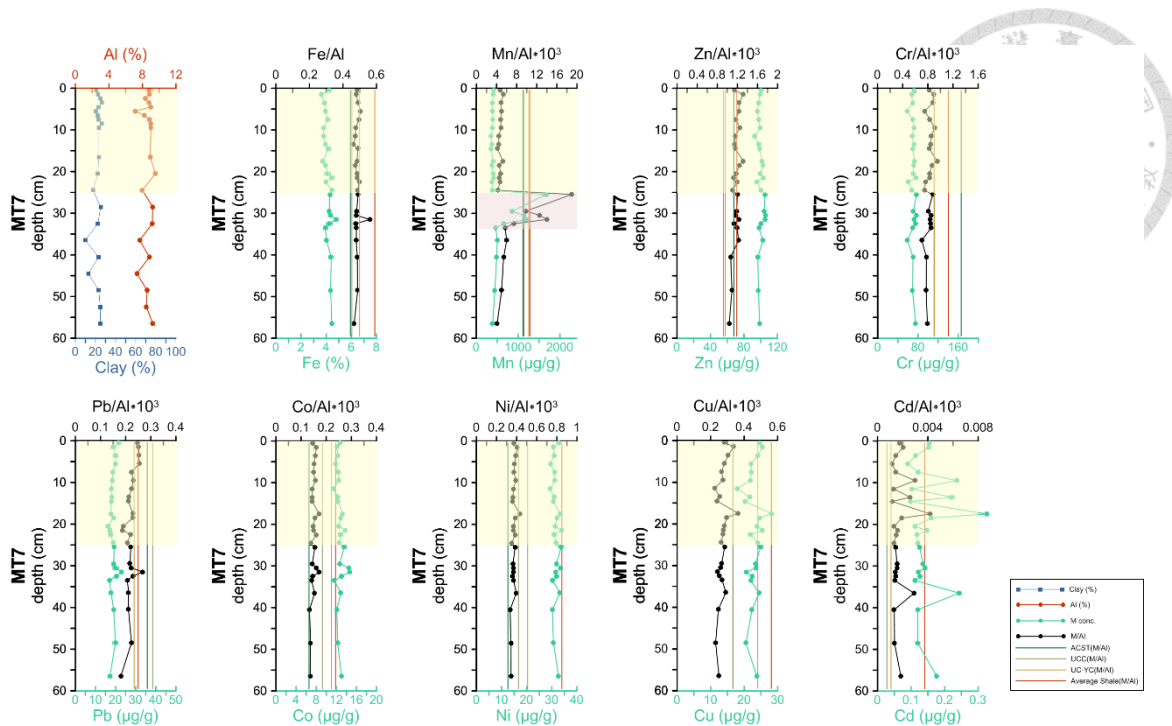
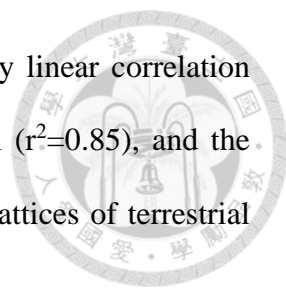


Figure 3-22 Vertical distribution of the metals in core MT7. The yellow shaded area is the event layer. Mn is enriched right below the event layer and Cd followed more variations in the event layer.

3.4 Source of the Elements

Figure 3-23 & Figure 3-24 show elements versus Al plots in all different sediment cores from this study with respect to the reference backgrounds (UCC, ACST, UC-YC and Average Shale). Owing to Al is the major component of Aluminosilicates which is considered as a good proxy for natural background, the correlation between elements and Al can also reveal the source of the elements. Moreover, since the slope of connection line between the origin and the reference background (black signs) is presented as M/Al on the plot, the data point above the reference backgrounds can indicate the enrichment of the metal (M) with respect to the background materials. The data falling out of linear distribution on M/Al plot or appearing above the reference materials can indicate a non-crustal source.



The Fe/Al , Mg/Al, and K/Al plots (Figure 3-23) show highly linear correlation between Fe and Al ($r^2=0.80$), Mg and Al ($r^2=0.75$), and K and Al ($r^2=0.85$), and the significant correlations can reveal the association of Fe, Mg, K in lattices of terrestrial Aluminosilicate minerals in the study area.

In Ti/Al plot (Figure 3-23), the data distributed around the reference line has a more dispersed distribution ($r^2=0.37$) than Mg, Fe and K, which can be caused by the gravity fractionation of elements during sediment transport.

In Mn/Al plot (Figure 3-23), most of the data points lie under the reference materials, and without a good correlation to the Al concentration ($r^2=0.05$). Several data points show the distinct enrichments of Mn in the core S2, MT6 and MT7 and the enriched level appear to display in the sequence of S2 > MT7 > MT6. Under the reference materials, the data points show a relatively horizontal distribution which indicates most of the non-enriched layer show a consistent concentration of Mn and the level differs between different sites.

In Zn/Al plot (Figure 3-23), it shows that the slight enrichment of Zn seems to conformably exist in all cores with respect to the reference backgrounds, but they are well-correlated with the Al content ($r^2=0.70$), revealing its association with aluminosilicate of continental origin.

In Cr/Al, Co/Al and Ni/Al plots (Figure 3-24), all cores show a distribution close to the reference materials, indicating these metals are mainly sourced from a natural source.

In Pb/Al plot (Figure 3-24), the Pb content in each core shows a nearly background value (all data points distributed around the reference backgrounds), while a group of data points from the sediment core of S1 and S2 have deviated from the linear distribution, indicating an non-lithogenic source of Pb in the study area.

In Cu/Al plot (Figure 3-24), nearly all the data points are below each individual reference background, revealing the depleted condition of Cu in all these cores.

In Cd/Al plot (Figure 3-24), there shows a very dispersed distribution with no correlation with Al ($r^2=0.000003$), and most of them fall within the range of reference backgrounds.

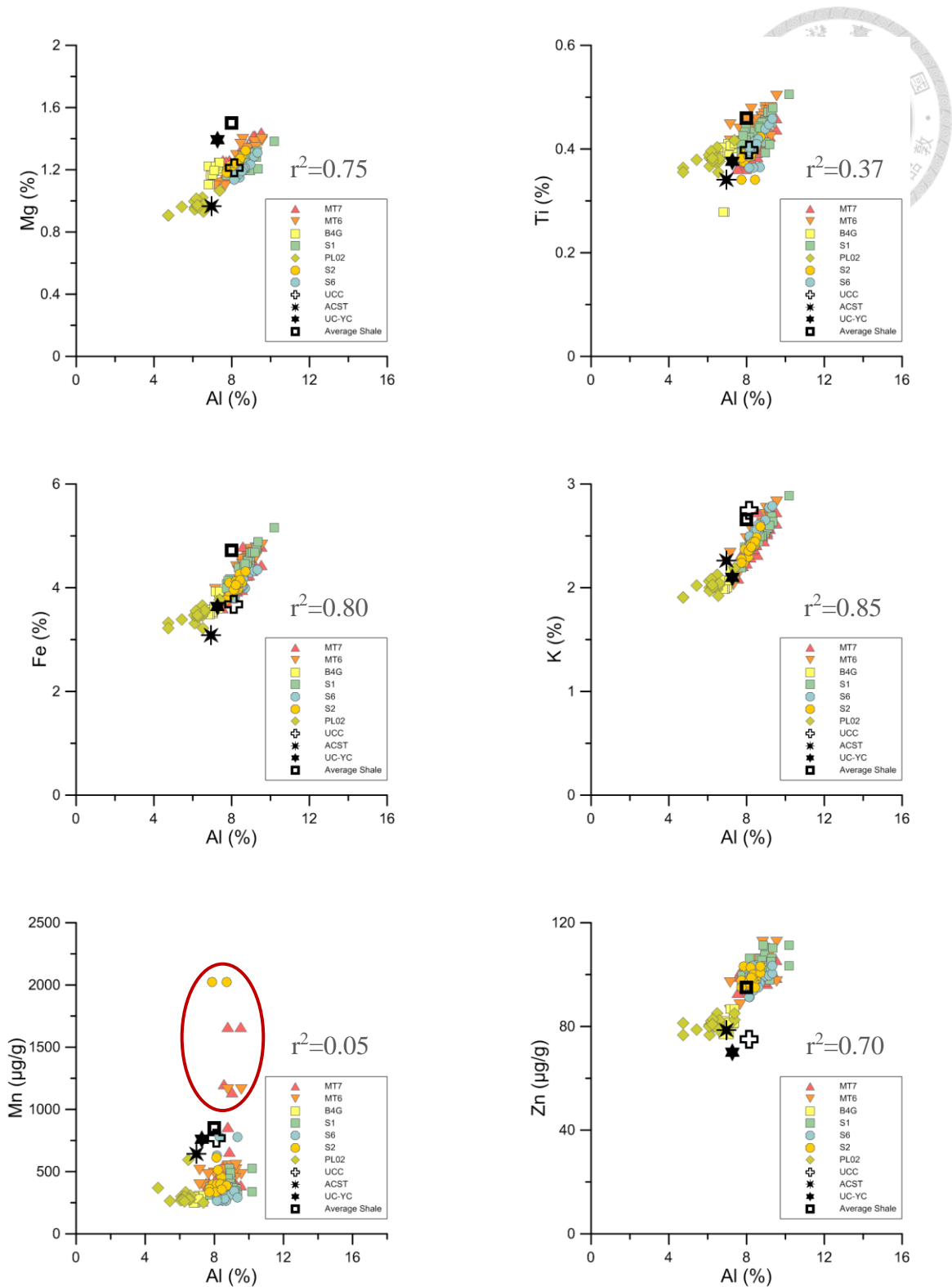


Figure 3-23 Scatter plot between concentrations of metals (Mg, Ti, Fe, K, Mn, Zn) and Al for each sample in different sediment cores analyzed in this study. The R-square on the plot is the result of linear regression between metals and Al of all data points in this study.

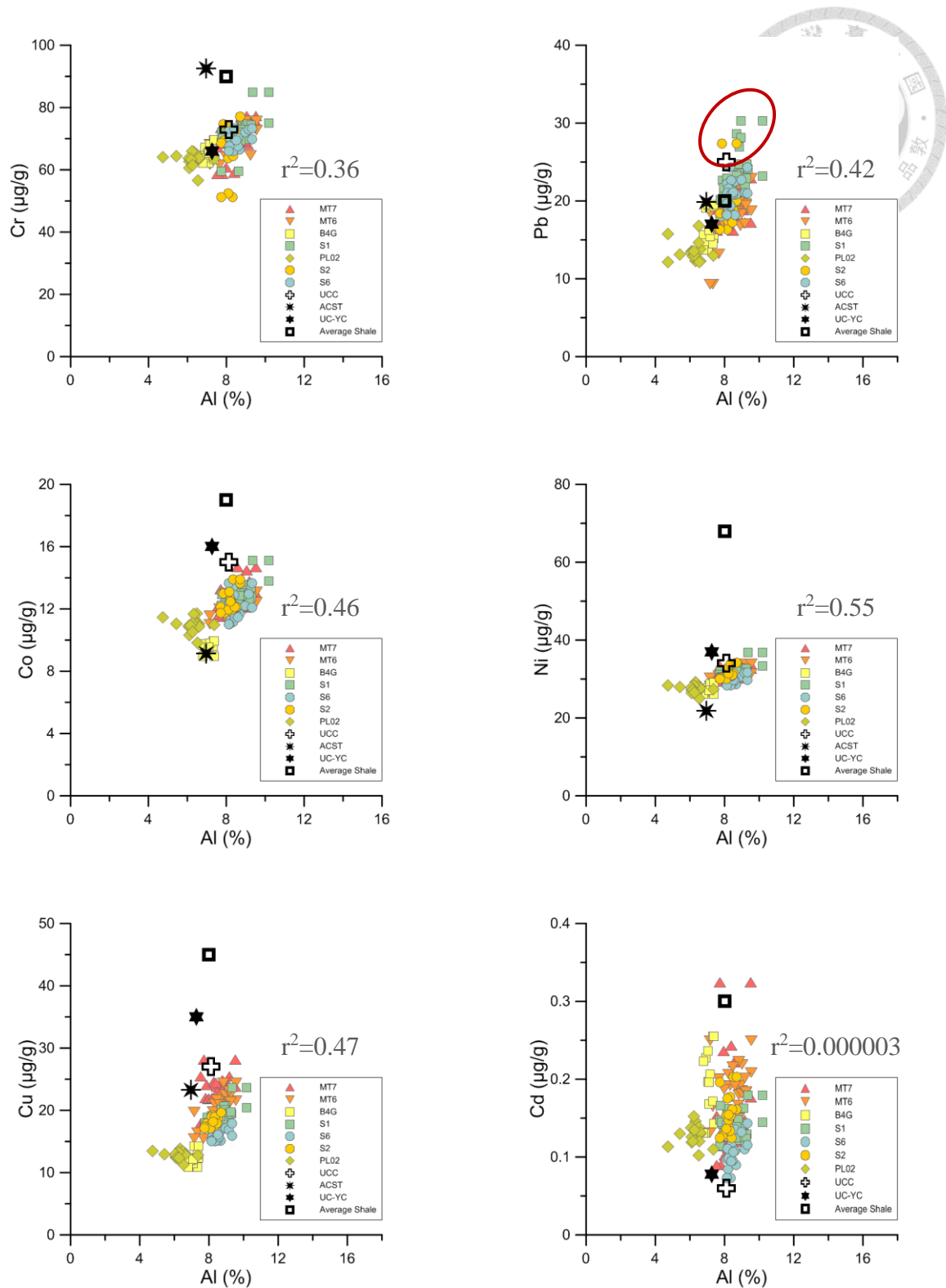


Figure 3-24 Scatter plot between concentrations of metals (Cr, Pb, Co, Ni, Cu, Cd) and Al for each sample in different sediment cores analyzed in this study. The R-square on the plot is the result of linear regression between metals and Al of all data points in this study.

3.5 Enrichment of the Trace Metals

3.5.1 Mn

The concentrations of Mn in each sediment core are in the ranges as follow: **PL02**: 250-595 $\mu\text{g/g}$, with a mean of 310 $\mu\text{g/g}$; **S2**: 335-2022 $\mu\text{g/g}$, with a mean of 513 $\mu\text{g/g}$; **S6**: 264-775 $\mu\text{g/g}$, with a mean of 346 $\mu\text{g/g}$; **S1**: 311-527 $\mu\text{g/g}$, with a mean of 379 $\mu\text{g/g}$; **B4G**: 248-308 $\mu\text{g/g}$, with a mean of 282 $\mu\text{g/g}$; **MT6**: 393-1160 $\mu\text{g/g}$, with a mean of 516 $\mu\text{g/g}$; **MT7**: 355-1663 $\mu\text{g/g}$, with a mean of 547 $\mu\text{g/g}$ (see Appendix).

Among the elements measured in this study, most of them did not show many significant fluctuations in the concentration profiles. However, among the analyzed sediments cores in this study, most of them (except for S1 and B4G) were found with a relatively high concentration of Mn in the surface layers with different extents of enrichment (Figure 3-25). Compared to the natural backgrounds, Mn is enriched in S2 and MT6 surface sediments, while MT7 shows a very distinct pattern associated with the event layer (Figure 3-25). In core MT7, the distinct high content of Mn appears immediately under the event layer and followed by some variations in the enriched layers. The thickness of the high Mn content layer in each core is as follow: PL02, MT6 and S2 (~1.5 cm) < S6 (~2.5 cm) < MT7 (~9 cm), yet the enrichment layer is absent in core S1 and B4G, both of which are on the eastern side of the GPSC (Figure 3-26). Under the high Mn content layer, the concentration of Mn decreases dramatically to a constant level, the mean concentration of Mn under high content layer in each core are as follow: B4G (282 $\mu\text{g/g}$) < PL02 (283 $\mu\text{g/g}$) < S6 (290 $\mu\text{g/g}$) < S1 (379 $\mu\text{g/g}$) < S2 (389 $\mu\text{g/g}$) < MT7 (407 $\mu\text{g/g}$) < MT6 (481 $\mu\text{g/g}$), and it seems to be related to the water depth of the core collecting sites, where S6, PL02, B4G, S1 are at water depth of 618-822 m, S2 is at water depth of 1205 m, and MT6 and MT7 is in the water depth



over 2600 m.

Although the enrichment of Mn in surface sediments are frequently caused by the early diagenesis process, there is no clear covariation between Mn and Fe in our analyzed cores (Figure 3-26). In addition, the Fe/Al ratios in the analyzed cores are close to the background level (can be seen in former section, Figure 3-11), indicating no authigenic Fe was formed in these cores and the enrichment of Mn may not be caused by early diagenesis process in the sediments. However, it can be noticed that the significant enrichment of Mn only exists in the cores collected from the western side of GPSC in this study (also mentioned by 林, 2006) where is also the slag dumping site of China Steel Corporation (CSC) off Kaohsiung Harbor. As Mn is an important component of steel, with a composition of Fe: 80–98%, Mn: 0.2–16%, C: 0.03–1.25%, P: maximum 0.05%, and S: maximum 0.05% (Chen & Selvaraj, 2008), the high Mn content might also be resulted from the anthropogenic source. According to previous studies (Chen & Selvaraj, 2008), the dumping sites were deployed during 1984-1995 (old dumping site: 1984-1988; new dumping site: 1988-1995), and the onset of sharp increase of Mn observed in Gaoping Slope can neither correspond to the slag dumping period nor a consistent time (red dashed line in Figure 3-25), saying there is neither no proof for the hypothesis of anthropogenic source of Mn. Consequently, lack evidence is provided to explain the enrichment of Mn observed in this study, whether they were derived from a pollution source, diagenesis process or even the interplay of both sources.

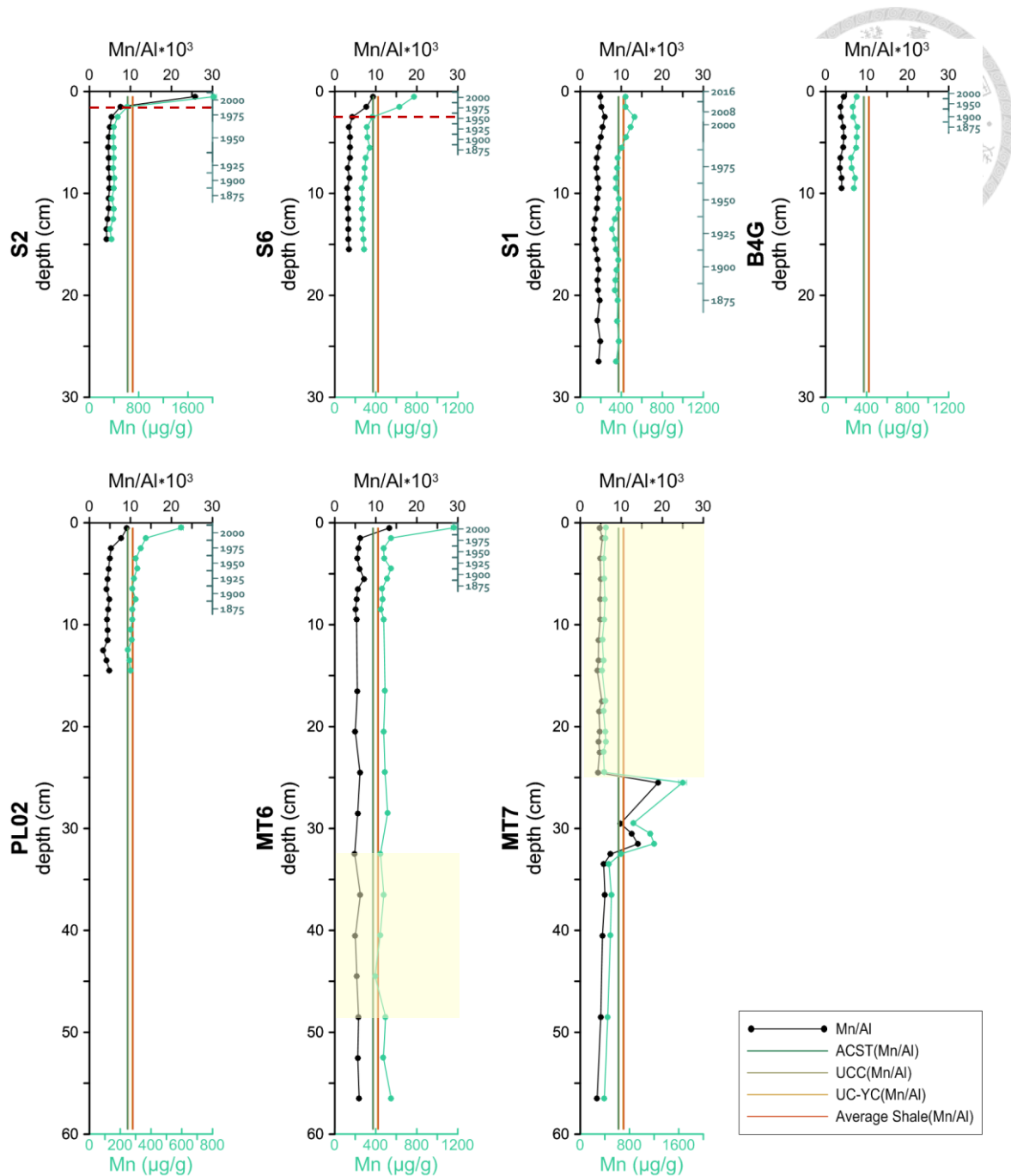


Figure 3-25 Vertical distributions of Mn and Mn/Al ratio with comparison to the natural backgrounds in each sediment core analyzed in this study. The high manganese content appears in the surface layer of each sediment core except for S1 and B4G, and the relatively high in MT7 happened at depth of 25-33 cm that is directly below the event layer (yellow shaded area). Enrichments of Mn are found at top of the sediment cores of S2 and MT6, and in the strata immediately below the event layer in MT7.

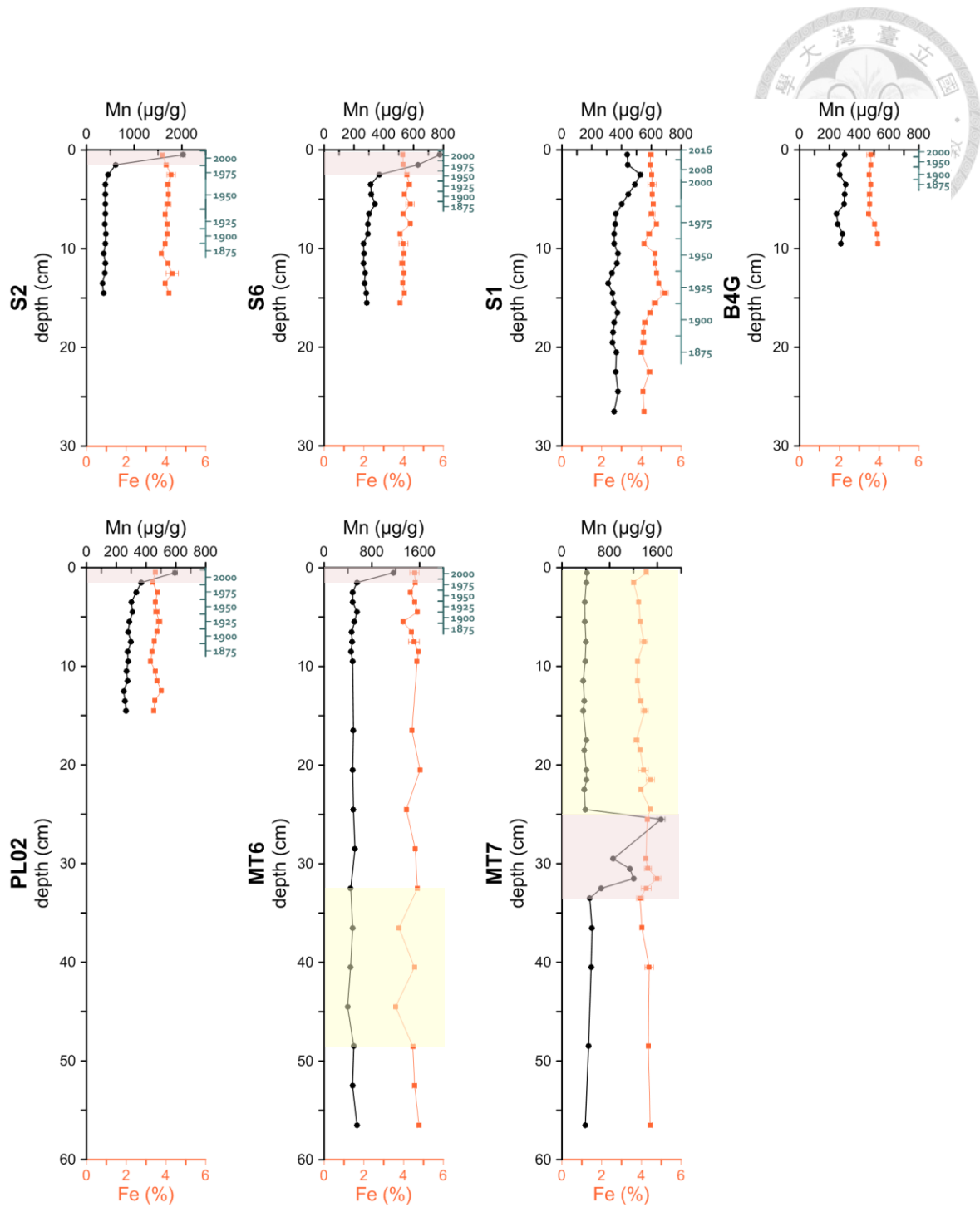


Figure 3-26 Vertical distributions of Mn and Fe in each sediment core analyzed in this study. The high Mn content layer is indicated with red shaded area. Most of them appear at top of the sediment columns while the one in MT7 appears directly under the event layer.

3.5.2 Pb

The concentration of Pb in each sediment core are in the ranges as follow: **PL02**: 12.2-16.8 $\mu\text{g/g}$, with a mean of 13.5 $\mu\text{g/g}$; **S2**: 16-27.4 $\mu\text{g/g}$, with a mean of 19 $\mu\text{g/g}$; **S6**: 18-24.3 $\mu\text{g/g}$, with a mean of 21 $\mu\text{g/g}$; **S1**: 18.0-30.3 $\mu\text{g/g}$, with a mean of 23 $\mu\text{g/g}$; **B4G**: 13.7-19.5 $\mu\text{g/g}$, with a mean of 16.3 $\mu\text{g/g}$; **MT6**: 9-22.9 $\mu\text{g/g}$, with a mean of 18 $\mu\text{g/g}$; **MT7**: 16-22.9 $\mu\text{g/g}$, with a mean of 19 $\mu\text{g/g}$ (see Appendix).

Figure 3-27 shows the vertical distributions of Pb in different cores. At the Gaoping Slope sites (S2, S6, S1 and B4G), all of the Pb concentration profiles show a conformable increasing trend over time. In core S2, S6, S1 and PL02, a sharp increase in Pb content within the surface layer is observed. In core S1, the Pb concentration even increases to nearly twice of the bottom concentration (18 $\mu\text{g/g}$ to 30 $\mu\text{g/g}$). After normalizing to Al, the sharp increase still exists within the surface layer in core S2, S6 and S1, and below the sharp increase they all fall back to a relatively consistent background level, indicating the increases observed at the sites can be resulted from an anthropogenic source. Among the sharp increase of Pb concentration sites observed on the Gaoping Slope, S2 and S1 show higher Pb/Al ratios than all the natural backgrounds, showing a higher degree of Pb enrichment than other sites. Moreover, the onset of these increasing Pb can correspond to a consistent year of 1970s (Figure 3-27), which confirms to the rapid industrial development period in Taiwan.

If compared to the studied core (KP Core, Hung & Hsu, 2004) also with pollution record of Pb at the head of GPSC, the onset of increasing Pb observed in Gaoping Slope cores is consistent with the time observed in the coastal area (Figure 3-28). Furthermore, if compare the temporal distribution of Pb between the Gaoping Slope cores and KP Core at the head of GPSC in a same period of time (yellow square in Figure 3-28), we can even observe the identical trend between S1 and KP Core (Figure 3-28). Although

the pollution signal is much weaker in the Gaoping Slope (Pb/Al is only slightly higher than the natural backgrounds), the accumulation of Pb in Gaoping Slope can still clearly illustrate the temporal input trend of Pb in the nearshore region. However, there is no obvious increasing trend of Pb concentration observed in the deep sea sites, and their Pb/Al ratios all appear around the natural backgrounds (Figure 3-27). Our results reveal the pollution history of human activities can still be recorded in the Gaoping Slope sediments, but no pollution signal of Pb is found in the further seaward deep sea sites.

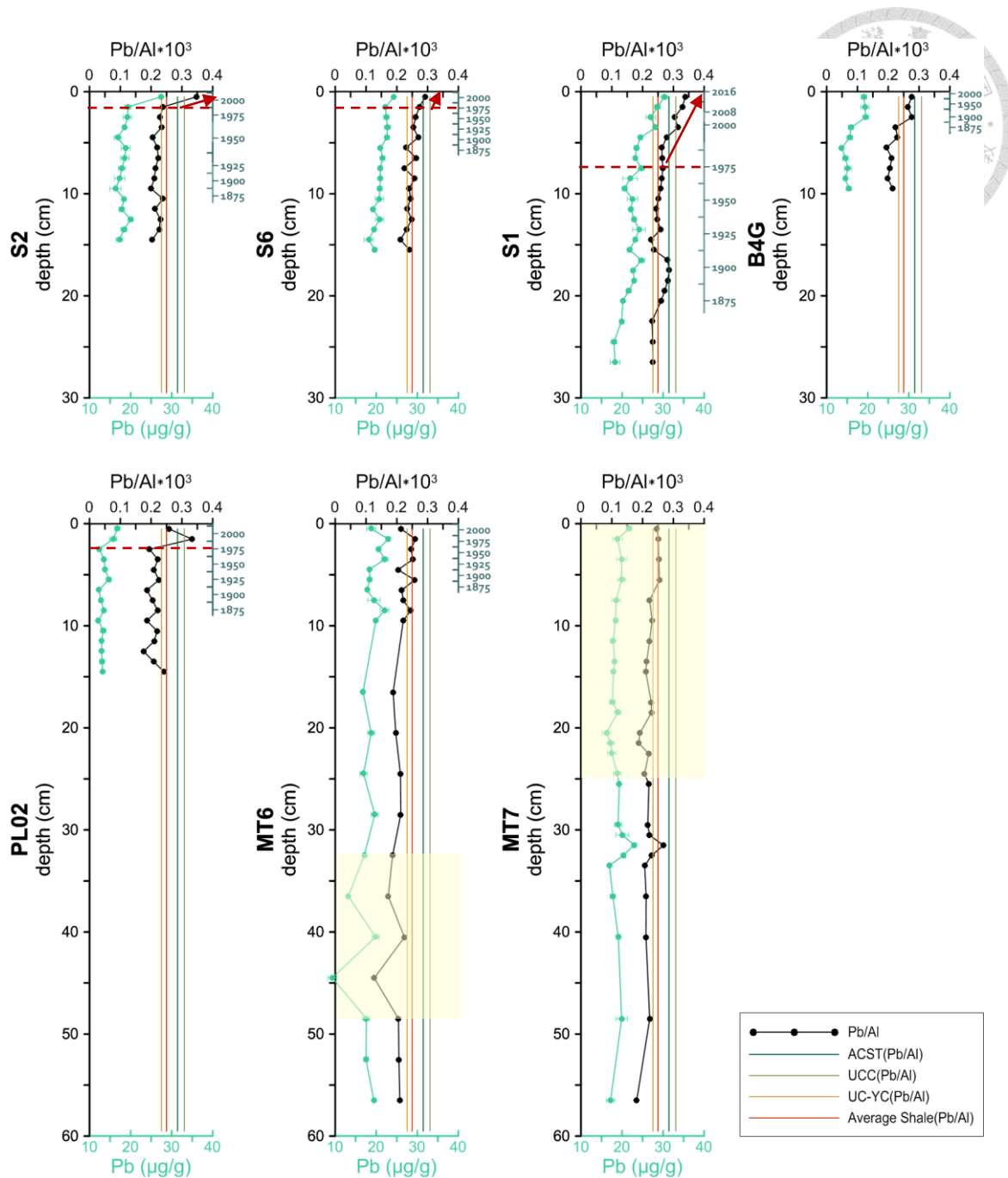


Figure 3-27 Vertical distributions of Pb and Pb/Al ratio with comparison to the natural backgrounds in each sediment core analyzed in this study. The profiles of the Gaoping Slope sites (S2, S6, S1 and B4G) show a conformable increasing trend of Pb concentration over time. The red dashed line shows the onset of the sharp increasing trend in Pb concentrations observed in core S2, S6 and S1 and all the onsets can correspond to a consistent year of 1970s. Slight enrichment of Pb is found within the surface layer in core S2 and S1 with respect to the reference backgrounds.

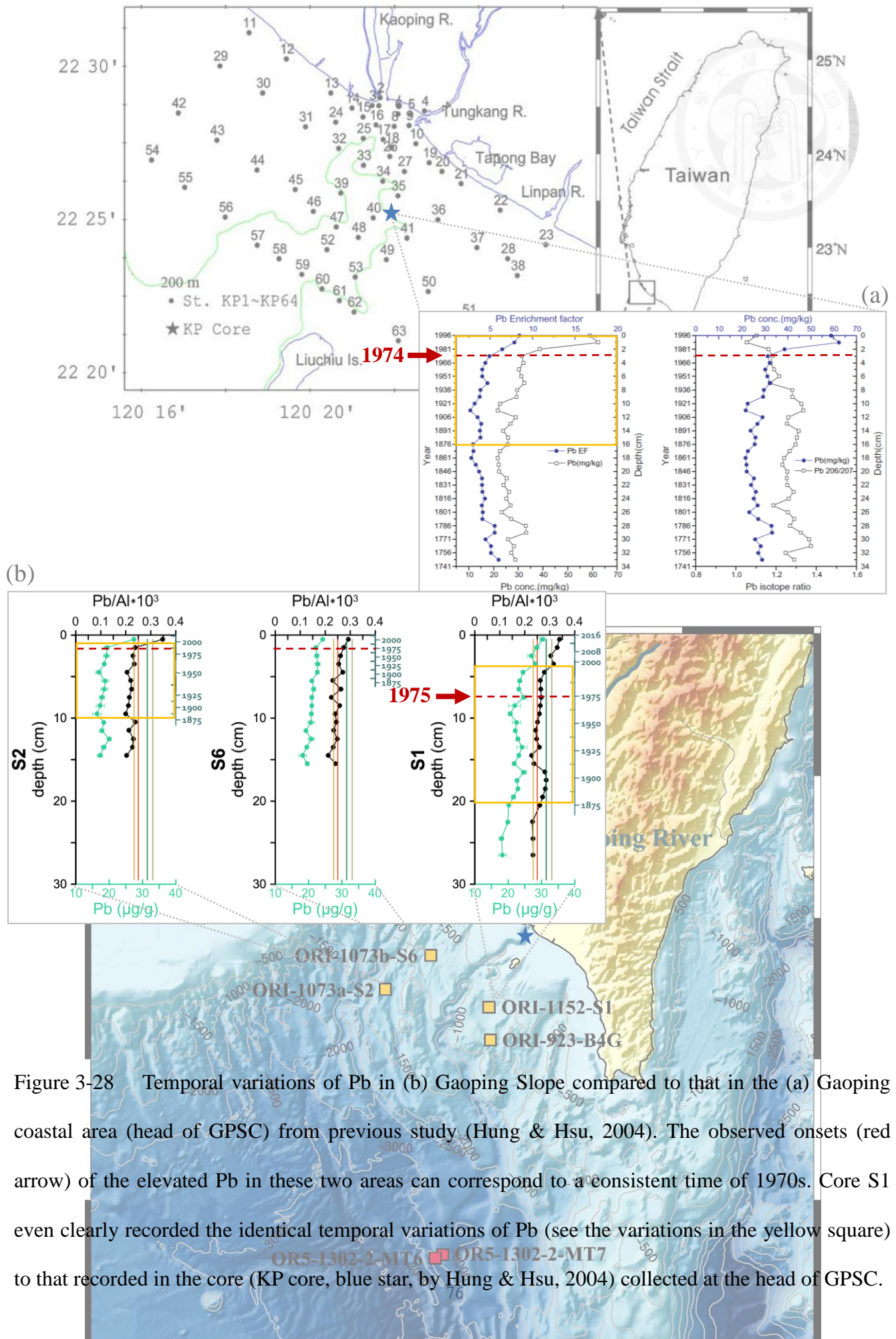


Figure 3-28 Temporal variations of Pb in (b) Gaoping Slope compared to that in the (a) Gaoping coastal area (head of GPSC) from previous study (Hung & Hsu, 2004). The observed onsets (red arrow) of the elevated Pb in these two areas can correspond to a consistent time of 1970s. Core S1 even clearly recorded the identical temporal variations of Pb (see the variations in the yellow square) to that recorded in the core (KP core, blue star, by Hung & Hsu, 2004) collected at the head of GPSC.

3.6 Cumulative Mass of the Trace Metals

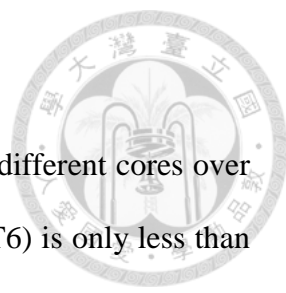


Figure 3-29 shows the cumulative mass of the metals between different cores over the last 150 years. The amount accumulated at the deep sea site (MT6) is only less than that accumulated in core S1, having comparable amount as other Gaoping Slope sites (S2, S6) and even greater amount than that in core B4G, implying a considerable amount of metals will be transported to and accumulated in the deep sea basin (Figure 3-29). In the past few decades, sediment cores collected off southwestern Taiwan are found to have recorded the natural hazards like typhoons and earthquakes. In the sediment cores analyzed in this study, events are found recorded in the sediment cores of B4G, MT6 and MT7 based on the ^{210}Pb and grain size data from previous studies (鄭, 2012; 蔡, 2014). Since the duration time of an event won't be longer than one year, we divided the cumulative mass over the last 150 years as a year average to be compared to the quantity contributed from an event, and the results showed that the absolute amount (cumulative mass) of the trace metals brought from an event over a short time period (less than one year) can be much greater than those delivered from a long-term (year average) steady sedimentation condition (Table 3-4).

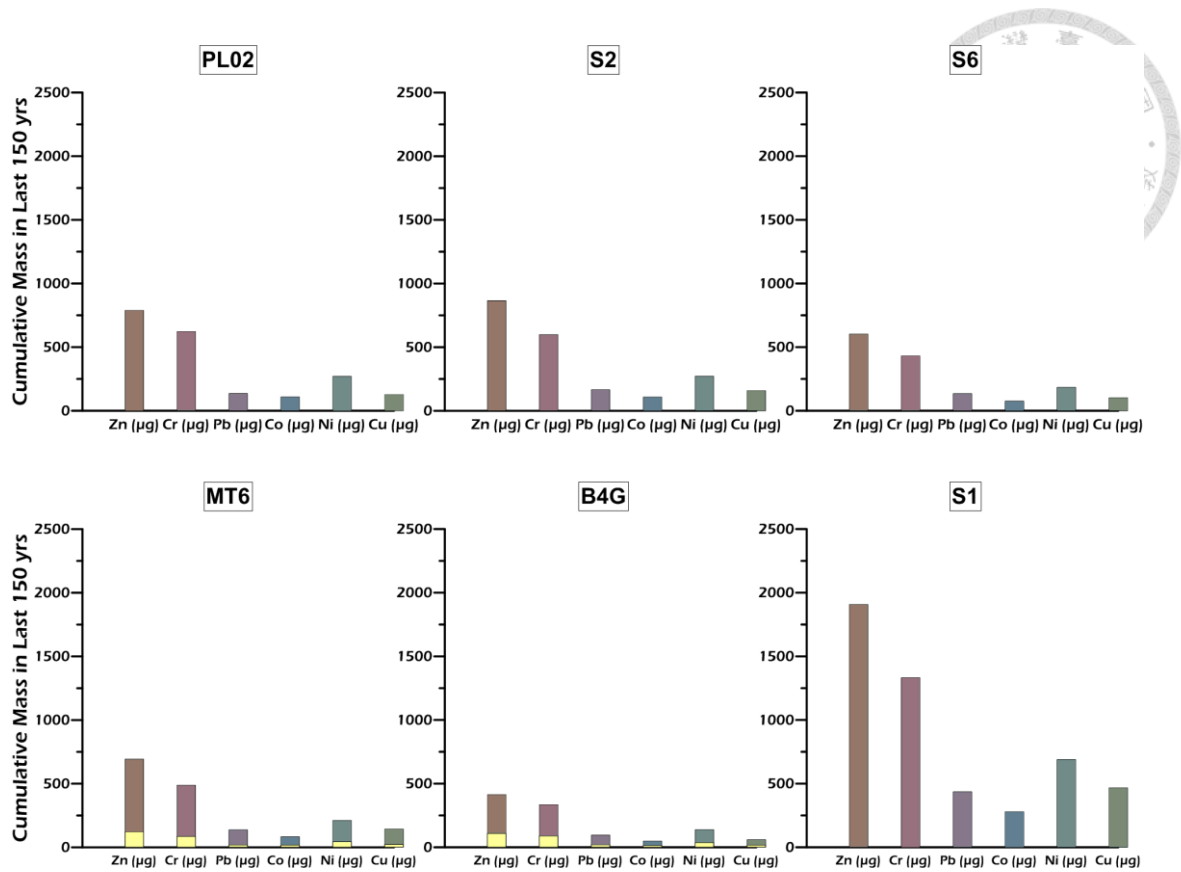


Figure 3-29 Cumulative mass of the metals in the last 150 years in core PL02, S2, S6, MT6, B4G and S1. The lower yellow bars in core MT6 and B4G show the amount contributed from the event layer (B4G: 4-5 cm; MT6: 36-37 cm) compared to the accumulation over the last 150 years (the whole bar). The cumulative mass of the metals in the deep sea site (MT6) is comparable to the amount accumulated in the Gaoping Slope sites (S2 and S6), and even greater than that in core B4G.



Table 3-4

Comparison in cumulative mass of the trace metals contributed from non-event and event period in core MT6 and B4G.

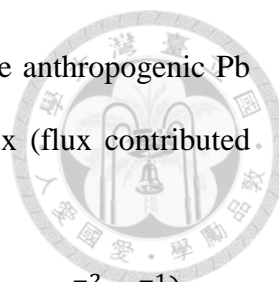
	MT6		B4G	
	Year Average	Event Layer (36-37cm)	Year Average	Event Layer (5-6cm)
Zn (μg)	4.6201	120.4124	2.7563	107.9967
Cr (μg)	3.2517	84.1189	2.2310	88.2211
Pb (μg)	0.9157	18.0184	0.6335	18.6735
Co (μg)	0.5541	16.3992	0.3255	13.1511
Ni (μg)	1.4080	42.0956	0.9226	36.3937
Cu (μg)	0.9574	21.1449	0.3998	16.4558
Cd (μg)	0.0087	0.2743	0.0076	0.2693

The year average is derived from the cumulative mass over the last 150 years.

3.7 Lead Pollution in Aquatic Sediments in a global Comparison

Through geochemical and geochronological investigations on the aquatic sediment archives (estuary, coastal or offshore sediments), the sedimentary records can potentially reveal a pollution history and the source and fate of the contaminants. In this case, we would like to know more knowledge about the Pb pollution recorded in our analyzed cores. Our ^{210}Pb dating and geochemical analyses render us the sedimentation rate (Material Accumulation Rate, MAR) of each sediment cores and the Pb concentration of certain depth, thus we can calculate the annual flux of Pb as follow:

$$\text{Annual Pb Flux } (\mu\text{g cm}^{-2}\text{yr}^{-1}) = \text{MAR } (\text{g cm}^{-2}\text{yr}^{-1}) \times \text{Pb conc. } (\mu\text{g g}^{-1})$$



In the layer where the Pb pollution was recorded, we can obtain the anthropogenic Pb flux through subtracting the annual Pb flux by the background flux (flux contributed from the natural background):

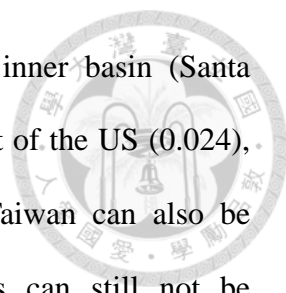
$$\text{Anthropogenic Pb Flux } (\mu\text{g cm}^{-2}\text{yr}^{-1}) = \text{Annual Pb Flux } (\mu\text{g cm}^{-2}\text{yr}^{-1}) - \text{Background Pb Flux } (\mu\text{g cm}^{-2}\text{yr}^{-1})$$

With the sedimentation rate derived from excess ^{210}Pb , the increasing rate of the anthropogenic Pb flux can be obtained through dividing them by the time they show the pollution trend:

$$\begin{aligned} & \text{Increasing Rate of Anthropogenic Pb Flux } (\mu\text{gcm}^{-2}\text{yr}^{-1} \text{ yr}^{-1}) \\ &= \frac{\text{Anthropogenic Pb Flux Change } (\mu\text{gcm}^{-2}\text{yr}^{-1})}{\text{the period of time recorded the increasing anthropogenic Pb flux (yr)}} \end{aligned}$$

In this case, we collated several exemplary case studies around the world which also recorded Pb pollution trend and compared the recalculated increasing rate between these world cities in different aquatic environments (offshore/ in vicinity of city). Such increasing rate of anthropogenic Pb flux can be an evaluation of contamination levels in different areas around the world, also showing a difference in different aquatic system.

Table 3-5 shows the estimated increasing rate of these anthropogenic Pb flux from previous studies (Ng & Patterson, 1982; Huh & Chen, 1988; Hosono at al., 2011; Hosono at al., 2010; Hung & Hsu, 2004). If compared the increasing rate recorded in the vicinity of the cities (bold figure in Table 3-5), the increasing rate of anthropogenic Pb flux recorded in Taiwan (Kaohsiung City) is similar to those recorded in Philippines (Manila City) and Indonesia (Jakarta City) which all ranged around 0.08-0.09 $\mu\text{g cm}^{-2}\text{yr}^{-1} \text{ yr}^{-1}$, showing a similar industrial growing pace in these countries. In addition, the increasing rate calculated from our pollution record (S1) on Gaoping Slope (0.027)



can even be compared to the serious pollution recorded in the inner basin (Santa Barbara Basin) off California during 1930s-1970s in the West Coast of the US (0.024), showing that the pollutants exported from human activities in Taiwan can also be considerable. However, the increasing rate of all these regions can still not be comparable to that on the East China Sea shelf, which mainly received the discharge from Changjiang and Huanghe, and the offshore record is even orders higher than that recorded in the vicinity of the cities, showing that China has exported a large amount of pollutants to the East China Sea within a very short period of time (1980s-now). The increasing rate can be compared to the record off Barcelona, Spain. Moreover, such increasing rate of anthropogenic Pb flux can also display a regional difference due to the distance from the pollutant source. Such as in California Bight, San Pedro Basin has a higher increasing rate of Anthropogenic Pb flux (Ng & Patterson, 1982) for it is proximal to the waste water treatment plants (Hyperion & JWPCP); in Jakarta Bay and Manila Bay, core JAK3 and MNL1 has higher increasing rate of anthropogenic Pb flux for they are closer to the city where provide the major source of the pollutants (Hosono et al., 2010; Hosono et al., 2011); the proximal prodelta has much higher increasing rate than that in the distal prodelta off Barcelona, Spain (Palanques et al., 1998); the sharp decrease in the increasing rate of anthropogenic Pb flux from the head of GPSC (Hung & Hsu, 2004) to that recorded on Gaoping Slope.

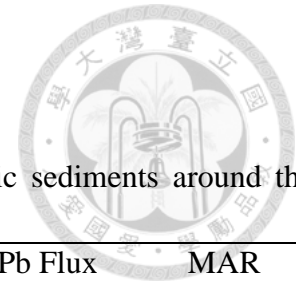


Table 3-5

Estimated increasing rate of anthropogenic Pb flux in different aquatic sediments around the world.

Location	Pb background Flux ($\mu\text{g cm}^{-2}\text{yr}^{-1}$)	Anthropogenic Pb Flux Increasing Rate (flux yr^{-1})	MAR ($\text{g cm}^{-2}\text{yr}^{-1}$)
California Bight, west U.S (1930s-1970s)^f			
Santa Barbara Basin ^f	0.7	0.024	0.092
Santa Monica Basin ^f	0.1	0.010	0.019
San Pedro Basin ^f	0.2	0.038	0.030
East China Sea (ECS) Shelf, east China (1980s-)^g			
Estuary (BC9) ^g	7.5	1.875	1.500
Jakarta Bay, Indonesia (1920s-1990s)^h			
Western Bay (JAK1) ^h	4.2	0.033	0.338
Eastern Bay (JAK3) ^h	11.6	0.087	0.806
Manila Bay, Philippines (1960-1990s)ⁱ			
MNL1 ⁱ	1.2	0.098	0.132
MNL2 ⁱ	8.2	0.075	1.128
The Besòs River Prodelta, Spain (1950s-1980s)^j			
Proximal Prodelta ^j	30.5	1.653	0.174
Distal Prodelta ^j	8.0	0.166	0.094
Gaoping Shelf, southwestern Taiwan (1970s-)^k			
Gaoping Coast (KP) ^k	2.0	0.091	0.234
Gaoping Slope, southwestern Taiwan (1970s-)^l			
Western Gaoping Slope (S2) ^l	0.9	0.015	0.047
Eastern Gaoping Slope (S1) ^l	2.3	0.027	0.106

The increasing rate in **bold figure** indicated the record in the vicinity of the cities, while the other were calculated from the record in offshore sediments.

MAR: Material Accumulation Rate (all derived from ^{210}Pb dating).

All the increasing rate was estimated with the Pb pollution record during the year in the parentheses from:

^f Ng & Patterson (1982)

^g Huh & Chen. (1988)

^h Hosono et al. (2011)

ⁱ Hosono et al. (2010)

^j Palanques et al. (1998)

^k Hung & Hsu (2004)

^l This study

Chapter 4 Conclusion



1. Among our Gaoping Slope and deep sea sites, most of measured trace metals have little variations over time and their ratios with Al (M/Al) reveal their natural variability in the sediments. However, Pb pollution signals can still be found in Gaoping Slope and the sedimentary record can clearly illustrate the onset of industrial development in Taiwan.
2. The comparable cumulative mass of the trace metals observed in the deep sea site and the relatively consistent Ti/Al molar ratio between Gaoping Slope and deep sea, all suggesting that the sediments could cross the narrow shelf and made a considerable amount to transport and accumulate in the deep sea. This transport mechanism could also be applied to those submarine canyons which have characteristics analogous to GPSC (developed on an active continental margin).
3. Natural hazards (earthquakes, typhoons, etc.) tend to be the major agents in Taiwan to cause grand output of sediments into the marine environment. Though they may cause lowered concentration of trace metals due to the dilution of coarser detrital materials, the absolute amount (cumulative mass) of the trace metals contributed from an event over a short time period (less than one year) could be much greater than those delivered from a long-term (year average) steady sedimentation condition, elucidating these natural hazards can also be the major agents to accelerate accumulation of trace metals off southwestern Taiwan.
4. Compared to previous studies conducted in the coastal and offshore region (Hung & Hsu, 2004; Chen & Selvaraj, 2008), many trace metals are found highly enriched in the near source area, yet no significant enrichment of the trace metals is found in the further seaward regions (Gaoping Slope & deep sea) in this study.

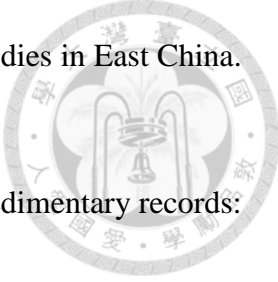
Although no strong pollution signals are recorded beyond the Gaoping Shelf as the pollution signals could be largely diluted with the increasing distance they've been transported, footprints of pollution (Pb) can still be recorded in the Gaoping Slope.

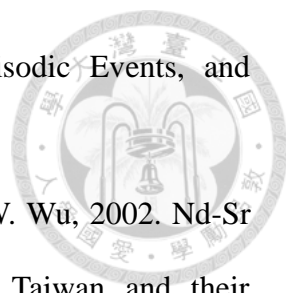
5. Though the cross-shelf transport can deliver a huge amount of terrestrial materials into the deep sea, due to dilution of the pollution signals during the further seaward transport, no interferences from anthropogenic sources were found at the deep sea sites (MT6 & MT7), implying the impact of pollutants discharged from Gaoping River on the deep sea is insignificant.
6. The estimated increasing rates of anthropogenic Pb flux in different areas around the world indicate the pollution level in Taiwan can be compared to most countries in east Asia and the US, while China accounts for the highest increasing rate of the world.

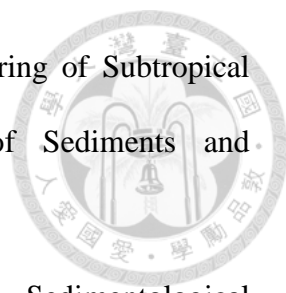
REFERENCE



- Chen, C.T.A., and K. Selvaraj, 2008. Evaluation of elemental enrichments in surface sediments off southwestern Taiwan. *Environmental Geology* 54: 1333-1346.
- Chen, H.F., P.Y. Yeh, S.R. Song, S.C. Hsu, T.N. Yang, Y. Wang, Z.Q. Chi, T.Q. Lee, M.T. Chen, C.L. Cheng, J.J. Zou, and Y.P. Chang, 2013. The Ti/Al molar ratio as a new proxy for tracing sediment transportation processes and its application in aeolian events and sea level change in East Asia. *Journal of Asian Earth Sciences* 73: 31-38.
- Chiang, C.S., and H.S. Yu, 2006. Morphotectonics and incision of the Kaoping submarine canyon, SW Taiwan orogenic wedge. *Geomorphology* 80 (3-4): 199-213.
- Choi, S.C., O.W.H. Wai, T.W.H. Choi, X.D. Li, and C.W. Tsang, 2006. Distribution of cadmium, chromium, copper, lead and zinc in marine sediments in Hong Kong waters. *Environmental Geology* 51: 455-461.
- Chung, C.H., C.F. You, and H.Y. Chu, 2009. Weathering sources in the Gaoping (Kaoping) river catchments, southwestern Taiwan: Insights from major elements, Sr isotopes, and rare earth elements. *Journal of Marine Systems* 76: 433-443.
- Doong, R.A., S.H. Lee, C.C. Lee, Y.C. Sun, and S.C. Wu, 2008. Characterization and composition of heavy metals and persistent organic pollutants in water and estuarine sediments from Gao-ping River, Taiwan. *Marine Pollution Bulletin* 57: 846-857.
- Finney, B.P., and C.A. Huh, 1989. History of Metal Pollution in the Southern California Bight: An Update. *Environmental Science and Technology* 23: 294-303.
- Gao, S., T.C. Luo, B.R. Zhang, H.F. Zhang, Y.W. Han, Z.D. Zhao, and Y.K. Hu, 1998.

- 
- Chemical composition of the continental crust as revealed by studies in East China. *Geochimica et Cosmochimica Acta* 62 (11): 1959-1975.
- Heim, S., and J. Schwarzbauer, 2013. Pollution history revealed by sedimentary records: a review. *Environmental Chemistry Letters* 11: 255-270.
- Honoso, T., C.C. Su, F. Siringan, A. Amano, and S.I. Onodera, 2010. Effects of environmental regulations on heavy metal pollution decline in core sediments from Manila Bay. *Marine Pollution Bulletin* 60: 780-785.
- Hosono, Takahiro, C.C. Su, R. Delinom, Y. Umezawa, T. Toyota, S. Kaneko, and M. Taniguchi, 2011. Decline in heavy metal contamination in marine sediments in Jakarta Bay, Indonesia due to increasing environmental regulations. *Estuarine, Coastal and Shelf Science* 92: 297-306.
- Hu, Z.C., and S. Gao, 2008. Upper crustal abundances of trace elements: A revision and update. *Chemical Geology* 253: 205-221.
- Huh, C.A., and H.Y. Chen, 1999. History of Lead Pollution Recorded in East China Sea Sediments. *Marine Pollution Bulletin* 38 (7): 545-549.
- Huh, C.A., H.L. Lin, S. Lin, and Y.W. Huang, 2009. Modern accumulation rates and a budget of sediment off the Gaoping (Kaoping) River, SW Taiwan: A tidal and flood dominated depositional environment around a submarine canyon. *Journal of Marine Systems* 76: 405-416.
- Hung, J.J., and C.L. Hsu, 2004. Present state and historical changes of trace metal pollution in Kaoping coastal sediments, southwestern Taiwan. *Marine Pollution Bulletin* 49 (11-12): 986-998.
- Järup, L., 2003. Hazards of heavy metal contamination. *British Medical Bulletin* 68 (1): 167-182.
- Kao S.J., and J.D. Milliman, 2008. Water and Sediment Discharge from Small

- 
- Mountainous Rivers, Taiwan: The Roles of Lithology, Episodic Events, and Human Activities. *The Journal of Geology* 116 (5): 431-448.
- Lan, C.Y., C.S. Lee, J.J.S. Shen, C.Y. Lu, S. A. Mertzman, and T.W. Wu, 2002. Nd-Sr isotopic composition and geochemistry of sediments from Taiwan and their implications. *Western Pacific Earth Sciences* 2 (2): 205-222.
- Li, Y.H., 1976. Denudation of Taiwan Island since the Pliocene Epoch. *Geology* 4 (2): 105-107.
- Liu, J.T., K.J. Liu, and J.C. Huang, 2002. The effect of a submarine canyon on the river sediment dispersal and inner shelf sediment movements in southern Taiwan. *Marine Geology* 181: 357-386
- Lynn, D.C., and E. Bonatti, 1965. Mobility of manganese in diagenesis of deep-sea sediments. *Marine Geology* 3 (6): 457-474.
- Milliman, J.D., and J.P.M. Syvitski, 1992. Geomorphic/ Tectonic Control of Sediment Discharge to the Ocean: The Importance of Small Mountainous Rivers. *The Journal of Geology* 100 (5): 525-544.
- Nagajyoti, P.C., K.D. Lee, and T.V.M. Sreekanth, 2010. Heavy metals, occurrence and toxicity for plants: a review. *Environmental Chemistry Letters* 8 (3): 199-216.
- Ng, A., and C.C. Patterson, 1982. Changes of lead and barium with time in California off-shore basin sediments. *Geochimica et Cosmochimica Acta* 46: 2307-2321.
- Palanques, A., J.A. Sanchez-Cabeza, P. Masqué, and L. León, 1998. Historical record of heavy metals in a highly contaminated Mediterranean deposit: The Besòs prodelta. *Marine Chemistry* 61: 209-217.
- Salomons, W., and U. Fornster, 1984. *Metals in the Hydrocycle*. Springer-Verlag, New York 349pp.

- 
- Selvaraj, K., and C.T.A. Chen, 2006. Moderate Chemical Weathering of Subtropical Taiwan: Constraints from Solid – Phase Geochemistry of Sediments and Sedimentary Rocks. *The Journal of Geology* 114 (1): 101-116.
- Su, C.C., S.T. Hsu, H.H. Hsu, J.Y. Lin, and J.J. Dong, 2018. Sedimentological characteristics and seafloor failure offshore SW Taiwan. *Terrestrial, Atmospheric and Oceanic Sciences Journal* 29: 65-76.
- Taylor, S.R., 1964. Abundance of chemical elements in the continental crust: a new table. *Geochimica et Cosmochimica Acta* 28: 1273-1285.
- Turekian, K.K., and K.H. Wedepohl, 1961. Distribution of the elements in some major units of the Earth's crust. *Geological Society of America Bulletin* 72: 175-192.
- Yu, H.S., and G.S. Song, 1993. Submarine physiography around Taiwan and its relation to tectonic setting. *Journal of the geological society of china* 36: 139-156.
- Yu, H.S., and Z.Y. Huang, 2006. Intraslope Basin, Seismic Facies and Sedimentary Processes in the Kaoping Slope, Offshore Southwestern Taiwan. *Terrestrial, Atmospheric and Oceanic Sciences Journal* 17 (4): 659-677.
- Yu, H.S., C.S. Chiang, and S.M. Shen, 2009. Tectonically active sediment dispersal system in SW Taiwan margin with emphasis on the Gaoping (Kaoping) Submarine Canyon. *Journal of Marine Systems* 76: 369-382.
- Zhang, J., and C.L. Liu, 2002. Riverine composition and estuarine geochemistry of particulate metals in China - Weathering features, anthropogenic impact and chemical fluxes. *Estuarine Coastal and Shelf Science* 54 (6): 1051-1070.
- Zwolsman, John J.G., G.W. Berger, and G.T.M. Van Eck, 1993. Sediment accumulation rates, historical input, post-depositional mobility and retention of major elements and trace metals in salt marsh sediments of the Scheldt estuary, SW Netherlands. *Marine Chemistry* 44: 73-94.

Water Resource Agency Hydrological Yearbook, 2017. E-book, Water Resource Agency,
Ministry of Economic Affairs, Taiwan, R.O.C.

林靜怡、董家鈞、許懷後、鄭文彬、蘇志杰，2016。台灣西南海域天然氣水合物賦存區海床穩定性的基礎研究(1/3)。第二期能源國家型科技計畫期末成果效益報告，地熱與天然氣水合物主軸中心。

林佳緯，2006。台灣西南海域表層沉積物金屬與顆粒組成空間分佈與控制因子。國立台灣大學海洋研究所碩士論文，51頁。

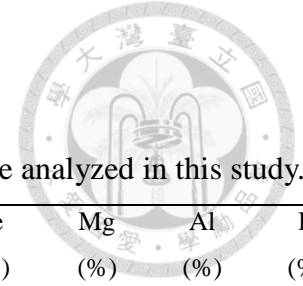
蔡帛軒，2014。臺灣西南海域極端事件引發海底地質災害對有機碳埋藏的影響。國立台灣大學海洋研究所碩士論文，71頁。

徐聖婷，2015。臺灣西南海域現代沉積物之傳輸途徑與機制。國立台灣大學海洋研究所碩士論文，67頁。

楊嘉豪，2002。東海陸棚沉積物中金屬元素之垂直分佈研究。國立台灣大學海洋研究所碩士論文，73頁。

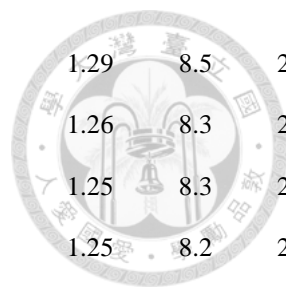
鄭屹雅，2012。臺灣西南海域沉積物重力流引發之海底電纜斷裂事件。國立台灣大學海洋研究所碩士論文，98頁。

APPENDIX



The concentrations of the trace and major elements in all depth of each sediment core analyzed in this study.

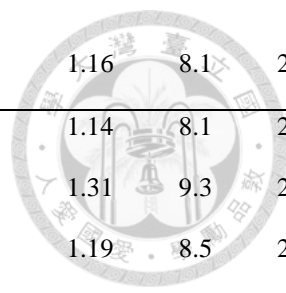
PL02	Zn ($\mu\text{g g}^{-1}$)	Cr ($\mu\text{g g}^{-1}$)	Pb ($\mu\text{g g}^{-1}$)	Co ($\mu\text{g g}^{-1}$)	Ni ($\mu\text{g g}^{-1}$)	Cu ($\mu\text{g g}^{-1}$)	Cd ($\mu\text{g g}^{-1}$)	Mn ($\mu\text{g g}^{-1}$)	Fe (%)	Mg (%)	Al (%)	K (%)	Ti (%)
0.5 cm	80	63	17	11.7	27.0	13	0.10	595	3.5	0.95	6.5	1.99	0.37
1.5 cm	81	64	16	11.5	28.3	14	0.11	367	3.3	0.91	4.7	1.91	0.36
2.5 cm	80	66	12	11.7	29.2	14	0.15	333	3.6	0.98	6.3	2.05	0.39
3.5 cm	77	63	14	10.9	27.1	13	0.12	301	3.5	0.96	6.1	2.00	0.38
4.5 cm	81	64	14	11.0	27.8	13	0.13	310	3.5	0.97	6.6	2.03	0.38
5.5 cm	85	65	15	11.0	28.0	13	0.14	289	3.7	1.02	6.5	2.13	0.40
6.5 cm	82	64	12	10.9	27.7	13	0.13	279	3.6	0.98	6.6	2.04	0.38
7.5 cm	81	66	13	11.1	28.4	13	0.15	300	3.4	0.97	6.2	2.01	0.38
8.5 cm	81	61	14	10.3	26.3	12	0.13	277	3.3	0.94	6.1	1.97	0.37
9.5 cm	79	57	12	9.8	25.0	11	0.12	278	3.2	0.93	6.5	1.92	0.36
10.5 cm	80	64	13	10.9	27.7	13	0.14	269	3.5	1.00	6.1	2.06	0.39
11.5 cm	82	63	13	11.0	27.2	12	0.12	275	3.6	1.01	6.2	2.09	0.40
12.5 cm	82	64	13	11.0	27.4	13	0.11	250	3.8	1.06	7.4	2.19	0.42
13.5 cm	83	62	13	10.5	26.6	12	0.14	259	3.4	0.96	6.3	2.01	0.38
14.5 cm	79	64	13	11.0	27.9	13	0.13	267	3.4	0.96	5.4	2.02	0.38
Minimum	77	57	12	9.8	25.0	11	0.10	250	3.2	0.91	4.7	1.91	0.36
Maximum	85	66	17	11.7	29.2	14	0.15	595	3.8	1.06	7.4	2.19	0.42
Mean	81	63	14	11.0	27.4	13	0.13	310	3.5	0.97	6.2	2.03	0.38
S2	Zn ($\mu\text{g g}^{-1}$)	Cr ($\mu\text{g g}^{-1}$)	Pb ($\mu\text{g g}^{-1}$)	Co ($\mu\text{g g}^{-1}$)	Ni ($\mu\text{g g}^{-1}$)	Cu ($\mu\text{g g}^{-1}$)	Cd ($\mu\text{g g}^{-1}$)	Mn ($\mu\text{g g}^{-1}$)	Fe (%)	Mg (%)	Al (%)	K (%)	Ti (%)
0.5 cm	103	75	27	13.0	30.4	18	0.13	2022	3.8	1.18	7.9	2.24	0.38
1.5 cm	96	64	19	11.9	30.1	17	0.15	611	4.0	1.22	8.1	2.30	0.39
2.5 cm	98	70	19	12.2	30.7	18	0.12	456	4.3	1.26	8.4	2.40	0.40
3.5 cm	97	69	18	11.7	30.2	17	0.13	394	4.1	1.23	7.9	2.37	0.39
4.5 cm	103	71	17	12.6	32.3	19	0.14	390	4.1	1.23	8.2	2.42	0.39



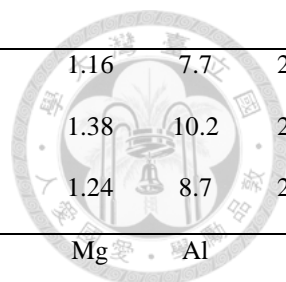
5.5 cm	99	71	19	12.1	31.4	19	0.20	393	4.1	1.29	8.5	2.49	0.41
6.5 cm	99	68	19	12.1	31.0	18	0.18	395	4.0	1.26	8.3	2.39	0.40
7.5 cm	98	51	18	12.0	30.7	18	0.13	388	4.1	1.25	8.3	2.39	0.40
8.5 cm	99	71	17	12.5	31.9	19	0.15	402	4.1	1.25	8.2	2.38	0.40
9.5 cm	98	73	16	13.1	32.8	19	0.18	399	3.9	1.23	8.2	2.35	0.39
10.5 cm	98	69	18	12.1	30.1	17	0.20	362	3.8	1.20	7.7	2.28	0.38
11.5 cm	100	64	18	13.9	33.9	19	0.15	398	4.1	1.25	8.3	2.44	0.39
12.5 cm	101	77	20	13.7	34.2	20	0.16	385	4.3	1.32	8.7	2.59	0.42
13.5 cm	97	52	18	12.0	30.0	17	0.14	335	4.0	1.18	8.1	2.36	0.39
14.5 cm	95	70	17	12.1	30.9	18	0.16	356	4.2	1.27	8.4	2.44	0.34

Minimum	95	51	16	11.7	30.0	17	0.12	335	3.8	1.18	7.7	2.24	0.34
Maximum	103	77	27	13.9	34.2	20	0.20	2022	4.3	1.32	8.7	2.59	0.42
Mean	99	68	19	12.5	31.4	18	0.15	513	4.1	1.24	8.2	2.39	0.39

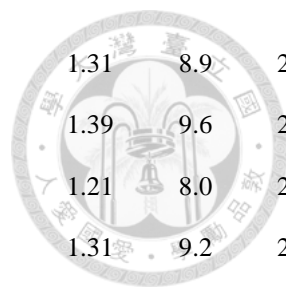
S6	Zn	Cr	Pb	Co	Ni	Cu	Cd	Mn	Fe	Mg	Al	K	Ti
	($\mu\text{g g}^{-1}$)	($\mu\text{g g}^{-1}$)	($\mu\text{g g}^{-1}$)	($\mu\text{g g}^{-1}$)	($\mu\text{g g}^{-1}$)	($\mu\text{g g}^{-1}$)	($\mu\text{g g}^{-1}$)	($\mu\text{g g}^{-1}$)	(%)	(%)	(%)	(%)	(%)
0.5 cm	103	71	24	13.3	30.1	18	0.10	775	4.0	1.16	8.3	2.49	0.40
1.5 cm	101	72	22	13.6	31.2	17	0.10	630	4.0	1.14	8.1	2.41	0.39
2.5 cm	102	70	22	11.6	29.7	17	0.14	369	4.2	1.19	8.6	2.55	0.42
3.5 cm	99	72	23	12.2	30.6	17	0.13	313	4.3	1.23	9.0	2.65	0.44
4.5 cm	99	73	23	12.9	31.6	18	0.12	317	4.0	1.15	8.4	2.51	0.41
5.5 cm	100	73	21	13.0	31.6	17	0.11	341	4.3	1.28	9.2	2.77	0.45
6.5 cm	100	68	22	12.2	29.7	16	0.10	302	4.0	1.17	8.2	2.46	0.40
7.5 cm	100	70	21	12.1	29.8	16	0.12	293	4.3	1.31	9.3	2.79	0.46
8.5 cm	100	70	21	12.4	30.1	16	0.11	292	3.8	1.16	8.2	2.48	0.40
9.5 cm	97	67	21	11.7	28.7	15	0.09	265	4.0	1.21	8.7	2.61	0.36
10.5 cm	97	68	21	11.7	29.0	15	0.09	266	4.0	1.20	8.5	2.55	0.42
11.5 cm	95	67	19	11.5	28.5	15	0.08	264	3.9	1.15	8.2	2.47	0.41
12.5 cm	97	69	21	11.6	29.3	16	0.09	275	4.0	1.18	8.4	2.55	0.41
13.5 cm	94	66	19	11.1	28.3	15	0.07	270	4.0	1.17	8.4	2.52	0.36
14.5 cm	95	67	18	11.5	29.5	16	0.11	282	4.0	1.20	8.6	2.60	0.42



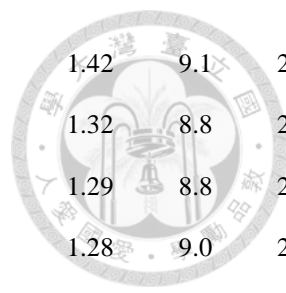
15.5 cm	91	67	20	11.0	28.6	15	0.14	286	3.8	1.16	8.1	2.50	0.40
Minimum	91	66	18	11.0	28.3	15	0.07	264	3.8	1.14	8.1	2.41	0.36
Maximum	103	73	24	13.6	31.6	18	0.14	775	4.3	1.31	9.3	2.79	0.46
Mean	98	69	21	12.1	29.8	16	0.11	346	4.0	1.19	8.5	2.56	0.41
S1	Zn	Cr	Pb	Co	Ni	Cu	Cd	Mn	Fe	Mg	Al	K	Ti
	($\mu\text{g g}^{-1}$)	($\mu\text{g g}^{-1}$)	($\mu\text{g g}^{-1}$)	($\mu\text{g g}^{-1}$)	($\mu\text{g g}^{-1}$)	($\mu\text{g g}^{-1}$)	($\mu\text{g g}^{-1}$)	($\mu\text{g g}^{-1}$)	(%)	(%)	(%)	(%)	(%)
0.5 cm	110	73	30	13.0	31.4	21	0.13	438	4.5	1.19	9.0	2.63	0.39
1.5 cm	106	73	29	13.1	31.7	20	0.13	442	4.4	1.21	8.7	2.49	0.44
2.5 cm	111	74	27	13.6	32.5	21	0.13	527	4.5	1.23	8.9	2.56	0.45
3.5 cm	108	72	28	13.1	32.4	20	0.14	489	4.5	1.25	8.9	2.57	0.46
4.5 cm	105	71	24	12.8	32.0	20	0.14	444	4.5	1.26	8.8	2.53	0.45
5.5 cm	103	74	24	13.0	32.8	19	0.14	402	4.6	1.29	8.9	2.53	0.45
6.5 cm	99	69	23	12.1	30.5	18	0.12	363	4.5	1.26	8.8	2.50	0.44
7.5 cm	106	73	25	12.7	32.1	19	0.13	358	4.8	1.32	9.3	2.69	0.45
8.5 cm	104	69	22	12.0	30.6	18	0.11	351	4.4	1.23	8.4	2.40	0.43
9.5 cm	100	69	21	12.1	30.3	17	0.13	350	4.1	1.17	8.0	2.32	0.44
10.5 cm	101	74	23	12.8	32.0	19	0.14	376	4.7	1.30	9.0	2.56	0.41
11.5 cm	103	75	22	12.9	32.4	19	0.16	369	4.7	1.30	9.1	2.58	0.47
12.5 cm	105	74	23	13.4	32.6	20	0.12	335	4.8	1.28	9.3	2.63	0.47
13.5 cm	110	85	24	15.1	36.9	24	0.18	311	4.9	1.21	9.3	2.64	0.48
14.5 cm	103	75	23	13.8	33.3	20	0.14	339	5.2	1.38	10.2	2.89	0.51
15.5 cm	98	70	22	12.5	31.0	18	0.11	348	4.7	1.31	9.2	2.60	0.41
16.5 cm	102	73	25	12.9	32.0	18	0.15	372	4.4	1.28	8.8	2.50	0.45
17.5 cm	101	73	23	13.1	32.4	19	0.14	352	4.2	1.20	7.9	2.39	0.43
18.5 cm	106	72	23	12.7	31.7	19	0.16	342	4.1	1.17	8.1	2.39	0.42
19.5 cm	101	69	22	12.4	30.7	18	0.13	340	4.1	1.18	7.9	2.36	0.42
20.5 cm	100	72	20	12.9	32.3	18	0.17	366	4.0	1.16	7.8	2.26	0.42
22.5 cm	98	59	20	12.3	31.1	17	0.12	360	4.4	1.27	8.6	2.44	0.44
24.5 cm	96	69	18	12.2	31.1	17	0.15	377	4.1	1.19	7.7	2.19	0.41
26.5 cm	95	70	18	11.9	30.5	17	0.14	351	4.1	1.19	7.8	2.26	0.43



Minimum	95	59	18	11.9	30.3	17	0.11	311	4.0	1.16	7.7	2.19	0.39
Maximum	111	85	30	15.1	36.9	24	0.18	527	5.2	1.38	10.2	2.89	0.51
Mean	103	72	23	12.9	31.9	19	0.14	379	4.5	1.24	8.7	2.50	0.44
B4G	Zn	Cr	Pb	Co	Ni	Cu	Cd	Mn	Fe	Mg	Al	K	Ti
	($\mu\text{g g}^{-1}$)	($\mu\text{g g}^{-1}$)	($\mu\text{g g}^{-1}$)	($\mu\text{g g}^{-1}$)	($\mu\text{g g}^{-1}$)	($\mu\text{g g}^{-1}$)	($\mu\text{g g}^{-1}$)	($\mu\text{g g}^{-1}$)	(%)	(%)	(%)	(%)	(%)
0.5 cm	81	67	19	9.3	27.6	12	0.23	301	3.6	1.16	6.9	1.98	0.39
1.5 cm	81	64	19	9.6	26.4	11	0.26	267	3.6	1.19	7.3	2.09	0.40
2.5 cm	81	66	20	9.6	27.0	12	0.24	269	3.5	1.20	7.0	2.05	0.41
3.5 cm	77	62	16	9.3	26.1	11	0.17	308	3.6	1.21	7.1	2.05	0.39
4.5 cm	82	65	16	9.6	26.5	12	0.22	301	3.5	1.22	6.8	2.07	0.40
5.5 cm	79	65	14	9.6	26.6	12	0.20	298	3.5	1.17	7.0	2.00	0.39
6.5 cm	82	64	15	9.8	26.8	12	0.13	248	3.5	1.11	6.9	1.99	0.28
7.5 cm	81	63	15	9.0	26.1	12	0.14	256	3.8	1.21	7.4	2.13	0.40
8.5 cm	84	70	15	9.9	29.1	13	0.17	289	3.9	1.25	7.3	2.16	0.41
9.5 cm	87	68	15	9.8	28.7	14	0.21	278	3.9	1.22	7.2	2.16	0.41
Minimum	77	62	14	9.0	26.1	11	0.13	248	3.5	1.11	6.8	1.98	0.28
Maximum	87	70	20	9.9	29.1	14	0.26	308	3.9	1.25	7.4	2.16	0.41
Mean	81	65	16	9.5	27.1	12	0.20	282	3.6	1.19	7.1	2.07	0.39
MT6	Zn	Cr	Pb	Co	Ni	Cu	Cd	Mn	Fe	Mg	Al	K	Ti
	($\mu\text{g g}^{-1}$)	($\mu\text{g g}^{-1}$)	($\mu\text{g g}^{-1}$)	($\mu\text{g g}^{-1}$)	($\mu\text{g g}^{-1}$)	($\mu\text{g g}^{-1}$)	($\mu\text{g g}^{-1}$)	($\mu\text{g g}^{-1}$)	(%)	(%)	(%)	(%)	(%)
0.5 cm	101	70	19	12.3	29.8	20	0.13	1160	4.5	1.28	8.8	2.46	0.46
1.5 cm	103	73	23	12.6	31.4	22	0.18	548	4.6	1.28	8.8	2.53	0.45
2.5 cm	101	71	21	11.8	30.3	21	0.19	477	4.3	1.23	8.3	2.47	0.44
3.5 cm	101	72	22	12.1	30.7	21	0.17	481	4.6	1.30	8.8	2.57	0.46
4.5 cm	100	71	18	12.0	30.7	21	0.19	548	4.7	1.31	9.0	2.60	0.48
5.5 cm	97	68	18	11.6	30.3	20	0.25	510	4.0	1.17	7.2	2.33	0.45
6.5 cm	98	69	18	11.6	30.3	20	0.21	462	4.4	1.29	8.2	2.56	0.48
7.5 cm	100	74	19	12.4	31.5	22	0.15	469	4.5	1.31	8.8	2.61	0.46
8.5 cm	105	76	22	12.7	31.9	22	0.18	452	4.7	1.30	9.0	2.71	0.47
9.5 cm	100	74	20	12.4	31.5	22	0.22	478	4.7	1.31	9.0	2.77	0.43



16.5 cm	101	69	17	12.4	31.0	22	0.19	490	4.4	1.31	8.9	2.60	0.47
20.5 cm	97	73	19	12.4	31.4	22	0.21	477	4.8	1.39	9.6	2.83	0.50
24.5 cm	94	64	17	11.4	29.9	18	0.19	491	4.1	1.21	8.0	2.48	0.46
28.5 cm	102	74	20	13.0	32.3	22	0.18	516	4.6	1.31	9.2	2.77	0.48
32.5 cm	101	73	17	12.8	32.1	23	0.20	446	4.7	1.38	9.2	2.69	0.47
36.5 cm	88	62	13	12.0	30.9	16	0.20	479	3.8	1.10	7.7	2.16	0.44
40.5 cm	113	74	20	12.9	32.7	24	0.22	442	4.5	1.34	8.8	2.63	0.46
44.5 cm	86	63	9	11.0	28.2	16	0.16	393	3.6	1.12	7.3	2.03	0.42
48.5 cm	102	72	18	12.2	31.8	21	0.20	496	4.5	1.40	8.6	2.51	0.44
52.5 cm	106	72	18	12.4	31.9	22	0.22	475	4.6	1.36	8.5	2.56	0.45
56.5 cm	108	65	19	13.1	33.9	21	0.18	550	4.8	1.35	9.2	2.68	0.42
Minimum	86	62	9	11.0	28.2	16	0.13	393	3.6	1.10	7.2	2.03	0.42
Maximum	113	76	23	13.1	33.9	24	0.25	1160	4.8	1.40	9.6	2.83	0.50
Mean	100	70	18	12.2	31.2	21	0.19	516	4.4	1.29	8.6	2.55	0.46
MT7	Zn	Cr	Pb	Co	Ni	Cu	Cd	Mn	Fe	Mg	Al	K	Ti
	($\mu\text{g g}^{-1}$)	($\mu\text{g g}^{-1}$)	($\mu\text{g g}^{-1}$)	($\mu\text{g g}^{-1}$)	($\mu\text{g g}^{-1}$)	($\mu\text{g g}^{-1}$)	($\mu\text{g g}^{-1}$)	($\mu\text{g g}^{-1}$)	(%)	(%)	(%)	(%)	(%)
0.5 cm	100	73	22	12.8	32.8	25	0.15	418	4.2	1.36	8.8	2.50	0.41
1.5 cm	99	67	19	12.1	30.6	25	0.15	406	3.6	1.26	7.5	2.09	0.36
3.5 cm	97	69	20	12.3	30.9	24	0.11	382	3.9	1.26	7.9	2.28	0.37
5.5 cm	96	59	20	11.9	29.6	22	0.09	387	3.9	1.22	7.8	2.21	0.37
7.5 cm	98	69	19	12.4	31.1	22	0.12	402	4.1	1.28	8.3	2.36	0.39
9.5 cm	99	72	18	12.5	31.2	22	0.24	388	3.8	1.17	8.0	2.31	0.36
11.5 cm	93	68	18	11.5	29.3	18	0.10	357	3.8	1.14	8.0	2.31	0.38
13.5 cm	98	72	18	12.3	30.9	22	0.22	377	4.0	1.22	8.5	2.32	0.38
14.5 cm	99	70	18	12.3	30.6	20	0.10	355	4.2	1.27	8.5	2.45	0.39
17.5 cm	102	73	18	13.3	33.3	28	0.32	407	3.7	1.25	7.7	2.31	0.37
18.5 cm	103	72	19	12.9	32.1	25	0.16	376	3.9	1.21	8.3	2.36	0.38
20.5 cm	99	70	16	12.5	31.3	24	0.11	406	4.1	1.32	8.5	2.42	0.41
21.5 cm	103	76	17	13.8	33.8	25	0.15	415	4.5	1.42	9.2	2.57	0.42
22.5 cm	96	61	18	12.8	31.0	22	0.12	376	4.0	1.23	8.0	2.24	0.37



24.5 cm	101	68	19	12.6	31.7	24	0.12	391	4.4	1.42	9.1	2.58	0.42
25.5 cm	105	77	19	13.6	33.7	25	0.13	1663	4.3	1.32	8.8	2.46	0.41
29.5 cm	104	71	19	12.7	31.9	23	0.14	861	4.2	1.29	8.8	2.49	0.41
30.5 cm	106	77	20	14.5	33.5	24	0.14	1137	4.3	1.28	9.0	2.54	0.41
31.5 cm	105	72	23	14.7	31.5	21	0.12	1201	4.8	1.35	8.6	2.73	0.46
32.5 cm	100	75	20	13.0	31.9	22	0.13	658	4.2	1.26	8.9	2.45	0.42
33.5 cm	98	70	17	11.6	30.3	22	0.11	466	3.9	1.22	8.2	2.29	0.39
36.5 cm	103	59	18	12.9	33.2	24	0.24	505	4.0	1.27	8.4	2.38	0.40
40.5 cm	97	70	19	12.1	30.2	22	0.12	489	4.4	1.37	9.0	2.52	0.43
48.5 cm	97	69	20	12.3	30.7	21	0.12	446	4.4	1.32	8.9	2.53	0.42
56.5 cm	99	75	17	13.0	32.7	24	0.18	392	4.4	1.44	9.5	2.62	0.44
Minimum	93	59	16	11.5	29.3	18	0.09	355	3.6	1.14	7.5	2.09	0.36
Maximum	106	77	23	14.7	33.8	28	0.32	1663	4.8	1.44	9.5	2.73	0.46
Mean	100	70	19	12.7	31.6	23	0.15	547	4.1	1.29	8.5	2.41	0.40

